2014-12-09

Characterization of Corneal Biomechanics using Customized Atomic Force Microscopy Techniques

Janice M. Dias
University of Miami, JMDIAS87@GMAIL.COM

UNIVERSITY OF MIAMI

CHARACTERIZATION OF CORNEAL BIOMECHANICS USING CUSTOMIZED ATOMIC FORCE MICROSCOPY TECHNIQUES

By

Janice Maxine Dias

A DISSERTATION

Submitted to the Faculty
of the University of Miami
in partial fulfillment of the requirements for
the degree of Doctor of Philosophy

Coral Gables, Florida

December 2014

UNIVERSITY OF MIAMI

A dissertation submitted in partial fulfillment of
the requirements for the degree of
Doctor of Philosophy

CHARACTERIZATION OF CORNEAL BIOMECHANICS USING CUSTOMIZED ATOMIC FORCE MICROSCOPY TECHNIQUES

Janice Maxine Dias

Approved:

_____ Noel Marysa Ziebarth, Ph.D. Assistant Professor of Biomedical Engineering	_____ Fabrice Manns, Ph.D. Professor of Biomedical Engineering
_____ Fotios Andreopoulos, Ph.D. Associate Professor of Biomedical Engineering	_____ Vincent Moy, Ph.D. Professor of Physiology and Biophysics
_____ Sonio Yoo, M.D. Professor of Ophthalmology	_____ M. Brian Blake, Ph.D. Dean of Graduate School

DIAS, JANICE MAXINE (Ph.D., Biomedical Engineering)

Characterization of Corneal Biomechanics using Customized Atomic Force Microscopy Techniques (December 2014)

Abstract of a dissertation at the University of Miami.

Dissertation supervised by Professor Noel Marysa Ziebarth.
No. of pages in text. (183)

Corneal biomechanics has become an increasingly important field within ophthalmology. Striving to establish a relationship between corneal physiological structure and function, corneal biomechanics is an objective, quantitative measure that aids in the development and improvement of diagnostic and therapeutic methods for corneal-related diseases. The goal of this project was to advance the technology of Atomic Force Microscopy (AFM) as a suitable characterization technique within the field of corneal biomechanics. The studies of this project include the development of AFM instrumentation, experimental techniques, and models to measure the elastic, viscoelastic, and poroelastic properties of the cornea in situ. Such developed instrumentation, techniques, and models were then implemented to quantify the treatment efficacy of corneal crosslinking for keratoconus, the most prevalent corneal dystrophy in the United States. In addition, age implications of the treatment efficacy of corneal crosslinking were determined using corneal biomechanics measured from the developed AFM technology.

DEDICATION

I would like to dedicate the obtainment of this degree to my late grandfather, Dexter Watson, for his hard work and efforts in paving a better way of life for his children and descendants. He will be missed and loved, but his legacy will forever live on through me.

ACKNOWLEDGEMENTS

I would like to thank my graduate research advisor, Dr. Noel Ziebarth her continuous guidance and support through this tenure. Thank you for this life-changing opportunity.

Secondly, I would like to acknowledge Dr. Michael Gaines for exposing me to the field of biomedical research. My passion for research would not have been ignited if it was not for your efforts.

Finally, I would like to express my gratitude to my parents, extended family, friends, and the Church for their emotional and spiritual support throughout the years. I am so grateful for your encouragement and prayers that have brought me through this chapter of my life. I love you all very much.

TABLE OF CONTENTS

Page

LIST OF FIGURES ix

LIST OF TABLES xiv

PUBLICATION NOTE xv

Chapter

1 Specific Aims 1

2 Background and Significance 4
2.1 Anatomy and Physiology of the Cornea 4
2.1.1 Overview 4
2.1.2 Cellular Layers 5
2.1.3 Basement Membranes 6
2.1.4Stroma 8
2.2 Corneal Biomechanics 10
2.2.1 Significance 10
2.2.2 Corneal Biomechanical Testing 12
2.3 Corneal Crosslinking 17
2.3.1 Clinical Need 17
2.3.2 Theory 18
2.3.3 Technique 20
2.3.4 Importance of Biomechanical Testing for Corneal Crosslinking 22
2.4 Biomechanical Measurements using Atomic Force Microscopy 24
2.4.1 Background 24
2.4.2 Mechanical Characterization 25

3 Measurement Protocol for Corneal Biomechanical Experimentation 28
3.1 Purpose 28
3.2 Corneal Holder 28
3.3 Tip Modification 30
3.4 Corneal Hydration 40
3.4.1 Rationale 40
3.4.2 Materials and Methods 41
3.4.3 Results 43
3.4.4 Discussion 45
3.5 Summary 51

4 Development of AFM Viscoelastic Capability 52
4.1 Purpose 52

4.2 Hardware 52
4.3 Software 56
4.3.1 Overview 56
4.3.2 Data Storage 57
4.3.3 Data Recording 61
4.3.4 Data Processing 63
4.3.5 Viscoelastic Model Fitting 64
4.4 Validation of Viscoelastic Capability 65
4.5 Summary 67

5 Biomechanical Models 69
5.1 Purpose 69
5.2 Elasticity Models 69
5.2.1 Overview 69
5.2.2 Spherical Indenter: Hertz Model 70
5.2.3 Conical Indenter: Sneddon Model 71
5.2.4 Pyramidal Indenter 72
5.2.4.1 Bilodeau Model 72
5.2.4.2 Rico Model 73
5.2.5 Multi-Layered Models 75
5.2.5.1 Overview 75
5.2.5.2 King Model 75
5.2.5.3 Gao Model 76
5.2.5.4 Dimitriadis Model 77
5.2.5.5 Chadwick Model 78
5.2.5.6 Summary of Multi-Layered Models 79
5.3 Viscoelasticity Models 81
5.3.1 Overview 81
5.3.2 Standard Linear Viscoelastic Models 82
5.3.2.1 Overview 82
5.3.2.2 Maxwell Model 84
5.3.2.3 Voigt Model 86
5.3.2.4 Kelvin Model 87
5.3.3 Advanced Linear Viscoelastic Models 90
5.3.3.1 Overview 90
5.3.3.2 Darling Model 90
5.3.3.3 Cheng Model 92
5.3.3.4 Mattice Model 94
5.3.3.5 Kaufman Model 97
5.3.3.6 Wang Model 98
5.3.3.7 Cheneler Model 100
5.3.4 Quasilinear Viscoelasticity: Tripathy Model 103
5.4 Poroelasticity Models 106
5.4.1 Overview 106
5.4.2 Kalcioglu-Hu Model 107

5.5 Implementation of Models for Stress Relaxation on Sample Corneal Data 110
5.6 Summary 113

6 Characterization of Corneal Biomechanical Properties 115
6.1 Purpose 115
6.2 Crosslinking Protocols 115
6.2.1 Dresden 115
6.2.2 Accelerated Crosslinking 116
6.2.3 Genipin 116
6.3 Porcine Corneal Study 118
6.3.1Tissue Acquisition 118
6.3.2 AFM Mechanical Testing 119
6.3.3 Results 120
6.3.3.1 Thickness 120
6.3.3.2 Elasticity 121
6.3.3.3 Viscoelasticity 122
6.3.3.4 Poroelasticity 123
6.3.4 Discussion 126
6.3.4.1 Elasticity 126
6.3.4.2 Viscosity 127
6.3.4.3 Diffusivity 128
6.4 Human Corneal Study 129
6.4.1Tissue Acquisition 129
6.4.2 Corneal Crosslinking Treatment 130
6.4.3 AFM Mechanical Testing 131
6.4.4 Results 132
6.4.4.1 Thickness 132
6.4.4.2 Elasticity 132
6.4.4.3 Viscoelasticity 133
6.4.4.4 Poroelasticity 136
6.4.5 Discussion 137
6.4.5.1 Elasticity 137
6.4.5.2 Viscosity 138
6.4.5.3 Diffusivity 139
6.5 Summary 139

7 Summary 141

REFERENCES 146

Appendix 1. Stress Relaxation Igor Pro Code Modifications 162

Appendix 2. Viscoelasticity (Darling Model) 170

Appendix 3. Poroelasticity (Kalcioglu-Hu Model) ……..... 177

LIST OF FIGURES

2.1	Diagram of the Basic Anatomy of the Human Eye Globe (From: Manns, F. BME545, Visual Optics. Lecture 13: Optics of the Eye and Magnifier.).	**5**
2.2	Histological section of the human cornea. The cornea is composed of five layers: (A) epithelium, (B) Bowman's membrane, (C) stroma, (D) Descemet's membrane, and (E) endothelium. ((Ziebarth, Rico et al. 2010).	**5**
2.3	Schematic of Tensile Stretcher (Kohlhaas, Spoerl *et al*. 2006).	**14**
2.4	*Left,* Schematic of a corneal inflation rig. *Right,* Picture of a Bovine Cornea placed onto an Inflation Rig (Boyce, Grazier *et al*. 2008).	**15**
2.5	Diagram of the Ocular Analyzer Response Principle and Waveforms (http://www.gatinel.com/wp-content/uploads/2010/01/ocular-response-analyzer-normal.jpg and (Reichert 2009)).	**15**
2.6	Diagrams of a normal and keratoconic cornea. (From: Cornea Research Foundation of America; http://www.cornea.org/index.php/research/corneal_conditions/keratoconus/).	**20**
2.7	Picture of a riboflavin-UVA irradiation treatment administered to a patient (Wollensak, Spoerl et al. 2003).	**25**
3.1	SolidWorks Rendition of the Custom Corneal Holder with the Anchoring Top and the Base Assembled.	**29**
3.2	Custom Corneal Holder. *Left*: Picture of the Anchoring Top and the Base Disassembled. Right: Picture of Anchoring Top and Base Assembled.	**30**
3.3	Picture of Modified AFM tip with microsphere.	**31**
3.4	*Left,* Side View of Cantilever Holder. *Right,* Close up of Cantilever Anchored in Holder.	**34**
3.5	*Left*, Picture of deflection measurement on a rigid surface, the silicon base of reference cantilever. *Righ*t, Picture of the slope curve fit of the deflection measurement to calculate, S_{hard}.	**36**

3.6	*Left*, Picture of deflection measurement on the reference cantilever. *Right*, Picture of the slope curve fit of the deflection measurement to calculate, S_{ref}.	**36**
3.7	Picture of the Canvas measurement analysis to derive the length of the reference cantilever, L_{ref}, and the radius of the glass microbead, D.	**39**
3.8	Pictures of the Modified Tip Calibration using the Reference Cantilever Method. *Left*: The centerline of the uncalibrated tip is aligned with the end of the reference cantilever. *Right*: Reference cantilever shifted directly under uncalibrated tip for deflection measurement.	**39**
3.9	Bar Graph of the Average Corneal Thickness Percentage Change. A bar graph comparing the thickness percentage changes after 120 minutes in different hydration media. Samples with the limbus had a greater change in thickness than samples without the limbus.	**44**
3.10	Bar Graph of the Average Corneal Elasticity Percentage Change. A bar graph comparing the corneal Young's modulus percentage changes after 120 minutes in different hydration media. Samples with the limbus had a greater change in Young's modulus than samples without the limbus.	**44**
4.1	Picture of AFM System with Integral Components.	**53**
4.2	*Left,* Side View of Cantilever Holder. *Right,* Close up of Cantilever Anchored in Holder.	**54**
4.3	Schematic of Photodiode Circuitry.	**54**
4.4	AFM Stress-Relaxation Testing. *Left,* Graph of Vertical Cantilever Displacement Held Constant on Tissue Surface During Stress-Relaxation tesing. *Right,* Graph of Resultant Force Response of Tissue due to Constant Strain Application from AFM Cantilever.	**58**
4.5	Contact Output Waves (or Outwaves) used in computer software to conduct elasticity testing. *Left*, Graph of Approach Contact Outwave for Elasticity Testing. *Right*, Retract Contact Outwave for Elasticity Testing.	**59**
4.6	Contact Output Wave (or Outwave) used in computer software to conduct stress relaxation testing.	**59**

4.7	Raw data force response of the Petri dish recorded from the position-sensitive photodiode during the cantilever's approach toward the Petri dish (A), stress relaxation testing from the Petri dish (B), and cantilever's retraction away from the Petri dish (C).	**66**
4.8	Raw data force response of the cornea recorded from the position-sensitive photodiode during the cantilever's approach toward the cornea (A), stress relaxation testing (B), and cantilever's retract away from the cornea (C).	**67**
5.1	Diagram model of the blunted pyramidal indenter (Rico *et al*. 2005).	**74**
5.2	Bar Graph of Calculated Bowman's Membrane Young's Modulus from the Multi-Layered Models.	**81**
5.3	The dashpot mechanical analog with spring constant, k.	**83**
5.4	The spring mechanical analog with spring constant, k.	**84**
5.5	The Maxwell Model.	**87**
5.6	The Voigt Model.	**87**
5.7	The Kelvin Model.	**88**
5.8	The Cheng Viscoelastic model.	**97**
5.9	The Maxwell-Weichert Viscoelastic model used by Kaufman *et al* (2008).	**98**
5.10	The Zener (or Kelvin) Viscoelastic model used by Wang *et al* (2013).	**101**
5.11	The Generalized Standard Linear Solid Viscoelastic model used by Cheneler *et al* (2013).	**102**
5.12	Curve Fits of the Darling, Mattice, Cheng, Kaufman, and Wang Stress Relaxation Models with Sample Corneal Mechanical Data.	**112**
5.13	Curve Fit of the Cheneler Stress Relaxation Model with Sample Corneal Mechanical Data.	**112**
5.14	Curve Fit of the Kalcioglu-Hu Poroelastic Model with Sample Corneal Mechanical Data.	**113**

6.1	Dresden and Avedro-FDA Corneal Crosslinking Methods: (1) Porcine eye globes are retrieved from a local abattoir. (2) Corneal epithelium is removed using a cotton-tipped applicator. (3) Cornea is placed in 20% Dextran to restore cornea to physiological thickness range. (4) Pachymetry measurements taken to ensure proper thickness restoration. (5) A 30-minute pretreatment of 0.1% riboflavin is performed. (6) Cornea is irradiated with UVA light (for Dresden, the irradiation time and intensity are: 30 minutes at $3mW/cm^2$; for Avedro, the irradiation time and intensity are: 3 minutes at $30mW/cm^2$.	**117**
6.2	Genipin Corneal Crosslinking: (1) Porcine cornea untreated. (2) Porcine cornea post-4 hour treatment in 1% Genipin solution. (3) Porcine cornea after 24 hour equilibrium in 15% Dextran.	**118**
6.3	Average Porcine Corneal Thickness Before and After the Accelerated, Dresden, and Genipin Crosslinking Treatments.	**122**
6.4	Average Thickness Percentage Change Produced by the Crosslinking Treatments.	**122**
6.5	Bar Graphs of the Measured Corneal Young's Moduli for the Experimental Groups. *Left*, Superficial Anterior Stromal Region. *Right*, Middle Anterior Stromal Region.	**122**
6.6	Bar Graph of the Calculated Apparent Viscosities Measured in the Superficial Anterior Stromal Region for the Experimental Groups.	**124**
6.7	Bar Graph of the Calculated Apparent Viscosities Measured in the Middle Anterior Stromal Region for the Experimental Groups.	**124**
6.8	Bar Graphs of the Derived Diffusivity for each Experimental Group. *Left*, Superficial Anterior Stromal Region. *Right*, Anterior Middle Stromal Region.	**125**
6.9	Bar Graph of the Corneal Thickness Before and After the Dresden Crosslinking Procedure.	**134**
6.10	Bar Graph of the Control and Dresden Corneal Young's Modulus for each Eye Pair.	**134**

6.11	The Control and Dresden Corneal Young's Modulus vs Age for the Anterior Stroma, *Left*, and the Posterior Stroma, *Right.*	**135**
6.12	Plot of Factor of Increase vs Age for the Anterior Stroma, *Left*, and the Posterior Stroma, *Right*.	**135**
6.13	Bar Graph of the Control and Dresden Corneal Apparent Viscosity for each Eye Pair.	**135**
6.14	Plot of Control and Dresden Corneal Apparent Viscosity vs Age.	**136**
6.15	Bar Graph of the Calculated Diffusivity for the Control and Dresden Groups. The asterisk sign (*) shown for Eye Pair 4 indicates that the diffusivity could be obtained.	**136**
6.16	Plot of Control and Dresden Corneal Diffusivity vs. Age.	**137**

LIST OF TABLES

2.1	Table of Human Bulk Corneal Young's Modulus of Elasticity reported in Literature	**16**
2.2	Table of Individual Human Corneal Layers' Young's Modulus of Elasticity reported in Literature	**16**
5.1	Table of Coefficients of Determination for the Stress Relaxation Models.	**111**
6.1	Summary Table of Porcine Corneal Elastic, Viscoelastic, and Poroelastic Properties at the Superficial Anterior Stroma Level for all Experimental Groups (* Means Statistically Significant).	**125**
6.2	Summary Table of Porcine Corneal Elastic, Viscoelastic, and Poroelastic Properties at the Middle Anterior Stroma Level for all Experimental Groups (* Means Statistically Significant).	**125**
6.3	Summary Table of Human Corneal Elastic, Viscoelastic, and Poroelastic Properties for the Control and Dresden Corneal Groups.	**137**

PUBLICATION NOTE

The following are publications, presentations, and posters that were published as a direct result of this project:

Peer-Reviewed Publications:

J. Dias and N.M. Ziebarth. **2014**. Impact of Hydration Media on Ex Vivo Corneal Elasticity Measurements. *Eye & Contact Lens: Science and Clinical Practice.* In Press.

J. Dias, V.F. Diakonis, V.P. Kankariya, S.H. Yoo, and N.M. Ziebarth. **2013**. Anterior and Posterior Corneal Stroma Elasticity after Corneal Collagen Crosslinking Treatment. *Experimental Eye Research.* 116: 58-62.

J. Dias and N.M. Ziebarth. **2013**. Anterior and Posterior Corneal Stroma Elasticity Assessed using Nanoindentation. *Experimental Eye Research.* 115:41-46.

Conference Presentations:

J. Dias and N.M. Ziebarth. **2014**. The Effect of Different Corneal Crosslinking Treatment Methods on Corneal Biomechanics. Abstract for Oral Presentation. Aegean Cornea XII Meeting, Santorini, Greece.

J. Dias and N.M. Ziebarth. **2014**. Viscoelastic Characterization of the Corneal Stroma Assessed Ex Vivo using Atomic Force Microscopy. Abstract for Poster Presentation. The Association for Research in Vision and Ophthalmology Conference, Orlando, FL.

C. Labate, **J. Dias**, V. Sueiras, M. De Santo, G. Lombardo, M. Lombardo and N.M. Ziebarth. **2014**. Depth-Dependent Mechanical Anisotropy of the Cornea Assessed by Atomic Force Microscopy. Abstract for Poster Presentation. The Association for Research in Vision and Ophthalmology Conference, Orlando, FL.

F.R. Gonzalez, M. Lorenzo, **J. Dias**, and N. Ziebarth. **2013**. Corneal Mechanical Properties after Crosslinking Treatments for Keratoconus and Post-LASIK Ectasia. Abstract for poster presentation. Biomedical Engineering Society Conference, Seattle, WA.

M. Lorenzo, F. R. Gonzalez, **J. Dias**, N. Ziebarth. **2013**. Investigation of the Efficacy of Genipin Solution as a Possible Treatment for Keratoconus. Abstract for poster presentation. Biomedical Engineering Society Conference, Seattle, WA.

J. Dias and N. Ziebarth. **2013.** Effect of Different Hydration Media on Ex Vivo Corneal Elasticity Measurements. Abstract for poster presentation. The Association for Research in Vision and Ophthalmology Conference, Seattle, WA.

J. Dias and N. Ziebarth. **2012.** Effect of Corneal Crosslinking on Anterior and Posterior Stromal Elasticity Assessed Ex Vivo by Atomic Force Microscopy. Abstract for poster presentation. The Association for Research in Vision and Ophthalmology Conference, Miami, FL.

J. Dias, D. Gonzalez, and N.M. Ziebarth. **2011**. Mechanical Characterization of Multi-Layered Biological Samples using Atomic Force Microscopy. Abstract for oral presentation. Biomedical Engineering Society Conference, Hartford, CT.

J. Dias, C. Yau, V. Moy, J.-M.A. Parel, and N.M. Ziebarth. **2011**. Feasibility of Bulk Corneal Elasticity Measurement with Atomic Force Microscopy: A Pilot Study. Abstract for poster presentation. The Association for Research in Vision and Ophthalmology Conference, Miami, FL.

J. Dias, N.M. Ziebarth, M. Prabakar, L. Lau, C. Rowaan, V.T. Moy, S.H. Yoo, and J.-M.A. Parel. **2010**. Elasticity of Corneas Treated With UVA and Riboflavin Assessed by Atomic Force Microscopy. Abstract for poster presentation. The Association for Research in Vision and Ophthalmology Conference, Miami, FL.

The following are other publications, presentations, and posters related to peripheral projects:

Peer-Reviewed Publications:

L.M. Pacheco, L.A. Gomez, **J. Dias**, N.M. Ziebarth, G. Howard, P.C. Schiller. **2014**. Progerin Expression Significantly Disrupts Critical Adult Stem Cell Functions Required for Tissue Repair. Aging. Accepted.

N.M. Ziebarth, **J. Dias**, V. Hürmeriç, M.A. Shousha, C.B. Yau, V.T. Moy, W.W. Culbertson, S.H. Yoo. **2013**. Quality of Corneal Lamellar Cuts Quantified using Atomic Force Microscopy. *Journal of Cataract & Refractive Surgery*. 39:110-117.

J. Ruiz, D. Pelaez, **J. Dias**, N.M. Ziebarth, H.S. Cheung. **2011**. The Effect of Nicotine on the Physical Properties of Mesenchymal Stem Cells. *Cell Health and Cytoskeleton*.4:29–35.

Conference Presentations:

N.M. Ziebarth, I. Persaud, E. Arrieta, **J. Dias**, E. Lee, C. Rowaan, I. Nose, S. Yoo, and J.-M.A. Parel. **2011**. Efficiency of Coulomb Controlled Iontophoresis for Transcorneal Delivery of Riboflavin: A Pilot Study. Abstract for poster presentation. The Association for Research in Vision and Ophthalmology Conference, Miami, FL.

V. Sueiras, **J. Dias**, C. Yau, E. Arrieta, V.T. Moy, and N.M. Ziebarth. **2011**. Human and Non-Human Primate Lens Capsule Structure Assessed by Atomic Force Microscopy.

Abstract for poster presentation. The Association for Research in Vision and Ophthalmology Conference, Miami, FL.

N.M. Ziebarth, **J. Dias**, M. Prabakar, L. Lau, C. Rowaan, S. Uhlhorn, F. Manns, S. Yoo, and J.-M.A. Parel. **2010**. Corneal Curvature and Thickness after Treatment With UVA and Riboflavin Assessed by Optical Coherence Tomography. Abstract for poster presentation. The Association for Research in Vision and Ophthalmology Conference, Miami, FL.

M. Prabakar, N. Ziebarth, **J. Dias**, L. Lau, C. Rowaan, S. Ulhorn, F. Manns, S. Yoo, and J.-M. Parel. **2010**. Swelling of Corneas Treated With UVA and Riboflavin Assessed by Optical Coherence Tomography. Abstract for poster presentation. The Association for Research in Vision and Ophthalmology Conference, Miami, FL.

CHAPTER 1

SPECIFIC AIMS

The goal of this project is to develop novel instrumentation and techniques to characterize corneal biomechanical properties *ex vivo* using atomic force microscopy (AFM). Corneal biomechanics is an important parameter for designing, developing and improving diagnostic and treatment methods for corneal diseases and glaucoma, including cross-linking for keratoconus, post-LASIK ectasia, and intraocular pressure measurements. Predicting the corneal biomechanical response requires knowledge of the corneal elasticity and viscoelasticity. However, these properties are not fully understood. Published values of such properties lack reproducibility and are acquired using destructive techniques, yielding results that may not reflect the *in situ* corneal behavior. Therefore, a need exists for the development of methodologies capable of accurately assessing corneal tissue elastic and viscoelastic properties in a non-destructive and reproducible manner.

To address this concern, the proposed project will expand the capability of AFM technology to probe corneal mechanical responses at the tissue level. The developed AFM instrumentation and techniques will then be implemented to investigate the effect of corneal crosslinking on corneal biomechanical properties. Corneal crosslinking is one of the most promising treatment options to reduce the progression of keratoconus. It encompasses the use of the photo-sensitizer riboflavin with ultraviolet light to increase corneal mechanical strength. Though this treatment has had positive preliminary results,

an increased comprehension of corneal mechanics is needed to explain how crosslinking alters corneal mechanical strength. The specific aims of this project are:

Aim 1: Develop AFM instrumentation to enable characterization of corneal biomechanical properties.

The simplicity of the AFM principle enables the construction of low-cost, custom-built systems for nanoindentation testing with the unique ability to measure both elastic and viscoelastic properties. Current commercial AFM systems measure mechanics of fully hydrated samples at the nanoscale level, thus being widely used in the field of cell mechanics. However, these systems lack instrumentation flexibility, making increased indentation and viscoelastic characterization difficult. The purpose of this aim is to develop custom instrumentation and techniques capable of corneal elastic and viscoelastic characterization.

Aim 2: Apply contact mechanical models to characterize the corneal biomechanical properties.

Within literature, various indentation-based contact mechanical models have been developed for both non-biological (thin metal films and polymers) and biological (such as the articular cartilage) samples. The goal of Aim 2 is to conduct a thorough, comprehensive study of pre-existing contact mechanical models (developed for both non-biological and biological applications) and apply them to the measured corneal mechanical responses obtained from the instrumentation and techniques developed from Aim 1. Respective elastic, viscoelastic, and poroelastic indentation-based contact

mechanical models will be fitted to the measured corneal mechanical responses to determine which models (elastic, viscoelastic, and poroelastic) best represent the mechanical nature of the corneal tissue. The execution of this goal is divided into the investigation of the elasticity, viscoelasticity, and poroelasticity models and the software development to enable model fitting and comparative analysis.

Aim 3: Apply the developed model and instrumentation to quantify the effect of crosslinking on the biomechanical properties of the cornea.

This aim will apply the instrumentation and analysis procedures developed in Aims 1 and 2 to understand the mechanism of corneal crosslinking by measuring the elasticity and stress relaxation of corneal samples.

CHAPTER 2

BACKGROUND AND SIGNIFICANCE

2.1 Anatomy and Physiology of the Cornea

2.1.1 Overview

The function and structure of the cornea is of significant importance for normal physiological visual capability. Of its two main physiological functions, the cornea is a protective element of the eye (Beuerman and Pedroza 1996, Lens 1999, Trattler 2010, Delmonte and Kim 2011). Positioned at the front of eye globe, the cornea helps to shield the intraocular structures from outer environmental interactions in conjunction with the eye lids, eye socket, tears, and sclera (Beuerman and Pedroza 1996, Trattler 2010, Delmonte and Kim 2011, Institute 2013) (Figure 2.1). The cornea is more commonly known as the primary ocular tissue responsible for between 65 to 75 percent of the eye's refractive or light bending power as it operates like a curved window controlling and focusing the entry of light into the eyes onto the retina (Atchison and Smith 2003, Krachmer *et al.* 2011, Institute 2013). Its transparency enables minimal scattering and reflection of light between the wavelengths of 310nm and 2500nm (Ziebarth *et al.* 2010). With such protective and refractive functions, the physical nature and structure of the cornea are the basis for which this tissue's functions can be fulfilled. The cornea is comprised of five distinct layers: epithelium, Bowman's membrane, stroma, Descemet's membrane, and endothelium (Figure 2.2).

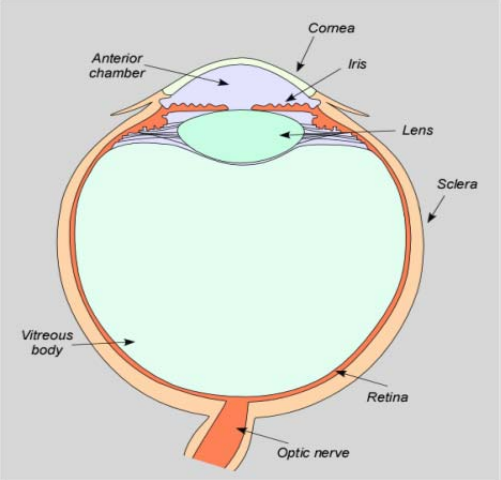

Figure 2.1: Diagram of the Basic Anatomy of the Human Eye Globe (From: Manns, F. BME545, Visual Optics. Lecture 13: Optics of the Eye and Magnifier.)

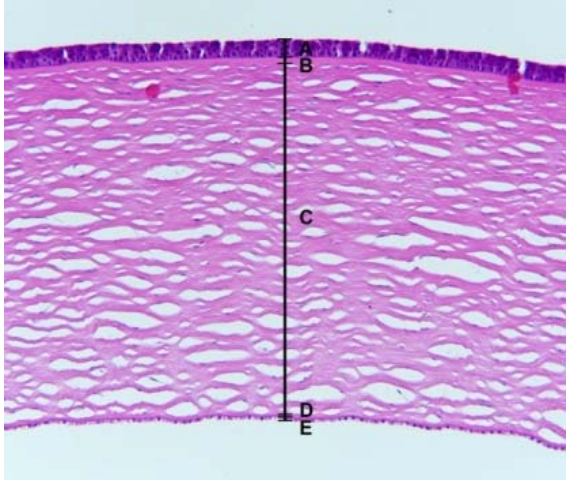

Figure 2.2: Histological section of the human cornea. The cornea is composed of five layers: (A) epithelium, (B) Bowman's membrane, (C) stroma, (D) Descemet's membrane, and (E) endothelium. (From: (Ziebarth *et al.* 2010))

2.1.2 Cellular Layers

The corneal epithelium, characterized as a stratified nonkeratinizing squamous layer, accounts for 10% of the corneal thickness (up to 50µm). Making up the primary layer of the anterior corneal surface, the main functions of the epithelium are to act as a diffusion barrier to water and solutes and as a protective mechanical barrier against microorganisms (Brightbill *et al.* 1986, Trattler 2010, Delmonte and Kim 2011, Krachmer *et al.* 2011). It is this layer, in conjunction with a tear film, which is responsible for the cornea's smooth surface.

The corneal endothelium forms the most internal corneal layer. Its main physiological functions are to maintain the dehydrated state of the cornea and to provide nutrition to the cornea from the aqueous humor (Lens 1999). The corneal endothelium consists of a monolayer of approximately 500,000 hexagonal cells ranging in thickness from 4 to 6µm (Trattler 2010). These cells also aid in forming a diffusive barrier to the

aqueous humor by enabling small molecule and electrolyte transfer between cells while assisting in waste removal and nutrition uptake (Lens 1999, Trattler 2010, Krachmer *et al.* 2011). Unlike the epithelium, corneal endothelial cells neither proliferate nor regenerate; therefore these cells die and slough off with age. Neighboring endothelial cells must then spread out to cover disruptions in the monolayer (Arffa and Grayson 1997, Lens 1999). Thus, it is imperative to keep the endothelial layer intact and unharmed during ocular surgeries (Krachmer *et al.* 2011).

2.1.3 Basement Membranes

Bowman's membrane is an acellular collagenous layer underlying the corneal epithelium and overlying the stroma. Its thickness ranges from 8 to 17.7μm in adult humans (Komai and Ushiki 1991, Wilson and Hong 2000, Tao *et al.* 2011). Bowman's membrane is composed of types I, III, and V collagen fibrils with a uniform diameter range of 20 to 30nm that is much smaller than fibrils within the stroma (Wilson and Hong 2000, Trattler 2010, Krachmer *et al.* 2011). Theses fibrils are randomly oriented forming a densely interwoven network, described as a felt-like sheet, and are also surrounded by proteoglycans called mucoprotein (Komai and Ushiki 1991, Wilson and Hong 2000, Krachmer *et al.* 2011). Moreover, the anterior surface of Bowman's membrane is smooth and distinct from the corneal epithelium, while its posterior border has been shown to be less defined with collagen fibrils forming bundles and merging with fibrils of the stromal layer (Komai and Ushiki 1991, Arffa and Grayson 1997, Lens 1999).

Although the anatomical structure of Bowman's membrane has been extensively studied, its physiological function within the cornea remains inconclusive. Theories

concerning the function of Bowman's membrane include a barrier against microorganisms (Arffa and Grayson 1997), maintaining epithelial uniformity, and sustaining optical stability (Wilson and Hong 2000, Trattler 2010). However, the lack of significant evidence to support such theories coupled with the lack of significant complications for the millions of individuals devoid of Bowman's membrane over their central corneas due to photorefractive keratectomy, suggests to ophthalmic researchers that this corneal layer has no critical function (Wilson and Hong 2000, Trattler 2010). In addition, recent clinical studies have demonstrated that the epithelia can form and are maintained in absence of the Bowman's membrane following excimer laser photoablation (Krachmer *et al.* 2011).

Descemet's membrane functions as the basement membrane of the corneal endothelium and a protective barrier to the rest of the eye (Lens 1999, Krachmer *et al.* 2011). With an average thickness of 10µm in adults, this membrane is comprised of two visually distinct regions: the banded anterior zone and the non-banded posterior zone. Although both regions are formed from secretions of the corneal endothelium, the banded anterior zone is produced during the first four months of gestation with an average thickness of 3µm while the non-banded posterior zone is produced after birth, progressively thickening with age (Beuerman and Pedroza 1996, Arffa and Grayson 1997, Krachmer *et al.* 2011). Descemet's membrane is composed of collagen types IV and VIII along with laminin and fibronectin (Trattler 2010, Krachmer *et al.* 2011). The orientation of the fine collagen fibers within the membrane forms a hexagonal pattern (Lens 1999). Unlike the collagen fibers of Bowman's membrane, those of Descemet's

membrane do not intertwine with the stromal collagen fibrils, thereby creating a distinct delineation from the stroma (Arffa and Grayson 1997, Lens 1999).

2.1.4 Stroma

Comprising approximately 90% of the entire corneal thickness (up to 500µm for the central stroma; (Reinstein *et al.* 2009)), the stromal layer is responsible for the function and optical properties of the cornea as a whole. Its roles include being the principal contributor to light scatter reduction, corneal transparency, corneal mechanical strength, and corneal curvature (Lens 1999, Trattler 2010, Delmonte and Kim 2011, Krachmer *et al.* 2011).

The stromal structure is a matrix of cellular, proteoglycan, and collagenous components. Keratocytes are the predominant cellular components within the stroma. These cells are responsible for the synthesis and maintenance of the collagen fibrils and proteoglycans; in addition, they contain crystallins that aid in reducing the backscatter of light (Delmonte and Kim 2011). Making up about 10% of the stromal volume, keratocytes have a long, flat spindle-like shape and are scattered among the collagen fibers (Trattler 2010, Krachmer *et al.* 2011). In normal conditions, keratocytes are quiescent but become active in response to stromal injury or infection to assist in healing (Lens 1999, Krachmer *et al.* 2011).

Another main structural component of the stroma is proteoglycan, which consists of a non-collagenous protein chain covalently bounded to oligosaccharides and glycosaminoglycan (GAG) side chains (Arffa and Grayson 1997). The two core proteins found within the stroma are lumican and decorin, while the two main stromal GAG side

chains are keratin sulfate and chondroitin/dermatan sulfate (Arffa and Grayson 1997, Trattler 2010). Lumican contains keratin sulfate as its GAG side chain while decorin contains chondroitin/dermatan sulfate as its GAG side chain (Arffa and Grayson 1997). The main functions of these proteoglycans include modulating the formation of collagen fibrils by limiting fibril size and maintaining collagen fibril spacing, while accounting for the stroma's water-holding capacity (Arffa and Grayson 1997, Trattler 2010, Krachmer *et al.* 2011).

The primary stromal constituent is a collagenous network of unique and highly ordered fashion. Individual collagen fibers of the stroma are arranged in parallel bundles known as fibrils (Delmonte and Kim 2011). Such fibrils, made up of complexes of types I and V collagen with uniform diameter (250-300*Å*), further assemble into parallel layers, called lamellae (Arffa and Grayson 1997, Delmonte and Kim 2011). The stroma contains between 200 and 250 such layers. It is the precise yet varied organization of the lamellae throughout the stroma that contributes to the cornea's transparency, curvature, and mechanical strength (Lens 1999, Abahussin *et al.* 2009, Delmonte and Kim 2011).

The internal structure of the stroma is often classified into two regions: anterior stroma and posterior stroma. The anterior stroma region consists of densely-packed interwoven lamellae that run in an oblique and random fashion (Kotecha 2007, Morishige *et al.* 2011). Typical lamellae dimensions within this anterior region include a width range of 0.5-30μm and thickness range of 0.2-1.2μm (Komai and Ushiki 1991). The orientation and structure of the collagen lamellae within the anterior stroma suggests that this region is a key factor in corneal rigidity as well as corneal curvature maintenance (Delmonte and Kim 2011, Morishige *et al.* 2011). As one descends towards more

posterior depths, the lamellae order and structure gradually changes. Unlike the anterior stroma, lamellae of the posterior stroma are more ordered and loosely-packed, have an orthogonal arrangement from limbus to limbus, and run parallel to the plane of the corneal curvature (Bron 2001, Kotecha 2007). The lamellae of this region are also wider (100-200μm) and thicker (1.0-2.5μm) (Bron 2001). Due to these structural characteristics, the posterior stroma is known to have increased hydration and swelling abilities along with a lower refractive index than its anterior counterpart (Turss *et al.* 1971, Freund *et al.* 1995, Patel *et al.* 1995, Bron 2001). Although the organizational differences of the anterior and posterior stromal lamellae result in varied regional properties, this diversity produces the destructive interference of scattered light necessary for corneal transparency (Abahussin *et al.* 2009).

2.2 Corneal Biomechanics

2.2.1 Significance

Although extensive research regarding corneal structure and function has created a strong and cohesive anatomical and physiological foundation for this tissue within the field of ophthalmology, expertise on corneal biomechanics has yet to arrive to the same level of standardization and mastery. Corneal biomechanics is an important field of study functioning to establish a relationship between corneal morphology and physiological function (Dupps and Wilson 2006). A more complete understanding of corneal biomechanics is required if they are to serve as an indication of normal and pathological corneal states. In addition, corneal biomechanics can further the development of effective corneal-related diagnostic and treatment methods.

Improved knowledge of corneal biomechanics would greatly increase the accuracy of corneal simulation models necessary for surgical outcome predictions. Improvement of surgical techniques involved in laser-assisted stromal removal would also ensue, as clinicians performing refractive surgeries like laser in situ keratomileusis (LASIK) and photorefractive keratectomy would enhance their skills in determining the optimal stromal depth that maintains biomechanical stability yet corrects the respective refractive errors for visual restoration. In addition, the advancement of corneal biomechanics would enable more objective standards of postoperative assessments for therapeutic treatments such as crosslinking for keratoconus and post-LASIK ectasia or phototherapeutic keratectomy (PTK) for granular corneal dystrophy (Kamiya, Shimizu *et al*. 2009). Accurate corneal mechanical measurements are necessary for compliance mismatch prevention in the development of corneal transplants (such as keratoprosthesis, corneal onlays, and corneal inlays) (Ruberti *et al.* 2011) while being of significant importance in intraocular pressure determination for effective diagnostic, risk, and treatment techniques for glaucoma (Harada and Naoi 2004, Brown and Congdon 2006, Pepose *et al.* 2007, Mansouri *et al.* 2012).

Due to its prominent thickness and prevalent collagenous composition, it is commonly accepted that the overall mechanical response of the cornea stems from its stromal layer (Dupps and Wilson 2006, Delmonte and Kim 2011, Winkler *et al.* 2011). The gradual changes of the collagen lamellar features and organization between the anterior and posterior stroma suggest a mechanical gradient within the stroma (Randleman *et al.* 2008, Winkler *et al.* 2011). Comprehensive understanding and

quantification of such spatial-mechanical variance within the stroma is necessary for the advancement of corneal biomechanics.

2.2.2 Corneal Biomechanical Testing

Standard biomechanical testing methods to measure human bulk corneas are tensile stretching (or strip extensiometry) (Nash *et al.* 1982, Hoeltzel *et al.* 1992, Seiler *et al.* 1992, Zeng *et al.* 2001, Jayasuriya *et al.* 2003, Wollensak *et al.* 2003), bulge testing (Jue and Maurice 1986, Hjortdal and Ehlers 1995, Hjortdal 1996, Elsheikh *et al.* 2007, Elsheikh *et al.* 2010), and the ocular response analyzer (Luce 2005, Medeiros and Weinreb 2006, Kotecha 2007, Ortiz *et al.* 2007, Pepose *et al.* 2007, Shah *et al.* 2007, Palomino *et al.* 2011). Tensile stretching has become the standard for *ex vivo* corneal elastic modulus determination. This characterization technique involves cutting the cornea into rectangular strips, attaching the lateral ends of the strip onto the clamps of a tension machine, and stretching the corneal strip laterally (Figure 2.3). During stretching, the force exerted to stretch the cornea and the displacement of corneal elongation is recorded to compute stress and strain values. The values are then used to derive mechanical properties such as the Young's modulus and hysteresis behavior of the cornea. However, the mechanical property values (like Young's modulus of elasticity) obtained may be inaccurate due to the technique's destructive tissue preparation that disrupt the native fibril orientations, potential misalignment of grips, inconsideration of corneal curvature, and non-uniform stress distribution applied along the width of the corneal strip during stretching (Elsheikh and Anderson 2005, Ahearne *et al.* 2007, Ruberti *et al.* 2011).

Bulge (or pressure inflation) testing addresses the destructive tissue preparation issue of tensile stretching. It involves placing excised whole corneas within an artificial anterior pressure chamber, where internal pressure (deemed as the source of stress) is exerted onto the posterior surface of the cornea, with the use of a saline solution (Figure 2.4). As force is applied onto the cornea, a pressure transducer monitors and records the pressure. Simultaneously, the displacement taking place at the corneal apex is also measured and recorded using an optical instrument (either a laser beam or camera system) to help calculate the resultant strain. Nonetheless, possible limitations of this experimental method include difficulty in maintaining experimental controls such as controlling applied pressure onto the cornea and pressure leaking issues (Ahearne *et al.* 2007, Ruberti *et al.* 2011).

The Ocular Response Analyzer (ORA) is the standard *in vivo* corneal biomechanical characterization method used in the clinical setting. The ORA exerts a high-speed air puff onto the cornea that results in consequent corneal deformation. The deformation of the cornea is recorded by an electro-optical system that measures the applanation pressure signals when the cornea deforms inwardly at the onset of the air-puff and when it returns back to its original state (Figure 2.5). The two pressure signals are then used to calculate measurements including two biomechanical parameters (Reichert 2009): (1) Corneal Hysteresis (CH), which is a measure of viscous damping within the cornea and (2) Corneal Resistance Factor (CRF), which is a measure of the overall corneal resistance. The main drawback with these biomechanical parameters is the lack of established correlations to standard mechanical property measurements like

stress, strain, and Young's modulus of elasticity to enable direct comparison (Ahearne *et al.* 2007).

Researchers are striving to develop new nondestructive experimental techniques for corneal characterization. Such characterization methods include shear wave propagation (Dupps *et al.* 2007, Liu *et al.* 2007, Tanter *et al.* 2009, Li *et al.* 2012), optical coherence elastography (Ford *et al.* 2006, Ford *et al.* 2011), Placido imaging (Grabner *et al.* 2005, Dorronsoro *et al.* 2012), interferometry (Jaycock *et al.* 2005), Brillouin optical microscopy (Scarcelli *et al.* 2012), and ultrasound (Wang *et al.* 1996, Hollman *et al.* 2002). These forthcoming techniques strive to address the need for *in vivo* corneal characterization with the use of light or sound waves, but they do not provide a direct measure of standard mechanical properties.

Using the aforementioned characterization techniques to probe corneal mechanical properties, a large range of reported corneal Young's modulus of elasticity values (0.667 kPa – 41MPa) exists within literature (Tables 2.1 and 2.2). Such large variability is believed to be due to the varied nature of the characterization methods used. For example, the application of tensile (in the case of tensile stretching) and radial (in the case of Pressure-Inflation loading) forces onto the cornea result in mechanical responses that are unique. Other factors creating this large range include differences in sample preparation, corneal hydration, age, and post-mortem time.

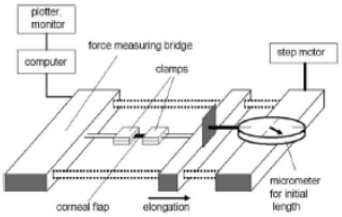

Figure 2.3: Schematic of Tensile Stretcher (Kohlhaas *et al.* 2006)

Figure 2.4: *Left,* Schematic of a corneal inflation rig. *Right,* Picture of a Bovine Cornea placed onto an Inflation Rig (Boyce *et al.* 2008).

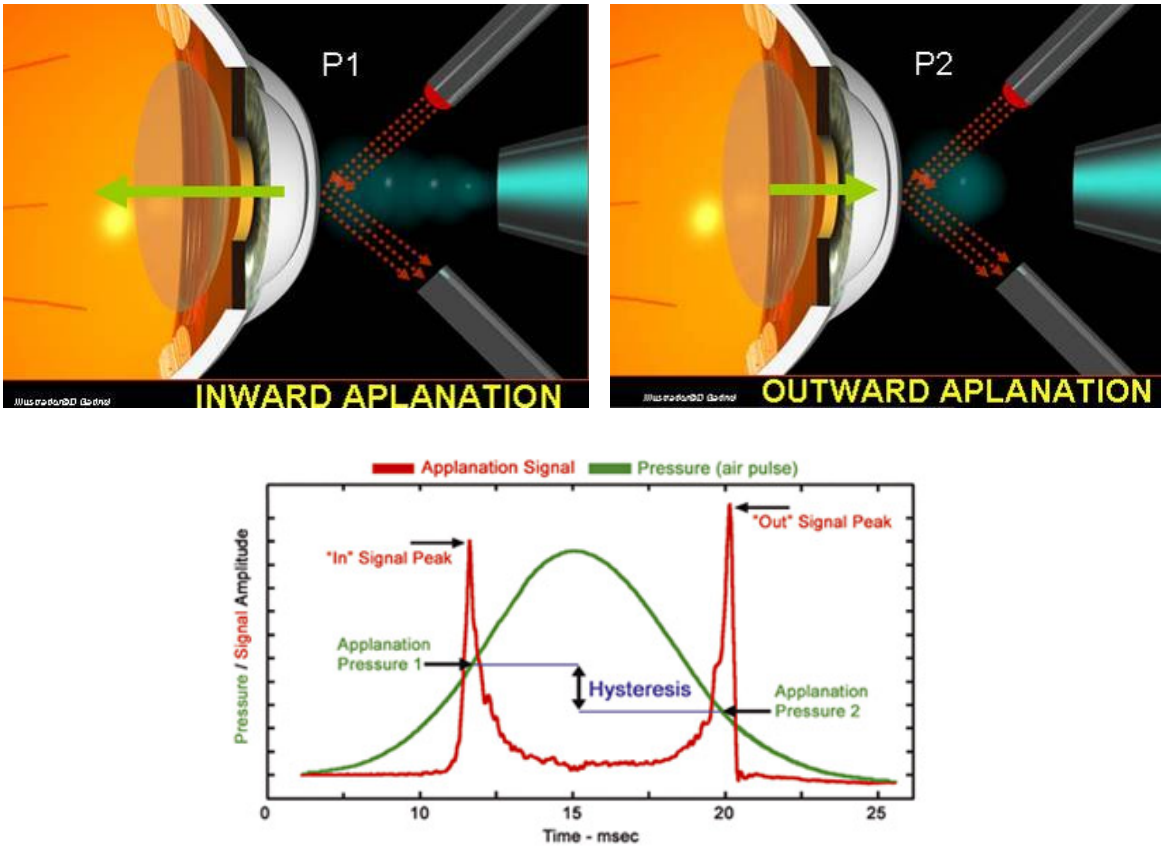

Figure 2.5: Diagram of the Ocular Analyzer Response Principle and Waveforms (http://www.gatinel.com/wp-content/uploads/2010/01/ocular-response-analyzer-normal.jpg and (Reichert 2009))

Characterization Method	Bulk	Young's Modulus of Elasticity (MPa)	Reference
Shearing interferometers	Bulk	0.27 (20yo)- 0.52 (100yo)	Cartwright 2010
Pressure-Inflation Testing	Bulk Central region (pressure dependent)	2.87 – 19.5	Hjortdal 1996
Pressure-Inflation Testing	Bulk (age and pressure function)	0.159 - 0.961	Elsheikh 2007
Pressure-Inflation Testing	Bulk	2.52 - 15.2	Hjortdal and Ehlers 1995
Ultrasound	Bulk	5.3 - 20	Wang 1996
Tensile Stretching	Bulk	3.40 – 41.0	Hoeltzel 1992
Tensile Stretching	Bulk	0.30 – 6.0	Jayasuriya 2003
Tensile Stretching	Bulk	3.81 ± 0.40	Zeng 2001
Tensile Stretching	Bulk	0.8 – 2.2	Wollensak *et al*, 2003

Table 2.1: Table of Human Bulk Corneal Young's Modulus of Elasticity reported in Literature

Characterization Method	Corneal Layer	Young's Modulus of Elasticity (MPa)	Reference
Tensile Stretching	Anterior Cornea	3.6	Kohlhaas 2006
Indentation Testing	Anterior Cornea	0.8919 – 2.583	Winkler 2011
Indentation Testing	Mid Stroma	0.336 – 1.240	Winkler 2011
AFM	Anterior Stroma	0.0331 ± 0.0061	Last 2012
AFM	Anterior Stroma	1400 - 2630	Lombardo 2012
Tensile Stretching	Posterior Cornea	1.3	Kohlhaas 2006
Indentation Testing	Posterior Cornea	0.3645 – 1.273	Winkler 2011
AFM	Anterior Basement membrane	0.0075 ± 0.0042	Last 2009
AFM	Descemet's membrane	0.05 ± 0.0178	Last 2009
AFM	Bowman's membrane	0.1098 ± 0.0132	Last 2012

Table 2.2: Table of Individual Human Corneal Layers' Young's Modulus of Elasticity reported in Literature

2.3 Corneal Crosslinking

2.3.1 Clinical Need

Keratoconus is the most common corneal dystrophy in the United States with an incidence of 1 in every 2,000 Americans, spanning all genders and ethnicities with prevalent diagnosis in the younger population (Kuo *et al.* 2006, Mazzotta *et al.* 2007, Romero-Jimenez *et al.* 2010, Dahl *et al.* 2012, Institute 2013). This disease can be characterized by abnormal corneal thinning and steepening as atypical changes in collagen structure, organization, and intercellular matrix within the corneal stromal occurs (Mazzotta *et al.* 2007, Cheema *et al.* 2012, Dahl *et al.* 2012, Hovakimyan *et al.* 2012) (Figure 2.6). Such irregularities contribute to the progressive corneal mechanical instability and the development of visual impairment that is associated with keratoconus (Krachmer *et al.* 1984, Hovakimyan *et al.* 2012). It was found that the stiffness of keratonic corneas is only 50% to 60% that of normal corneas (Andreassen *et al.* 1980).

Treatment methods for keratoconus have included medical and surgical procedures designed to restore visual acuity to persons with keratoconus. The usual first-line treatment is the use of rigid-gas permeable (RGP) contact lenses, which allow oxygen transmission; although these lenses improve visual acuity, the irregular shape of the cornea due to keratoconus makes it challenging for proper lens fitting (Hovakimyan *et al.* 2012). When contact lens intolerance is experienced, intrastromal corneal ring segment (Intacs) implantation is then considered. This procedure involves the insertion of implants within the stromal bed to reduce the corneal curvature, thus addressing the refractive compromises due to keratoconus. However, post-implant complications like epithelial defects, anterior and posterior perforations, improper implant placement, and

stromal thinning are possible (Hovakimyan *et al.* 2012). Finally, for those with severe, advanced stages of keratoconus, penetrating keratoplasty (PK) is the only remaining option. PK is a type of corneal transplantation that involves the trephination and grafting of a donor central cornea that is used to replace a patient's compromised central cornea. Nonetheless, problems of low donor cornea supply, reduced corneal sensitivity, and the recurrence of keratoconus due to continual thinning of the peripheral stroma exists with this procedure (Hovakimyan *et al.* 2012).

Although RGP contact lenses, Intacs, and PK correct the refractive errors of keratoconus, these treatment methods fail to combat the disease's progression (Wollensak *et al.* 2003, Wollensak 2006). For this reason, researchers sought a way to address the progressive corneal changes associated with keratoconus while attempting to avoid the need for penetrating keratoplasty (Wollensak *et al.* 2004, Mazzotta *et al.* 2007, Cheema *et al.* 2012). In the late 1990s, a German research group from Dresden Technical University conceived the treatment approach of corneal crosslinking (Spoerl *et al.* 1998, Mazzotta *et al.* 2007). To date, corneal crosslinking is the only treatment method designed to arrest keratoconus progression (Wollensak 2006, Hovakimyan *et al.* 2012).

2.3.2 Theory

The mechanical strength of the stroma is dependent upon the formation of collagen crosslinks through enzymatic and non-enzymatic processes. Once collagen is synthesized by keratocytes and begins fibril and fiber formation, an enzyme-regulated process involving lysyl oxidase causes the oxidation of the amino acids lysine and hydroxylysine to their respective aldehydes; condensation of the aldehydes then occurs,

resulting in intra- and intermolecular crosslinks (Hovakimyan *et al.* 2012). The non-enzymatic mechanism of collagen crosslinking is glycation (or non-enzymatic glycosylation), which is the covalent bonding of a protein with a sugar molecule. Thus, in the case of the stroma, collagen is covalently crosslinked with glucose, found in the interstitial space. This glycation-mediated crosslinking is known to be the main attributor of the increase in corneal strength with age (Dahl *et al.* 2012).

In keratoconus, the microscopic link to decreased corneal mechanical strength is the reduced number in stromal collagen crosslinks and molecular bonds between stromal proteoglycans (Hovakimyan *et al.* 2012). For this reason, researchers strived to develop a method to induce additional crosslinks in the stroma. The research group at Dresden Technical University, led by Theo Seiler, found their breakthrough when it was noted that diabetic patients did not develop keratoconus due to the prevalence of glycation-mediated crosslinking with glucose, which strengthen stromal tissue (Seiler *et al.* 2000, Mazzotta *et al.* 2007, Dahl *et al.* 2012, Hovakimyan *et al.* 2012). Thus, their goal was to replicate a similar crosslinking effect in non-diabetic corneas (Dahl *et al.* 2012). Corneal crosslinking is the result of primary studies in photobiology intended to identify biological glues that could increase the stromal collagen strength when activated by light or heat, upon which riboflavin was decided (Khadem *et al.* 1994, Spoerl and Seiler 1999, Mazzotta *et al.* 2007, Dahl *et al.* 2012).

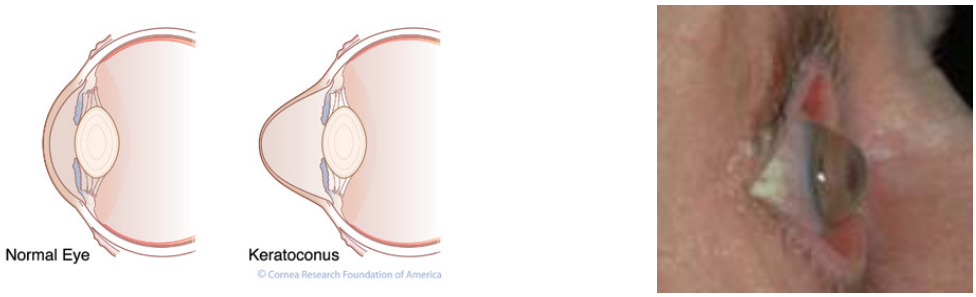

Figure 2.6: Diagrams of a normal and keratoconic cornea. (From: Cornea Research Foundation of America; http://www.cornea.org/index.php/research/corneal_conditions/keratoconus/)

2.3.3 Technique

Corneal crosslinking uses riboflavin and ultraviolet irradiation (UVA) to induce photo-oxidative crosslinking of stromal collagen to increase the rigidity of stromal collagen fibers and the overall mechanical strength of the stromal layer. Riboflavin (vitamin B2) functions as the photosensitizing agent that increases the absorption coefficient of the cornea so that crosslinking can take place; upon ultraviolet exposure, riboflavin excites to a triple state, releasing reactive oxygen species within the stroma (Wollensak *et al.* 2010, Iseli *et al.* 2011). These free radicals cause crosslink formations between the amino acids of the collagen chains at the intra-helical, inter-helical, and inter-microfibrillar levels (Abad and Panesso 2008), causing an increase in collagen fiber diameter and subsequent mechanical stiffness of the collagen (Wollensak *et al.* 2004). Riboflavin also serves as a protective substance, limiting UVA penetration to the stromal layer, thereby avoiding photo-oxidative damage to the underlying endothelium and other intraocular structures (Wollensak *et al.* 2010). The general procedure of corneal crosslinking involves the removal of the corneal epithelium, a pre-treatment of 0.1% riboflavin solution (in 20% dextran) via drops onto the cornea every 2 to 5 minutes for total of 30 minutes to ensure riboflavin penetration into the stromal layer, and a 30

minute treatment of UVA irradiation (370nm; 3mW/cm^2) with simultaneous drops of 0.1% riboflavin solution every 2 to 5 minutes to maintain corneal hydration (Figure 2.7). This procedure, originating from Dresden Technical University, is known as the standard corneal crosslinking procedure.

Researchers and companies have recently been working to improve the effectiveness and clinical feasibility of the standard corneal crosslinking procedure. Such efforts have resulted in the development of accelerated corneal crosslinking protocols. Utilizing the Bunsen-Roscoe law of reciprocity in which energy density is equivalent to irradiance multiplied by exposure time (density = irradiance x exposure time), these accelerated techniques maintain the original energy density of the standard corneal crosslinking procedure (5.4J/cm^2) by creating different combinations of irradiance levels and exposure time lengths (Touboul *et al.* 2012, Hammer *et al.* 2014). In Europe, where corneal crosslinking has been approved for clinical use, the commercial corneal crosslinking device used is the CCL-Vario (Peschke Medizintechnik GmbH). This corneal crosslinking system offers clinicians the option of choosing between three distinct irradiance-exposure time settings, all of which still maintain the standard corneal crosslinking protocol (total energy dose of 5.4 J/cm^2). The irradiance-exposure time combinations are:

3mW x 1800 seconds (30 minutes) = 5.4 J/cm^2

9mW x 600 seconds (10 minutes) = 5.4 J/cm^2

18mW x 300 seconds (5 minutes) = 5.4 J/cm^2

Within the United States, the corneal crosslinking technique is currently undergoing Food and Drug Administration (FDA) clinical trials for approval. Avedro, a

biopharmaceutical company spearheading these investigations, has also developed an accelerated crosslinking technique that is being implemented within FDA clinical trials. Using Avedro' s commercial corneal crosslinking device known as the KXL system, the Avedro crosslinking protocol uses an increased energy dose of 7.2J/cm^2 through the irradiance-exposure time combination of 30mW/cm^2 for 4 minutes. In addition to using an increased energy dose compared that of the standard crosslinking procedure, the Avedro protocol also uses a higher concentration of riboflavin solution (0.12%) commercially known as VibeX (Avedro, Waltham, MA). The Avedro protocol first subjects the cornea to a 10 minute pretreatment of 0.12% riboflavin (VibeX, Avedro, Waltham, MA) and then UVA irradiation (30mW/cm^2 at 365nm) for 4 minutes.

2.3.4 Importance of Biomechanical Testing for Corneal Crosslinking

With the intended goal to strengthen the intrinsic mechanical properties of corneal collagen, the evaluation of corneal crosslinking's ability to fulfill its purpose is of much importance. Among the various methods to test the efficacy of this treatment method, biomechanical characterization provides an objective and quantitative measure to assess the degree of crosslink formation after the crosslinking procedure. For this reason, studies have been conducted measuring the biomechanical effect of the crosslinking procedure on the cornea (Spoerl *et al.* 1998, Spoerl and Seiler 1999, Wollensak *et al.* 2003, Kohlhaas *et al.* 2006, Tanter *et al.* 2009, Wollensak and Iomdina 2009, Wollensak and Iomdina 2009, Kling *et al.* 2010, Lanchares *et al.* 2011, Schumacher *et al.* 2011, Cartwright *et al.* 2012, Kling *et al.* 2012, Scarcelli *et al.* 2012, Beshtawi *et al.* 2013, Dias *et al.* 2013, Roy *et al.* 2013, Wernli *et al.* 2013, Beshtawi *et al.* 2014, Hammer *et al.*

2014, Lombardo *et al.* 2014, Marcos *et al.* 2014). Researchers have consistently demonstrated the qualitative trend of a statistically significant increase in corneal stiffness when riboflavin-UVA treated corneas are compared to their untreated counterparts (Spoerl *et al.* 1998, Spoerl and Seiler 1999, Wollensak *et al.* 2003, Kohlhaas *et al.* 2006, Tanter *et al.* 2009, Wollensak and Iomdina 2009, Kling *et al.* 2010, Lanchares *et al.* 2011, Schumacher *et al.* 2011, Cartwright *et al.* 2012, Scarcelli *et al.* 2012, Beshtawi *et al.* 2013, Choi *et al.* 2013, Dias *et al.* 2013, Sondergaard *et al.* 2013, Beshtawi *et al.* 2014, Lombardo *et al.* 2014). Of the characterization studies performed to quantify the efficacy of the crosslinking treatment, some have been conducted using human corneas *ex vivo* (Wollensak *et al.* 2003, Kohlhaas *et al.* 2006, Cartwright *et al.* 2012, Beshtawi *et al.* 2013, Choi *et al.* 2013, Dias *et al.* 2013, Sondergaard *et al.* 2013, Beshtawi *et al.* 2014, Lombardo *et al.* 2014). The characterization techniques used in these studies to derive corneal stiffness included tensile stretching (Wollensak *et al.* 2003, Kohlhaas *et al.* 2006, Sondergaard *et al.* 2013), atomic force microscopy (Choi *et al.* 2013, Dias *et al.* 2013), inflation testing (Lombardo *et al.* 2014), scanning acoustic microscopy(Beshtawi *et al.* 2013, Beshtawi *et al.* 2014), and radial spectral speckle pattern interferometry(Cartwright *et al.* 2012). Despite the differences in characterization method nature, all of these studies demonstrated an increase in corneal stiffness for treated corneas compared to their control counterparts with a factor of increase ranging from 1.051 to 4.5. In addition, it was revealed that the majority of the stiffening effect of the crosslinking procedure occurred in the anterior stromal region, therefore demonstrating the depth-dependence (Kohlhaas *et al.* 2006, Dias *et al.* 2013, Sondergaard *et al.* 2013). These studies have provided significant evidence regarding the positive

treatment efficacy of the crosslinking procedure; however, it would be of interest to enhance comprehensive insight on the efficacy of corneal crosslinking by conducting experiments that would provide: (1) a more thorough depth-dependent analysis of the crosslinking effect on the biomechanical properties of stromal layers and (2) an age-dependent analysis of the crosslinking effect on the corneal biomechanical properties.

2.4 Biomechanical Measurements using Atomic Force Microscopy

2.4.1 Background

The Atomic Force Microscope (AFM) was developed by Binnig *et al* as a modification of the scanning tunneling microscope (STM) to study conductor and insulator surfaces on an atomic scale (Binnig *et al.* 1986). The AFM extends the capability to map the surfaces of various samples, regardless of material conductivity (Binnig *et al.* 1986). The atomic force microscope profiles sample surfaces with a sharp cantilever tip of an ultra-small mass (10^{-10} kg) and measures the atomic force (10^{-18}N) created by minute distances between the tip and sample of interest. The creation of surface topographical images requires the maintenance of a constant atomic force correlative to a constant distance between the tip and sample surface (Binnig *et al.* 1986, Tomanek *et al.* 1989). Such maintenance is achieved with the use of a piezoelectric element serving as the feedback mechanism component to manipulate the height of the cantilever beam.

Figure 2.7: Picture of a riboflavin-UVA irradiation treatment administered to a patient (Wollensak *et al.* 2003)

2.4.2 Mechanical Characterization

In addition to providing surface topographical imaging, the AFM can also measure the biomechanical properties of elasticity and viscoelasticity. AFM instrumentation can characterize sample elasticity by implementing the principle of nanoindentation (Overney *et al.* 1992, Wu *et al.* 1998, Wojcikiewicz *et al.* 2003). Nanoindentation involves the contact between the cantilever tip and sample of interest, in efforts to determine resultant force and indentation responses. The AFM cantilever tip is lowered onto the sample at a pre-determined rate, using a piezoelectric actuator. As the cantilever tip comes into contact with the sample, it will undergo a certain degree of deflection (or bending) depending upon the compliance of the sample: the harder the sample is, the more deflection the cantilever tip will experience. The bending of the cantilever corresponds to the amount of force exerted on the sample by the tip. The occurrence of cantilever deflection is also coupled with cantilever indentation, based on the vertical displacement of the piezoelectric actuator. However, unlike the cantilever tip deflection, the cantilever tip indentation upon the sample is inversely proportionate to sample's compliance: the harder the sample is, the less the cantilever tip can indent upon the sample. The cantilever deflection and indentation recorded from the cantilever tip-

sample interaction can be translated into force-indentation curves, after the calibration of the cantilever deflection on a hard surface is taken into account. Once force-indentation curves are acquired, contact mechanical models can be used to derive the Young's modulus of elasticity based on the cantilever tip geometry: spherical (Hertz model; (Hertz 1881)), conical (Sneddon model; (Sneddon 1965)), or pyramidal (Bilodeau and Rico model; (Bilodeau 1992, Rico *et al.* 2005)).

With the fact that most biological tissues possess both elastic and viscous attributes, it is important that viscoelastic measurements are conducted for complete biomechanical characterization (Fung 1993). The two common viscoelastic testing techniques are stress-relaxation and creep response. Stress-relaxation is the phenomenon in which constant strain results in a decrease of the stress with time, while creep is the phenomenon in which constant stress applied to a viscoelastic body results in continual deformation or strain (Fung 1993). Both phenomena have been incorporated using commercial AFMs. For stress-relaxation testing, the cantilever tip displacement is kept constant on the sample, while the decrease of force, corresponding to stress, is recorded over time (Darling *et al.* 2006). On the other hand, the measurement of creep response is the application of a constant force on the sample as the cantilever displacement, corresponding to sample deformation, is recorded over time (Vadillo-Rodriguez *et al.* 2008). However, the simplest way to determine viscoelastic properties of biological tissues is to subject the sample to periodic oscillation, which results in a frequency-dependent response (Fung 1993). The traditional analyzers that use this method to determine the complex elastic modulus and phase lag are dynamic mechanical analysis

and rheometers; however, the modification of custom AFMs as a nanorheometer has extended its capability to perform like its macroscale counterparts (Mahaffy *et al.* 2004).

Atomic force microscopy allows localized mechanical sample testing in aqueous solutions without prerequisite sample alterations (Karrasch *et al.* 1994, Lal and John 1994). This capability enables not only the acquirement of biomechanical measurements in near physiological conditions but also addresses the issues of proper tissue hydration and sample integrity. This is of particular significance for accurate measurement of corneal biomechanics as the level of corneal hydration affects the subsequent quantitative values of the mechanical parameters. In addition, the simplicity of the AFM principle also enables the construction of low-cost custom-built systems for nanoindentation testing. Such custom-built AFMs have the unique ability to measure both elastic and viscoelastic measurements over a large range of length scales. Such capabilities demonstrate the versatility of AFM, permitting the ability to characterize the distinct layers of the cornea and perform depth-dependent characterization studies.

CHAPTER 3

MEASUREMENT PROTOCOL FOR CORNEAL BIOMECHANICAL EXPERIMENTATION

3.1 Purpose

The effectiveness of an *ex vivo* corneal biomechanical characterization technique lies in its ability to most accurately reflect the tissue's *in vivo* behavior. One major factor related to achieving such efficacy is the tissue preparation performed. By minimizing corneal tissue alteration and simulating near-physiological conditions during measurement acquisition, the subsequent *ex vivo* mechanical results should be a close representation of the *in vivo* mechanical response. Although corneal biomechanics has emerged over the last few decades, experimental standardization of *ex vivo* corneal characterization has not yet been established. Many different corneal sample preparation methods exist to accommodate the respective biomechanical characterization technique used. Therefore, the purpose of this chapter is to develop a method to enable accurate *in situ* corneal biomechanical characterization using Atomic Force Microscopy.

3.2 Corneal Holder

Within literature, many researchers perform corneal mechanical characterization testing on corneal strips or buttons since this provides more manageability of the sample. However, such alterations may affect the mechanical response attained. If the entire cornea is left intact, the original collagen fiber orientation is retained and lateral diffusion in areas where the corneal excisions are performed is prevented. In efforts to obtain

reliable biomechanical measurements using Atomic Force Microscopy, a custom corneal sample holder was designed and developed.

The holder developed consists of two parts and provides sturdy anchoring of an intact cornea by laying the cornea flat on the base of the holder and then positioning the top piece of the holder upon the cornea to anchor the cornea in place, using a twist-lock locking mechanism (Figure 3.1). In addition to eliminating corneal sample alterations, this corneal holder also maintains the tissue's curvature. The center of the corneal holder's base contains a customized insert for an uncoated plano-convex optical lens (Edmund Optics, #45-079, 6.0mm diameter, 15.0mm focal length) with 7.75mm radius of curvature, closely matching that of the human cornea (7.8mm; (Bron *et al.* 1997)). It is upon this lens that the apex of the corneal sample is positioned to ensure that only the central corneal region of interest comes into contact with the AFM cantilever for biomechanical measurement. The base of the holder was manufactured at a depth of 11mm to enable complete submersion of the corneal sample in hydration media for maintenance of its physiological thickness. The holder was designed in SolidWorks (Dassault Systèmes SolidWorks Corporation, Waltman, MA) and rapid prototyped with VeroWhite resin material (Figure 3.1 and 3.2).

Figure 3.1: SolidWorks Rendition of the Custom Corneal Holder with the Anchoring Top and the Base Assembled.

Figure 3.2: Custom Corneal Holder. *Left*: Picture of the Anchoring Top and the Base Disassembled. Right: Picture of Anchoring Top and Base Assembled.

3.3 Tip Modification

Commercially available AFM cantilever tips are typically less than 50nm in diameter and are therefore limited to mechanical characterization of individual tissue constituents. To measure tissue level mechanical properties of soft tissues using indentation testing, it has been determined that a contact area greater than 50μm in diameter is required (Ebenstein and Pruitt 2004, Ebenstein and Pruitt 2006). With the intent of characterizing the cornea at the tissue-level rather than at the nanoscale level, AFM cantilevers were modified with glass microspheres. An adapted version of the Abdulreda and Moy (2007) tip modification protocol was implemented. Tipless AFM cantilever tips (nominal spring constant range: 1 - 4.5 N/m, NSC12 series, Mikromasch, San Jose, CA) were modified with glass microspheres (50-100μm diameter, 15926-100, Polysciences Inc., Warrington, WA) by using a water-resistant two-part epoxy adhesive (Loctite Epoxy Heavy Duty Glue) to manually attach a microsphere onto the cantilever tip with the aid of an inverted optical microscope (Carl Zeiss Stemi-2000C). Using a pointed glass capillary tube (0.78mm diameter, G100TF-6, Warner Instruments, Hamden, CT), the epoxy adhesive was placed onto the cantilever tip with much precaution to not cover the tip's reflective backside. Afterward, a glass microsphere was lifted with another

capillary tube and placed onto the tip. The modified tip was then allowed to dry overnight (Figure 3.3). The use of these modified cantilevers increases the surface contact area with the corneal sample, thereby enabling networks of the stromal tissue microstructure to be mechanically probed rather than individual collagen components of the stroma.

Accurate determination of the cantilever's spring constant is of particular significance when using cantilevers with modified tips. The value of the cantilever's spring constant greatly influences the force measurements and consequent outcome of elasticity values obtained. When a microsphere is attached to an AFM cantilever, its weight coupled with the application of epoxy glue to adhere it alters the nominal spring constant prescribed to the cantilever, producing further stiffening. For this reason, it is important to calibrate the modified cantilever rather than just assume the spring constant to be equivalent to the nominal spring constant of the unmodified cantilever.

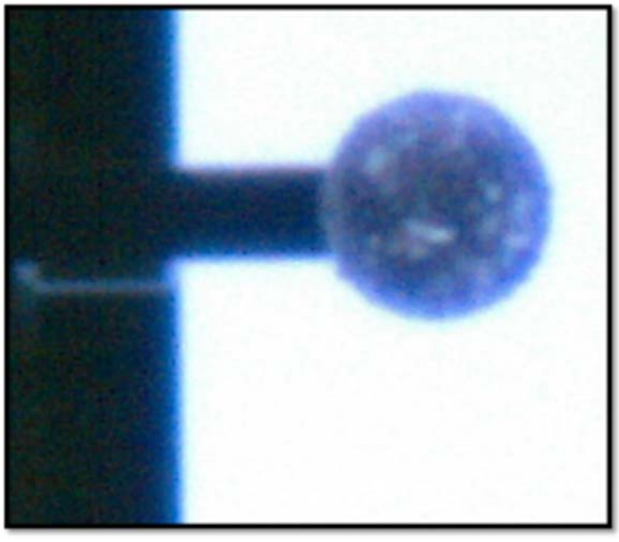

Figure 3.3: Picture of Modified AFM tip with microsphere.

The most common method to calibrate AFM cantilevers was developed by Hutter and Bechhoefer (1993). This method assumes that an AFM cantilever can be likened to a simple harmonic oscillator with one degree of freedom (Hutter and Bechhoefer 1993). Therefore, using the equipartition theorem, the spring constant of the AFM cantilever, *k*, can be determined by measuring the mean square of its thermal fluctuations:

$$k = \frac{k_B T}{\langle x^2 \rangle} \qquad \text{Eq. 3.2}$$

where k_B is Boltzmann's constant (1.380658 x 10^{-23} Nm/K), T is temperature (in Kelvins), and ‹χ2› is the mean square of the cantilever's deflection (in square meters). The mean square of the cantilever's deflection can be experimentally obtained by recording the power spectral density of the cantilever's fluctuation, fitting the power spectrum to a Lorenz fit, and then integrating the area under the curve-fit at the cantilever's resonant frequency.

Although the Hutter and Bechhoefer (1993) method is easy and quick in implementation, this calibration technique could not be used to determine the spring constant of the modified AFM tips. The thermal noise method is an optimal technique for softer cantilevers because these cantilevers have significant and large thermal fluctuations. However, the accuracy of the method decreases with stiffer cantilevers, as in the case of the modified tips, because stiffer cantilevers (having a larger *k*) experience fewer thermal fluctuations (having a smaller ‹χ2›) (as evident with Eq. 3.2) to the point where motion can fall below the detection sensitivity of the position-sensitive photodiode. In addition, limitations of the AFM hardware make the Hutter and

Bechhoefer (1993) method unable to calibrate the modified tips. According to the equation of one-dimensional harmonic oscillating motion:

$$f = \frac{1}{2\pi}\sqrt{\frac{k}{m}} \qquad \text{Eq. 3.3}$$

where *f* is the resonant frequency, *k* is the spring constant of the oscillating body, and *m* is the mass of the oscillating body; at a set mass, an increase in the object's spring constant yields an increase in its resonant frequency. Consequently, the stiffer (greater in *k* value) an AFM cantilever is, the higher its resonant frequency (*f*). The nominal spring constant range of the tipless AFM cantilevers used for glass-microbead modification is 1-4.5 N/m with a resonant frequency range of 90 – 150 kHz (NSC12 series and NSC36 series, Mikromasch, San Jose, CA). According to the Nyquist-Shannon theorem, the AFM's data acquisition system would need to sample at a rate double the resonant frequency of these cantilevers for complete resolution, thereby requiring a minimum sampling rate of 300 kHz. However, the maximum sampling rate capacity of the custom AFM's data acquisition system (ITC-18/PCI, Instrutech, Port Washington, NY) is 200 kHz. This limitation coupled with the fact that attachment of the glass microbeads using epoxy glue produces further stiffening of the cantilever, which further increases the resonant frequency range of the modified tips, produced the need to consider a new spring constant determination technique.

The technique chosen to calibrate the modified tips is the reference cantilever method, which is a widely used static calibration method to determine the cantilever spring constant (Ohler , Gibson *et al.* 1996, Slattery *et al.* 2013). With ease of applicability, the reference cantilever method can be used to calibrate a variety of

cantilever types (with regards to shape, coating, and tip geometry) with a wide range of cantilever spring constants (Ohler , Gates and Reitsma 2007, Slattery *et al.* 2013). It is also advantageous in the sense that using this method negates the need for precise information of the cantilever dimensions and material properties (Gates and Reitsma 2007).

The reference cantilever method entails calibrating a cantilever of unknown spring constant by measuring its deflection when pressed against an accurately calibrated cantilever with a known spring constant. To perform this calibration, the modified cantilever tip of unknown spring constant is placed into a custom cantilever holder, which is made out of VeroWhite resin and fixates the cantilever at a 15^{o} angle to ensure that only the tip comes into contact with the sample of interest and not the holder (Figure 3.4). The calibrated reference cantilever with known spring constant is anchored onto the bottom of a Petri dish using double-sided tape; the Petri dish is then filled with deionized water and placed under the AFM system. Deflection measurements of the uncalibrated cantilever must be respectively performed on a: (1) rigid surface, which, in this case, is done on the silicon base of the reference cantilever and (2) known location of the reference cantilever, which, in this case, is done as close to its end as possible (Gates and Reitsma 2007).

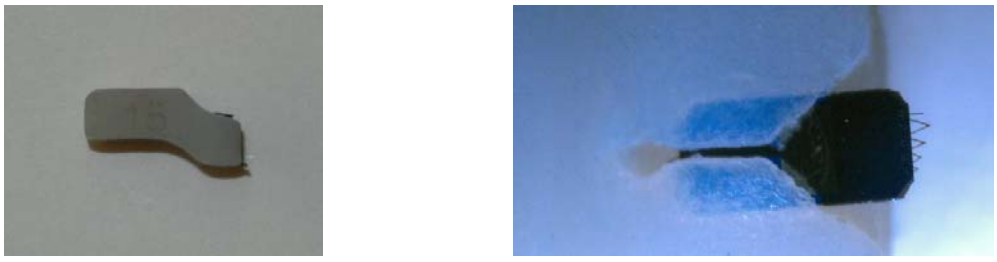

Figure 3.4: *Left,* Side View of Cantilever Holder. *Right,* Close up of Cantilever Anchored in Holder.

The first deflection measurement, on the rigid surface, is performed to determine the correlation between the photodiode voltage and piezoelectric actuator displacement through the cantilever deflection; the second deflection measurement is conducted to relate the first deflection correlation to the deflection of the uncalibrated cantilever to the reference cantilever (Gibson *et al.* 1996, Gates and Reitsma 2007, Clifford and Seah 2009) (Figures 3.5 and 3.6). For both deflection measurement scenarios, deflections were respectively conducted with the indentation voltage set to 1000mV and performed 5 times, then averaged. The spring constant of the uncalibrated modified cantilever, *k*, can then be calculated using:

$$k = k_{ref}\left(\frac{S_{ref}}{S_{hard}} - 1\right)\left(\frac{L_{ref}}{L_{ref}-\Delta L}\right)^3 cos^2\alpha \left(1 - \tan\alpha \frac{3D}{2(L_C-\Delta L_C)}\right) \qquad \text{Eq. 3.4}$$

where k_{ref} is the spring constant of the reference cantilever (in Newton/meter), S_{ref} is the average measured deflection on the tip of the reference cantilever (in nanometers/Volt), S_{hard} is the average measured deflection on the base of the reference cantilever (in nanometers/Volt), L_{ref} is the length of the reference cantilever (in meters), ΔL is the offset distance of the modified tip from the end of the reference cantilever (in meters), α is the angle of the uncalibrated cantilever to the surface (in degrees), D is the height of the cantilever tip (which, in the case of a spherical tip, is the radius of the microbead; in meters); L_C is the length of the uncalibrated cantilever (in meters), and ΔL_C is the offset distance of the attached microbead from the end of the uncalibrated cantilever (in meters) (Edwards *et al.* 2008).

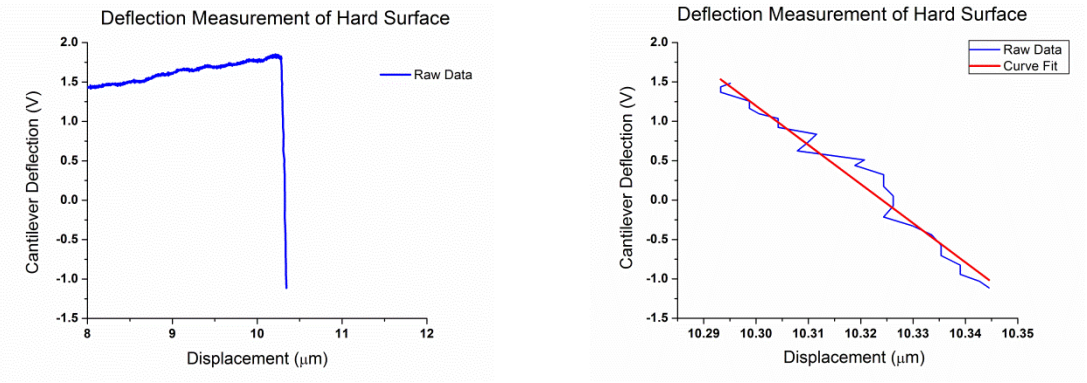

Figure 3.5: *Left*, Picture of deflection measurement on a rigid surface, the silicon base of reference cantilever. *Right*, Picture of the slope curve fit of the deflection measurement to calculate, S_{hard}.

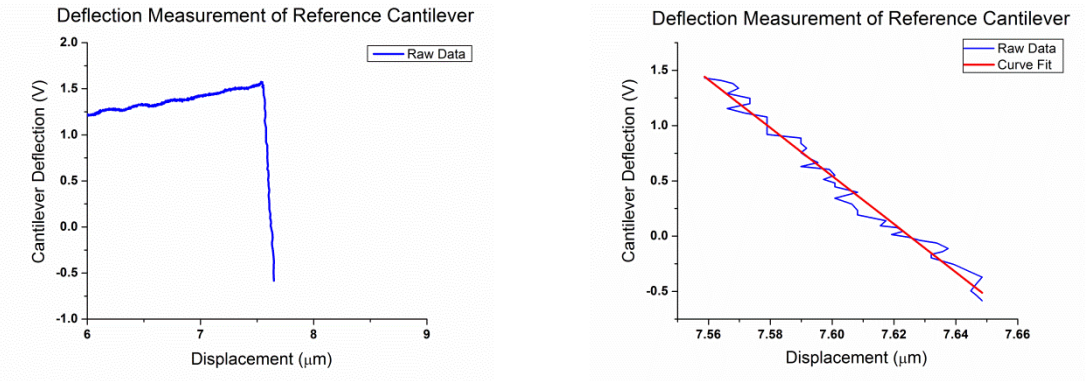

Figure 3.6: *Left*, Picture of deflection measurement on the reference cantilever. *Right*, Picture of the slope curve fit of the deflection measurement to calculate, $S_{ref.}$

$\left(\frac{L_{ref}}{L_{ref}-\Delta L}\right)^3$ is the correction factor that takes into account the contact position of the uncalibrated cantilever along the length of the reference cantilever during its deflection measurement on the reference cantilever (Ohler , Sader *et al.* 1995, Slattery *et al.* 2013). This is necessary as the reference cantilever becomes stiffer along its beam as one approaches its base. The $cos^2\alpha$ term takes into account the tilt of the uncalibrated cantilever to the reference cantilever due to the custom cantilever holder; therefore, α is set to 15°. Lastly, the $\left(1 - \tan\alpha\frac{3D}{2(L_C-\Delta L_C)}\right)$ terms takes into account the torque produced

by the spherical tip during the deflection measurement (Edwards *et al.* 2008, Slattery *et al.* 2013). Due to the difficulty of determining the precise attachment point of the microbead onto the tipless cantilever, precaution was taken to ensure that microbead is as close to the end of the tipless cantilever as possible. Therefore, ΔL_C can be assumed to be 0. Since the end of the cantilever of the modified tip cannot be distinguished on the images, the length of the modified tip, L_C, is retrieved from the specification sheet that accompanies the tipless cantilevers when they are purchased.

The dimensional parameters of the reference and uncalibrated modified cantilever (L_{ref} , ΔL, and D) are calculated by first taking pictures of the reference cantilever, the modified uncalibrated cantilever, and the uncalibrated cantilever in contact with the reference cantilever during deflection measurements (Figures 3.7 and 3.8). This is performed using the AFM's inverted imaging system consisting of a monochrome firewire camera (640x480 pixels, 5.6x5.6mm pixel size, DMK21AF04, The Imaging Source, Charlotte, NC) and a 10x microscope objective (NT36-132, Edmund Optics, Barrington, NJ). Afterward, the pictures are analyzed using the technical image measurement analysis tools of Canvas (ACD Systems of America, Inc., Seattle, WA) and are then used to derive the parameters (Figure 3.7).

The main limitations of the reference cantilever method that influence its ability to accurately determine the spring constant of an uncalibrated cantilever include the need for an accurately calibrated reference cantilever and the difficulty in determining the precise contact point of the uncalibrated cantilever on the reference cantilever beam during deflection measurement (Ohler , Gates and Reitsma 2007, Slattery *et al.* 2013). With regards to the first issue, a calibrated reference cantilever manufactured with precise

dimensions and material properties to enable an accurate spring constant determination is needed. Such cantilevers have recently become commercially available; the reference cantilevers used to calibrate the modified cantilevers were obtained from Bruker AFM Probes (Model: CLFC-NOBO; Bruker AFM Probes, Camarillo, CA). This probe contains three cantilevers of distinct spring constants: 0.157, 1.3, and 10.4N/m. The criteria of selecting the correct reference cantilever for calibrating the modified cantilevers rests upon the notion that the spring constant of the uncalibrated modified cantilever, k, should be within the range: $0.3\ k_{ref} < k < 3k_{ref}$ (Ohler , Gibson *et al.* 1997); this ensures that one cantilever does not dominate the deflection measurements (Ohler). With the fact that the nominal spring constants of the tipless cantilevers used for glass-microbead modification are 2 and 4.5N/m coupled with the consideration that the modification produces further stiffening of the tipless cantilevers, the 10.4 N/m reference cantilever is chosen for calibrating the modified cantilevers since utilizing it yields a detectable spring constant range that modified cantilevers are believed to lie within ($3.12\ N/m < k < 31.2\ N/m$). The difficulty in determining the exact contact point of the modified cantilever on the reference cantilever can contribute to a large uncertainty error because the spring constant of a beam-shaped cantilever is inversely proportional to the cube of its length (Slattery *et al.* 2013); therefore, measures are taken to try to indent as close to the end of the reference cantilever as possible. The centerline of the spherically-modified tip is first adjacently aligned to the edge of the reference cantilever; at this setup, a picture is taken with the AFM's imaging system (Figure 3.8). After, the reference cantilever is then shifted directly under the modified cantilever (Figure 3.8); a picture is then taken, before deflection measurements commence, to enable image analysis using Canvas (ACD

Systems of America, Inc., Seattle, WA) to calculate the length offset, Δt. The distance between the centerline of the spherical indenter and the end of the reference cantilever is measured to determine the length offset, ΔL; in the case of Figure 3.8, ΔL, is 0.

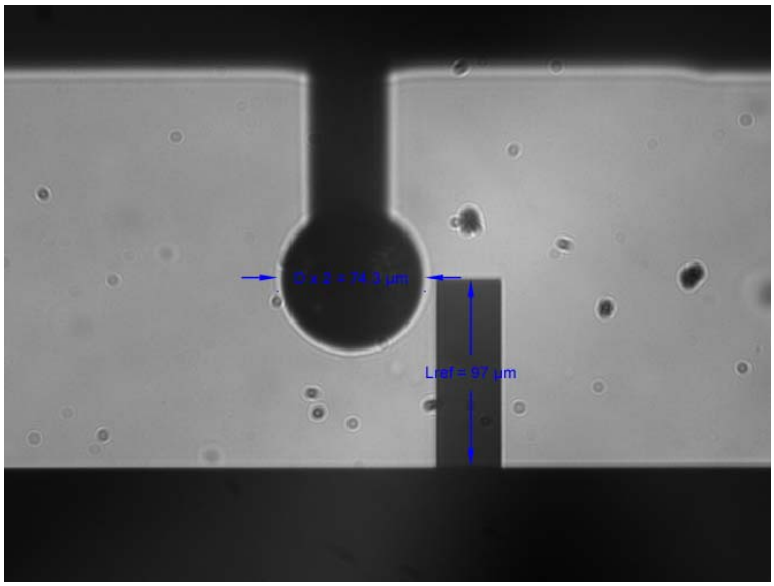

Figure 3.7: Picture of the Canvas measurement analysis to derive the length of the reference cantilever, L_{ref}, and the radius of the glass microbead, D.

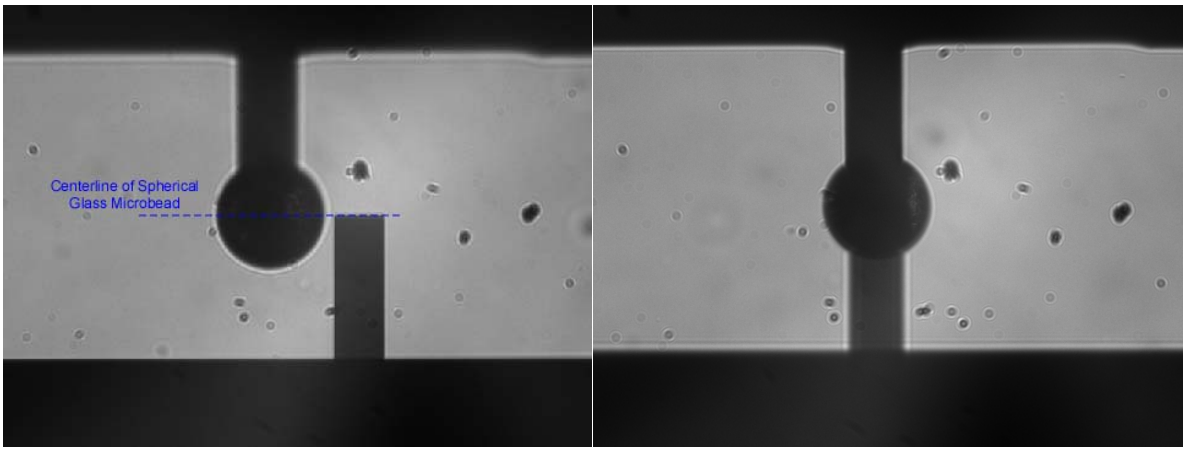

Figure 3.8: Pictures of the Modified Tip Calibration using the Reference Cantilever Method. *Left*: The centerline of the uncalibrated tip is aligned with the end of the reference cantilever. *Right*: Reference cantilever shifted directly under uncalibrated tip for deflection measurement.

3.4 Corneal Hydration

3.4.1 Rationale

For *ex vivo* corneal characterization studies, a true reflection of the *in situ* biomechanical response is heavily influenced by the hydration of the post-mortem cornea (Borja *et al.* 2004). For this reason, researchers use various media to maintain corneal hydration during mechanical testing; such media include saline solutions like PBS or HBSS (Jayasuriya *et al.* 2003, Elsheikh *et al.* 2008, Last *et al.* 2009, Last *et al.* 2012, Thomasy *et al.* 2014), Dextran solutions (Terry *et al.* 1994, Hamaoui *et al.* 2001, Borja *et al.* 2004, Lombardo *et al.* 2012, Dias *et al.* 2013, Dias and Ziebarth 2013), oils (Nash *et al.* 1982, Winkler *et al.* 2011), as well as commercial ophthalmic solutions (Elsheikh *et al.* 2007, Elsheikh *et al.* 2010). Although numerous studies have been conducted to investigate the effect of different media on corneal thickness and swelling changes over time (Swinger and Kornmehl 1985, Duffey *et al.* 1989, Terry *et al.* 1994, Jablonski-Stiemke and Edelhauser 1998, Bourne *et al.* 2001, Hamaoui *et al.* 2001, Borja *et al.* 2004), only a few studies looking into the impact of corneal hydration solutions on corneal biomechanical response have been published (Kling and Marcos 2013, Hatami-Marbini and Rahimi 2014). The purpose of these experiments was to investigate the stability of corneal mechanical properties in different hydration media. The impact of the corneal limbus on biomechanical measurements was also tested by using corneal samples with and without the limbus present (Dias and Ziebarth, 2014).

3.4.2 Materials and Methods

Experiments were conducted on 40 porcine eyes (10 eyes for each hydration medium; <3 days postmortem). The eyes were retrieved from an abattoir, placed in a bag filled with saline, and shipped to the laboratory overnight. Upon arrival in the laboratory, the corneal epithelium was removed using a cotton-tipped applicator. The porcine cornea was then excised with a generous scleral rim and placed in 20% Dextran, anterior stroma down, to restore corneal thickness to physiological levels(Swinger and Kornmehl 1985, Duffey *et al.* 1989, Borja *et al.* 2004). The intact corneas remained in 20% Dextran for 24 hours at room temperature. Pachymetry measurements were taken after 24 hours to ensure the equilibrium and restoration of the corneal thickness to physiological levels (Faber *et al.* 2008).

With the physiological thickness restored, one group of porcine corneas (5 corneas each for each hydration medium) was further excised within the limbus (all sclera removed), and the other group (5 corneas each for hydration medium) was left with the intact scleral rim around the cornea. The porcine cornea was then mounted onto the custom corneal holder and positioned so that the central region of the corneal sample was oriented directly under the AFM cantilever. The corneal holder was then filled with a hydration medium, either PBS (D1283, Sigma Aldrich, St. Louis, MO), HBSS (04-315Q, Lonza, Walkersville, MD), 15% Dextran (15 grams of dextran in 100mL of PBS; D8821, avg. molecular weight: 64,000-76,000 g/mol, Sigma Aldrich, St. Louis, MO), or Optisol (Optisol-GS, 50006-OPT, Bausch and Lomb, Rochester, NY), prior to corneal elasticity testing. While maintained in each medium, corneal elasticity measurements were

performed for 2 hours; measurements were conducted at 5-minute intervals for the first 30 minutes and then at 15-minute intervals for the remaining 90 minutes.

Elasticity characterization testing was conducted using a custom-built atomic force microscopy (AFM) system. Tipless AFM cantilevers (nominal spring constant: 4.5 N/m, NSC12 series, Mikromasch, San Jose, CA) were modified with glass microspheres (59-74μm diameter, 15926-100, Polysciences Inc) and calibrated with a reference force calibration cantilever (nominal spring constant: 10-30 N/m, CLFC-NOBO, Bruker, Camarillo, CA) to measure its spring constant. Regulated by a piezoelectric mechanism (60μm maximal expansion, P-841.40, Physik Instrumente, Germany), the spherical-tipped cantilevers were lowered onto the corneal samples at an approach speed of 15μm/s and then retracted at that same speed, once the maximal indentation force of 1000mV (<20nN) was applied. Recordings of the cantilever's deflection from the photodiode's voltage output and the cantilever's indentation from the piezoelectric displacement were then used to derive the sample's force-indentation curves (after the cantilever deflection on a hard surface is factored out and the measured spring constant of the cantilever is integrated). A custom curve-fitting MATLAB program is used to analyze to the force-indentation curves with the Hertz model for spherical indenters (Hertz 1881):

$$F = \frac{4E\sqrt{R}}{3\left(1-\nu^2\right)} D^{3/2} \qquad \text{Eq. 3.1}$$

where F is the measured force (in Newtons), E is Young's modulus (in Pascals), ν is Poisson's ratio (ν=0.49 for the cornea (Fernandez *et al.* 2005, Liu and Roberts 2005, Cartwright *et al.* 2011)), R is the radius of the spherical indenter (in meters), and D is the measured indentation (in meters). Experiments were performed at room temperature.

Corneal thickness measurements were taken with an ultrasonic pachymeter (DGH 55 Pachmate, DGH Technology Inc., Exton, PA) before and after elasticity testing.

3.4.3 Results

The average central corneal thickness for all the eyes at the start of the experiments was 562 ± 72μm (range: 436-684μm). The percentage change of the corneal thickness (change in thickness relative to initial thickness) was calculated for each sample. For the intact limbus, the percent change in thickness was: -14.0 ± 4.5% for 15% Dextran, 75.7 ± 23.3% for BSS, 81.6 ± 15.8% for PBS, and 50.4 ± 6.5% for Optisol (Figure 1). For the group where corneas were excised within the limbus, the percentage change in thickness was: -19.8 ± 21.3% for 15% Dextran, 55.8 ± 22.6% for BSS, 46.3 ± 16.3% for PBS, and 39.9 ± 14.6% for Optisol (Figure 3.9).

The percentage change of the effective Young's modulus (change in Young's modulus relative to initial Young's modulus) was calculated for each corneal sample. For the corneas excised with the limbus left intact, the average corneal elasticity percentage change was: 40.1 ± 32.2% for 15% Dextran, 115.1 ± 109.3% for BSS, 212.4 ± 159.3% for PBS, and 62.4 ± 44.1% for Optisol (Figure 3.10). While for the corneas excised within the limbus perimeter, the average corneal elasticity percentage change was: 27.1 ± 16.5% for 15% Dextran, 103.4 ± 39.0% for BSS, 83.1 ± 78.1% for PBS, and 55.6 ± 18.9% for Optisol (Figure 2). The Young's modulus profile over time for the 15% Dextran fluctuated around a median line for both corneal sample groups with and without the limbus present. Meanwhile, the BSS, PBS, and Optisol hydration solutions exhibited

a linearly increasing Young's modulus profile over time for both corneal samples with and without the limbus.

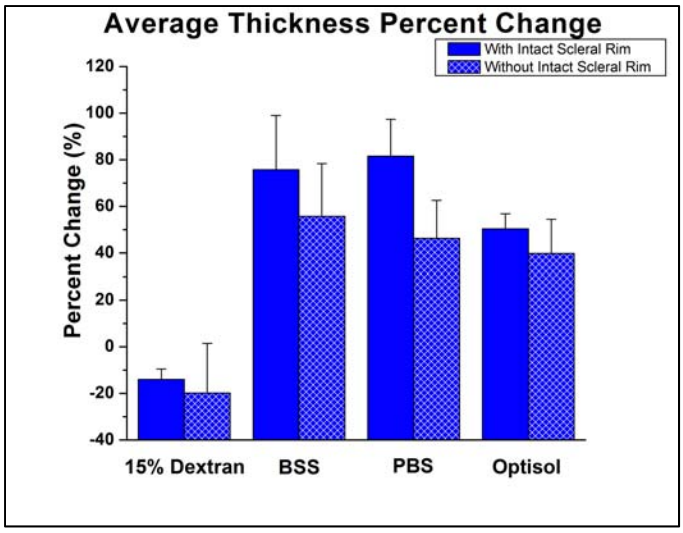

Figure 3.9: Bar Graph of the Average Corneal Thickness Percentage Change. A bar graph comparing the thickness percentage changes after 120 minutes in different hydration media. Samples with the limbus had a greater change in thickness than samples without the limbus.

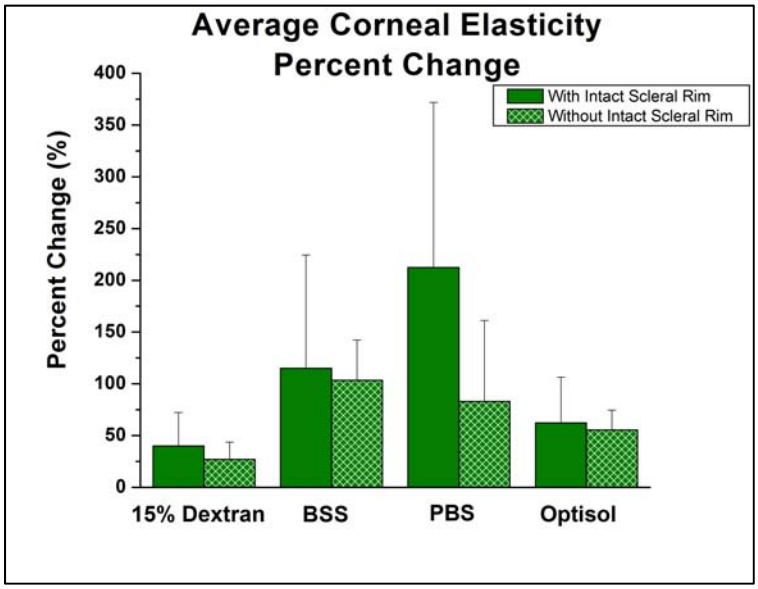

Figure 3.10: Bar Graph of the Average Corneal Elasticity Percentage Change. A bar graph comparing the corneal Young's modulus percentage changes after 120 minutes in different hydration media. Samples with the limbus had a greater change in Young's modulus than samples without the limbus.

3.4.4 Discussion

Published values of ex-vivo corneal mechanical properties vary greatly. Factors contributing to such variation include differences in characterization techniques (which reveal the anisotropic nature of the cornea), post-mortem time, age (Malik *et al.* 1992, Daxer *et al.* 1998, Elsheikh *et al.* 2007, Kotecha 2007, Randleman *et al.* 2008, Cartwright *et al.* 2011, Ruberti *et al.* 2011), and sample preparation. However, in this study, the factor of sample preparation was investigated. Corneal sample preparation, which encompasses manipulation required to prepare the sample for biomechanical testing, varies depending on the biomechanical characterization method used. For example, tensile stretching requires the cornea to be excised into thin strips, while bulge testing and AFM allow measurements to be performed on an intact cornea. With the existence of many variables attributing to the high variation of published ex-vivo corneal mechanical property values, the need for experimental standardization arises. For this reason, this study was undertaken to further our understanding of the influence of cornea hydration on mechanical property measurements *ex vivo*. The cases of keeping the scleral rim intact with cornea (which is used for AFM, inflation testing, shear testing, and acoustic radiation force elastic microscopy), by excising the cornea with a scleral rim, and having the scleral rim removed from the cornea (which is common for tensile stretching) were also investigated to determine how the presence of the corneal scleral rim affected these biomechanical measurements.

Post-mortem corneas, whether human corneas from the eye bank or animal globes like porcine eyes from an abattoir, arrive in an edematous state with thicknesses above their respective physiological range. Performing mechanical characterization testing on

such edematous corneas would yield biomechanical results influenced by high water content, thus not reflecting an accurate measure of in-situ corneal responses. Therefore, the restoration of the corneal thickness to the normal physiological thickness range before characterization testing is imperative. Some researchers explicitly make mention of measuring the corneal thickness before characterization testing (Elsheikh *et al.* 2007, Elsheikh *et al.* 2008, Elsheikh *et al.* 2010, Lombardo *et al.* 2012, Dias *et al.* 2013, Dias and Ziebarth 2013, Sondergaard *et al.* 2013, Wernli *et al.* 2013, Mikula *et al.* 2014) but only a few take measures to address corneal thickness restoration before characterization testing (Lombardo *et al.* 2012, Dias *et al.* 2013, Dias and Ziebarth 2013, Mikula *et al.* 2014). Based on the results of this present study, measures should also be taken to address the corneal hydration (and thickness), through the use of hydration media, during measurements as they affect corneal biomechanical properties.

In this study, corneal elasticity profiles, obtained through AFM indentation testing, were mapped over the span of 2 hours in the hydration solutions of 15% dextran, PBS, BSS, and Optisol (Figure 3). In addition, corneal thickness was performed before and after mechanical testing. Mechanical testing and thickness measurements were conducted on two corneal samples groups: corneas with the scleral rim left intact and corneas excised within the scleral rim perimeter. The elasticity profiles of BSS and PBS respectively showed a steady increase in Young's modulus, while the profiles of 15% Dextran and Optisol fluctuated around a median. For both corneal samples where the scleral rim was left intact and removed, 15% Dextran was most effective in maintaining corneal thickness and yielded the least change in corneal elasticity over the two hour experimental span. Although producing the minimum change in corneal thickness out of

the hydration media, it is important to note that the 15% Dextran caused corneal dehydration. This same dehydrating effect has been observed previously by Hamaoui *et al* (2003), Duffey *et al* (1989) and Terry *et al* (1994), where they noted initial corneal thinning followed by thickness stability. Perhaps a lower concentration of Dextran would be necessary to minimize the observed corneal shrinkage. In fact, 8% Dextran was included in the Kling and Marcos (2013) study and showed a lesser dehydrating effect on the corneal thickness than that seen for the 15% Dextran concentration used in this study. Further investigation using the 8% Dextran concentration should be conducted. After 15% Dextran, Optisol followed in its effectiveness to maintain corneal hydration. Similar to this study, corneal thickening in Optisol was also observed in the study of Bourne *et al* (2001), while the study of Jablonski-Stiemke and Edelhauser (1998) revealed that the mean percent water content within the cornea increased significantly in Optisol, without the corneal epithelium present. BSS and PBS were not effective at all and resulted in extreme corneal swelling. A previous study by Hatami-Marbini and Rahimi (2014) also noted an increase in corneal thickness for PBS and BSS (4.9% increase for PBS and 4.2% increase for BSS). However, since their thickness measurements were performed after only 10 minutes in the hydration media, the percent increases were much smaller than those seen in the current study. The studies of Terry *et al* (1994) and Duffey *et al* (1989) also showed the rehydrating effect of BSS on corneal thickness as up to a 22% and 14.7% increase in corneal thickness was respectively observed when cornea samples were subjected to BSS drops on the anterior corneal surface for one hour.

The precise mechanism that enables 15% Dextran to maintain corneal hydration more effectively than the more physiological analog solutions of PBS and BSS is

currently unknown. However, it is believed some type of molecular diffusion between the corneal ultrastructure and the 15% Dextran solution may be taking place. One probable explanation for the observed phenomenon of effective corneal hydration maintenance is the fact that the molecular weight of the dextran solution is greater than the corneal molecular junction size, thereby inhibiting dextran solution diffusion into the cornea and thus minimal change in corneal thickness. Nonetheless, the observance of slight corneal dehydration with the 15% Dextran may indicate that minimal diffusion of corneal water content into the dextran solution takes place in order to reach equilibrium. Future studies investigating possible molecular mechanisms of the post-mortem cornea that play a role in corneal hydration maintenance with different hydration media should be conducted.

Young's modulus of elasticity increased for all samples, indicating an increase in stiffness. The greater the level of corneal swelling, the larger the percentage change in corneal Young's modulus. This was most apparent for the samples placed in BSS and PBS, which had the highest percentage changes in both corneal thickness and elasticity compared 15% Dextran and Optisol. Previous studies of Kling & Marcos (2013) and Hatami-Marbini & Rahimi (2014) also investigated the effect of different corneal media solutions on corneal biomechanical responses using inflating testing and uniaxial tensile testing, respectively. The Kling and Marcos (2013) study investigated the change in hysteresis of corneas (with the scleral rim intact) during different intraocular pressure levels with the corneal samples in 20% dextran, 8% dextran, 0.125% riboflavin-20% dextran, or Optisol-GS. The slope of the curves as IOP increases can be related to the corneal stiffness. Kling and Marcos found that corneas in Dextran solutions were less stiff than those in Optisol, which mirrors the results of the current study (more swollen

samples were stiffer). The Hatami-Marbini and Rahimi (2014) study performed tensile stretching experiments on corneal strips in 12% NaCl, 0.9% NaCl, PBS, ophthalmic balanced saline solution (OBSS), and mineral oil. The trend found in the Hatami-Marbini and Rahimi (2014) study showed that increasing corneal thickness yielded a decrease in corneal tangent modulus, which contradicts the trends found within this study. Such discrepancy in the qualitative results of this current study and that of Hatami-Marbini and Rahimi may stem from the difference in characterization technique. When the cornea swells due to the hydration media, the hydration solution occupies the interfibrillar space. At the high levels of corneal swelling observed in this current study, it may be possible that there is so much fluid in the corneal tissue that it causes the collagen fiber interconnectivity to be overextended. Since AFM indentation is a compressive technique and the indentations upon the cornea were performed instantaneously, a stiffening effect was observed because the tautness of the collagen fibers did not allow the hydration solution to displace easily within the collagenous network. The results of this study may imply that the elastic property of the cornea may not structurally correspond to the collagen fibers within the corneal ultrastructure only, but may also be influenced by the amount of extracellular matrix between the collagenous networks as well. Therefore, it is imperative to make sure that the corneal samples subjected to biomechanical characterization are within the physiological thickness range before testing and such thickness can be maintained during testing, to yield biomechanical responses close to physiological form.

Corneal samples excised within the scleral rim consistently yielded lower percentage changes in thickness and elasticity, independent of the hydration media used.

The observation of such phenomenon may stem from an increase in peripheral diffusion. Since the corneal sample no longer has a circumferential impermeable boundary that restricts fluid flow, hydration media is able to flow in both the axial and the transverse directions. Therefore, corneal samples without the intact scleral rim are more susceptible to both the inflow and outflow of hydration media, and the thickness changes were observed as less dramatic than those observed with the intact scleral rim present. Since samples without the intact scleral rim are consistently thinner than samples with the limbus in the same hydration media, there is a corresponding increase in Young's modulus, as described in the previous paragraph. For hydration media BSS and PBS, this degree of increase in Young's modulus is shown to be greater than of 15% Dextran and Optisol. Tissue swelling causes an overextension of the collagen fibers. When the corneal sample with the intact scleral rim was indented upon, the corneal fluid content was unable to be displaced circumferentially, resulting in a stiffening effect.

In summary, this study confirms that corneal hydration media does have an effect on measured ex-vivo corneal elasticity and thickness over time. Measures should be performed to carefully select a corneal hydration medium that effectively maintains corneal hydration during corneal biomechanical testing. For the both cases of corneal samples having the intact scleral rim and corneal samples excised within the scleral rim, 15% Dextran exhibited the most effectiveness in stabilizing corneal thickness and maintaining corneal elasticity over the span of 2 hours.

3.5 Summary

Custom techniques were developed to enable accurate corneal biomechanical characterization using atomic force microscopy. The developed techniques were designed to simulate the curvature and hydration of the cornea *in vivo* as well as to obtain a microscale biomechanical response reflecting the dynamics of the tissue's collagenous network. This was accomplished by:

- Designing a customized holder to minimize corneal sample manipulation and maintain corneal curvature.
- Developing and implementing a protocol for AFM cantilever tip modification and calibration. Tipless AFM cantilevers were modified with glass microbeads. The use of spherical indenters as the probes during AFM mechanical testing enables the investigation of corneal mechanical response on the structural scale of its collagenous networks.
- Performing an experimental study to determine the influence of corneal hydration media on the stabilization of corneal thickness and elasticity measurements during experimental testing. Results of the study showed that the corneal hydration media has an effect on measured corneal thickness and elasticity over time. 15% Dextran was found to be most effective in stabilizing corneal thickness and maintaining corneal elasticity.

CHAPTER 4

STRESS RELAXATION MEASUREMENT USING ATOMIC FORCE MICROSCOPY

4.1 Purpose

Full mechanical characterization of tissues requires the measurement of both elastic and viscoelastic properties to reveal the nature of instantaneous and time-dependent tissue responses, respectively (Fung 1993). A custom AFM system was initially developed for elastic characterization functionality in an effort to measure the Young's modulus of elasticity of tissues. However, to provide a more comprehensive profile of a tissue's mechanical response, the ability to perform viscoelastic characterization is also necessary. When applied to the cornea, viscoelasticity gives insight into both the elastic and viscous nature of the cornea during deformation. To enable viscoelastic characterization functionality, the ability to perform stress relaxation testing will be incorporated into the AFM system. The aim of this chapter is to develop AFM instrumentation that enables the stress relaxation testing of the cornea.

4.2 Hardware

Initially, two AFM systems were developed with the sole capability of measuring Young's modulus of elasticity. The design of the Atomic Force Microscopes was based on that previously developed by Noel Ziebarth, Ph.D. (Figure 4.1; (Ziebarth 2008)). To perfom elasticity testing, a cantilever is first placed onto a custom cantilever holder made out of VeroWhite resin. The holder fixates the cantilever tip at a 15^{o} angle to ensure that only the tip comes into contact with the sample and not the holder (Figure 4.2). The

cantilever, in its holder, is then placed onto the piezoelectric actuator (60µm maximal expansion, P-841.40, Physike Instrumente, Auburn, MA), which is responsible for the vertical displacement of the cantilever. Its expansion, once subjected to a voltage signal, enables the lowering of the AFM cantilever tip onto the sample.

Monitoring of the cantilever tip deflection during nanoindentation testing is achieved with the use of a laser diode and position-sensitive photodiode. The beam of a single mode, pigtailed laser diode (2.71mW, 635nm, LPS 635FC 030SP, Thorlabs, Newton, NJ) is focused onto the tip of the cantilever and is reflected onto a 2-segment position-sensitive photodiode (SPOT-2D, OSI Optoelectronics, Hawthorne, CA), which detects the change of the reflected beam's position during cantilever deflection. The position-sensitive photodiode converts the reflected light into an electrical signal. This electrical output is then sent to a custom circuitry with dual function: (1) to be a current buffer amplifier and (2) to add and subtract the signals of the photodiode's 2 segments (A and B) to determine the cantilever deflection. The circuitry output signals, A+B and A-B, are then sent to the control software (Igor Pro, Wavemetrics, Portland, OR) through a data acquisition system (ITC-18/PCI, Instrutech, Port Washington, NY).

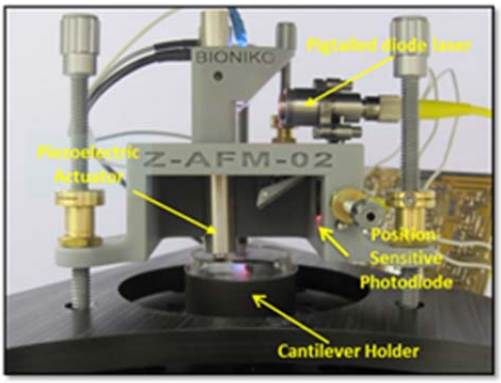

Figure 4.1: Picture of AFM System with Integral Components.

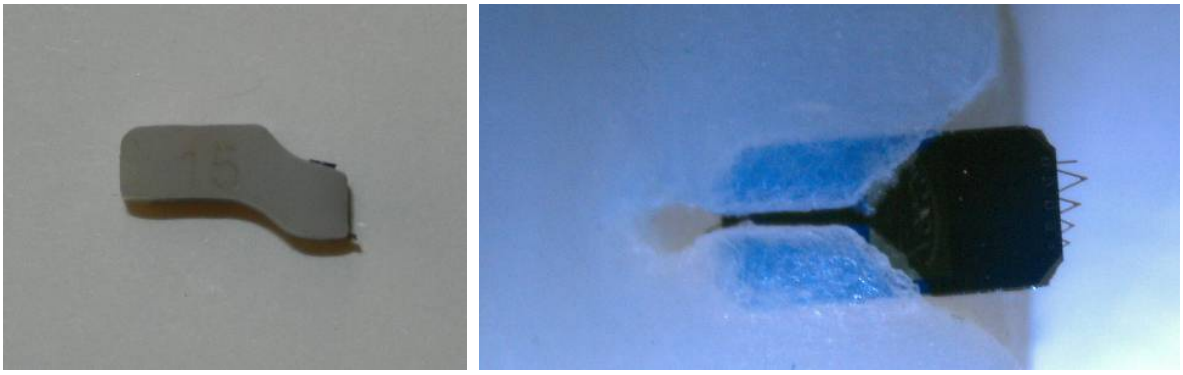

Figure 4.2: *Left,* Side View of Cantilever Holder. *Right,* Close up of Cantilever Anchored in Holder.

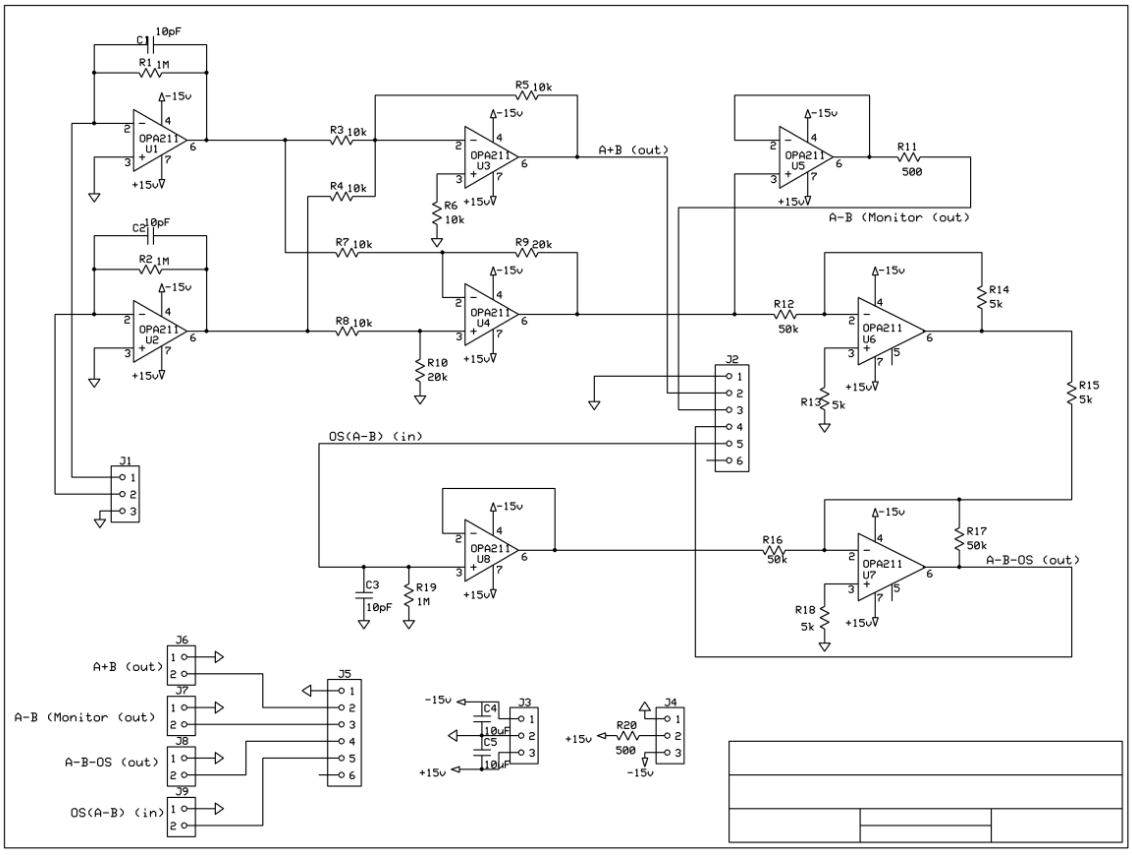

Figure 4.3: Schematic of Photodiode Circuitry

An inverted imaging system with a monochrome firewire camera (640x480 pixels, 5.6x5.6mm pixel size, DMK21AF04, The Imaging Source, Charlotte, NC) and a 10x microscope objective (NT36-132, Edmund Optics, Barrington, NJ) is located underneath the AFM system to view the cantilever and sample to ensure the structural integrity of the cantilever, allow accurate positioning of the laser beam onto the cantilever tip, and verify that no abnormalities in the sample measurement area exists.

Although the basic AFM system instrumentation is the same as that developed by Ziebarth (2008), modifications to the housing of the AFM have been made. The primary design to shield the AFM from acoustic noise, thermal vibrations, and mechanical vibrations consisted of placing the system onto a marble plate suspended by bungee cords and having the entire system inside a nonfunctioning freezer. However, the new system is now on an optical table of supreme stability and vibration isolation capability (M-RS4000-510-12, Newport, Irvine, CA). The AFM system is mounted onto a rectangular aluminum plate (12 x 16 inches) 10.5 inches above the optical table using 4 aluminum posts. For acoustic and further vibration shielding, the AFM is isolated with a vertical-sliding Faraday cage lined with soundproof foam insulation (Bioniko, Sunny Isles, FL) during experiments. In addition, the photodiode circuitry was minimized using microelectronic components to reduce the size of the AFM's main peripheral element connected to the AFM housing (Figure 4.3).

4.3 Software

4.3.1 Overview

The developed AFM systems, with elastic characterization function, operate with a custom program based in Igor Pro (WaveMetrics, Inc., Portland, OR) to acquire force-indentation profiles. The program delivers user-defined piezoelectric speed and expansion voltage signals to the piezoelectric actuator to induce the vertical movement of the cantilever tip toward the sample. It also records subsequent relative voltage changes corresponding to the reflected laser beam deflection on the photodiode (A-B signal) and the expansion/retraction voltage profile of the piezoelectric actuator during cantilever indentation onto the sample. To enable viscoelastic stress-relaxation testing using the AFM system, modification to the custom program was performed.

Stress relaxation testing encompasses subjecting a tissue of interest to constant strain (indentation) and measuring its subsequent decreasing stress (force) response as a function of time. Stress relaxation can be executed using atomic force microscopy by holding the vertical cantilever displacement constant on the tissue surface for a user-inputted time interval and recording the resultant force response (Figure 4.4). Direct implementation of such testing to the AFM system requires the use of computer software to control the data acquisition system (ITC-18/PCI, Instrutech, Port Washington, NY), which regulates the piezoelectric actuator's expansion and retraction (60μm maximal expansion, P-841.40, Physike Instrumente, Auburn, MA) for the AFM cantilever's vertical displacement control and the recording of the relative voltage changes of the position-sensitive photodiode (SPOT-2D, OSI Optoelectronics, Hawthorne, CA) to determine the resultant tissue force response. To enable AFM stress relaxation testing,

code was created and incorporated into the custom Igor Pro program to enable data storage, recording, and processing. Afterwards, the data is fitted to a viscoelastic model.

4.3.2 Data Storage

The data storage process is comprised of making and initializing data variables so that the recorded stress relaxation measurements during the viscoelastic testing can be stored to them. The creation of data storage encompassed making a contact output wave (where a wave is the Igor Pro software terminology synonymous to a data array) and input wave. The contact output wave (or outwave, for short) functions as the stimulus sent to the data acquisition's First-In, First Out (FIFO) memory and directed to the piezoelectric actuator for the vertical displacement control of the AFM cantilever. The movement of the piezoelectric actuator, and therefore cantilever tip vertical movement toward the sample, is dictated by the linear profile of the outwave. Piezoelectric expansion, which signifies the vertical downward movement of the cantilever toward the sample, corresponds to an increasing linear slope profile of the outwave; piezoelectric actuator retraction, which signifies the vertical upward movement of the cantilever back to its original position, corresponds to a negative linear slope line back to zero for the contact outwave. For elasticity testing, two contact outwaves are sent to the piezoelectric actuator for the cantilever tip approach toward the sample and retract back to its original position; their profile is that of a positive linear slope and negative linear slope, respectively (Figure 4.5). To implement stress relaxation, a contact outwave is created with the profile of a horizontal line of zero slope and implemented directly after the approach contact outwave stimulus is sent to the piezoelectric actuator (Figure 4.6). This

contact outwave signifies holding the cantilever tip constant onto the sample's surface for a user-defined hold time, once the cantilever tip has indented sample at the user-defined piezoelectric speed and expansion voltage signals. The length of the contact outwave is set to 12,000 data points, as suggested by the data acquisition system's manufacturer to ensure optimal performance in continuous acquisition applications; this size gives the computer enough buffer to keep acquiring data without running out of memory to save the information. It is also important to note that this size is not dependent on the user-defined hold time and therefore does not regulate the recording setting of the data acquisition system. Therefore, if the size of the contact outwave is smaller than of the contact input wave, the last voltage value of the contact outwave is repeated until the contents of the contact input wave has been filled during acquisition. The voltage value of the contact outwave, which is equivalent to the last voltage of the position slope line of the approach contact outwave, is determined by the user-defined expansion voltage.

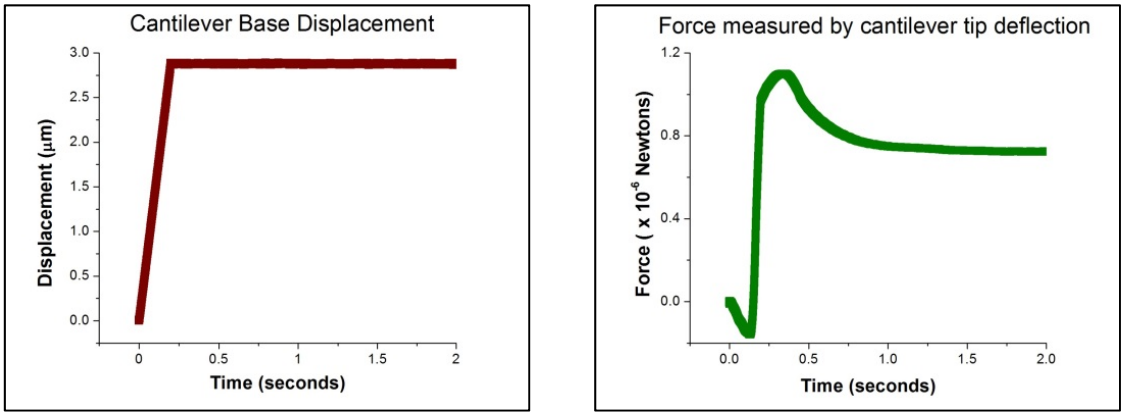

Figure 4.4: AFM Stress-Relaxation Testing. *Left,* Graph of Vertical Cantilever Displacement Held Constant on Tissue Surface During Stress-Relaxation tesing. *Right,* Graph of Resultant Force Response of Tissue due to Constant Strain Application from AFM Cantilever.

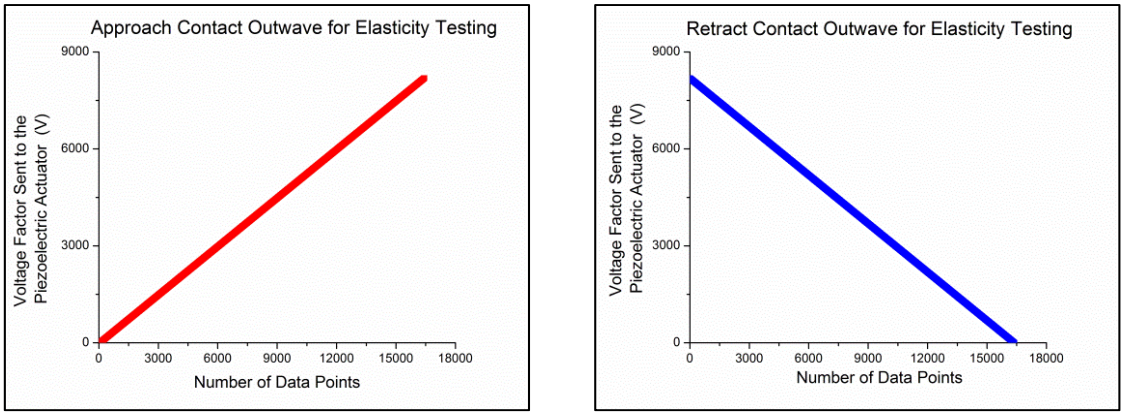

Figure 4.5: Contact Output Waves (or Outwaves) used in computer software to conduct elasticity testing. *Left*, Graph of Approach Contact Outwave for Elasticity Testing. *Right*, Retract Contact Outwave for Elasticity Testing.

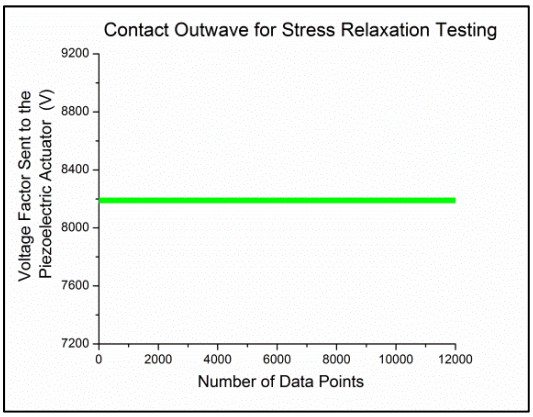

Figure 4.6: Contact Output Wave (or Outwave) used in computer software to conduct stress relaxation testing.

During stress relaxation testing, the resultant response of the cantilever tip indentation during the hold time (recorded from the relative voltage changes detected from the photodiode) and the voltage signals of the piezoelectric actuator's movement are saved in the contact input wave (or inwave, for short). The length of the contact inwave for stress relaxation is determined by the user-defined duration that the cantilever tip is held constant on the sample's surface, the sampling rate, and the number of channels of

the data acquisition system that need to the recorded. Therefore, the length of the contact inwave is calculated by:

$$Length\ of\ Contact\ Inwave = (Hold\ Time/Sampling\ Interval)\ x\ Number\ of\ Channels\ Recorded \quad \text{Eq. 4.1}$$

The constant hold duration of the stress relaxation testing is determined by:

$$Hold\ Time = dwellTime\ x\ (1/60)\ \text{[seconds]} \quad \text{Eq. 4.2}$$

where *dwellTime* is the user-inputted time factor that must be multiplied by 1/60 to produce the stress relaxation hold time in seconds. For example, to obtain a hold time of 60 seconds for the stress relaxation testing, the *dwellTime* parameter is then set to 360. The sampling rate for data acquisition was chosen to be 1 millisecond because it is the smallest sampling interval that would allow the maximum amount of data points to be saved for a hold time range of 0 to 8 minutes without running out of the data acquisition memory. Since the maximum sample memory capacity that the data acquisition system can hold is 1,024,000 data points, using the sampling rate of 1 millisecond ensures that 960,000 data points are collected so that complete profiles of the resultant force response derived from the photodiode signal and the cantilever displacement derived from the piezoelectric actuator sensor are captured for a hold time range of up to 8 minutes. The remainder of data acquisition memory is reserved for the contact outwave and the computer buffer. Nonetheless, the sampling interval setting can be changed by the user. Since both the movement of the piezoelectric actuator and the subsequent voltage changes of the photodiode are connected to a channel in the data acquisition system, these two channels need to be recorded. After the creation of the stress relaxation contact

outwave and inwave, measures to implement the recording of the piezoelectric actutator's movement (representative of the cantilever tip movement) and the photodiode's voltage signals (representative of the force response) are then performed.

4.3.3 Data Recording

The data acquisition system can be controlled with Igor Pro by utilizing an Igor external operation, known as ITC18XOP (Instrutech, Port Washington, NY). This entity permits the control of the data acquisition system through customized command functions that can be written in the Igor Pro command. To enable stress relaxation testing, four ITC18-XOP commands are responsible for the recording of the cantilever tip hold and resultant sample force response. The four command line operations are *ITC18Stim*, *ITC18StartAcq*, *ITC18Samp*, and *ITC18StopAcq*.

The *ITC18Stim* command is responsible for sending the contents of the stress relaxation contact outwave into the output FIFO of the data acquisition system. The custom code was already written with an established sequential acquisition memory pattern to:

- For one sampling interval, or clock pulse: shift data from the output FIFO to the piezoelectric actuator and retrieve data coming from the photodiode to the input FIFO
- For the next sampling interval, or clock pulse: shift data from the output FIFO to the piezoelectric actuator and retrieve data from the piezoelectric actuator sensor to the input FIFO

- For the next sampling interval, or clock pulse: shift data from the output FIFO to the piezoelectric actuator and retrieve data coming from the photodiode to the input FIFO again

Therefore, the *ITC18Stim* command sends the stress relaxation outwave to the piezoelectric actuator.

The initialization of data acquisition can then commence with the command line operation *ITC18StartAcq*. With the use of this command, settings for the sampling period, flags for controlling data acquisition, and the clock source can be established. The command line *ITC18StartAcq 400, 2, 0* was placed in the custom code for stress relaxation testing to signify that sample acquisition takes place every 500 microsecond interval as soon as the command is executed and that all outputs of the data acquisition channels can be accessible for recording (refer to Appendix 1). It was previously noted that the sampling period of the stress relaxation testing was set to 1ms; this still remains in effect because the 500 microsecond interval assigned in the *ITC18StartAcq* command takes into account the 2 channels that need to be recorded and that only one channel can be recorded per clock tick. Therefore, the photodiode output is first retrieved at time zero, the piezoelectric actuator sensor output is retrieved at the first 500μs clock pulse, then the photodiode output is retrieved again at the second 500μs clock pulse, and so on. This alternating sequence continues until stopped; nonetheless, the sampling interval for reach channel remains equivalent to 1ms.

The recording of the data into the stress relaxation contact inwave takes place with the command line operation *ITC18Samp*. This operation transfers the data retrieved from the input FIFO into the stress relaxation contact inwave. Since the two channels of

the photodiode and piezoelectric sensor were alternately recorded at 500μs intervals, both data signals are interleaved within the inwave. Once the stress relaxation inwave is complete, the command line *ITC18StopAcq* is executed to stop the sampling clock and terminate data acquisition.

4.3.4 Data Processing

Since the content of the stress relaxation contact inwave consists of the interleaved data signals from the photodiode and piezoelectric actuator sensor, measures to separate and graph them need to be performed within the data processing phase. The pre-existing custom code encompassed user-created functions to achieve such measures. The names of the functions are *ForceWBuild*, *ForceWDisplay*, and *ForceWSave.*

The *ForceWBuild* function separates the stress relaxation contact inwave into the respective photodiode (corresponding to force) and piezoelectric actuator sensor (corresponding to cantilever displacement) data signals. These data signals are converted into voltages and saved as two new waves, *FWaveSRAB* and *FWaveSRAD7,* respectively. Afterward, dimension scaling of the waves is performed, where the time scale of the waves is established from time zero to the user-defined hold time of the stress relaxation testing and the unit of the data is labelled in voltage. In addition, a new wave, *FWaveAD7Combined*, is initialized and created to obtain a complete profile of the piezoelectric actuator movement, depicting its initial position, its movement toward the sample for indentation, and its constant hold upon the sample during stress relaxation testing. This wave is used to verify that the piezoelectric actuator functioned properly during the viscoelastic testing.

The *ForceWDisplay* function displays the profiles of the recorded piezoelectric sensor and voltage changes of the photodiode during the stress relaxation testing as graphs within the Igor Pro control software comsole. Using the scaling performed by the *ForceWBuild* function, the x-axis of the graphs is labelled in seconds and the y-axis is labelled in Volts. The *ForceWSave* function then saves and exports each wave as a text file for further viscoelastic model fitting to extract stress relaxation parameters.

4.3.5 Stress Relaxation Model Fitting

The stress relaxation parameters are determined by performing mechanical model fitting to the sample's force response, which is derived from the relative voltage changes of the position-sensitive photodiode. The photodiode voltage data, therefore, must be converted into force (in Newtons) versus time (in seconds). A MATLAB program was previously written to determine the Young's modulus of elasticity; this program was slightly modified to perform the data conversion and the viscoelastic curvefitting.

The voltage detected by the position-sensitve photodiode ($V_{photodiode}$) is converted to force using the equation:

$$F = k\,CV_{photodiode} \qquad \text{Eq. 4.3}$$

where F[N] is the force of indentation, k[N/m] is the cantilever's spring constant (see Eq. 3.4), and C[V/m] is the slope of the photodiode voltage versus cantilever displacement. The slope, C, is experimentally obtained by placing the cantilever in contact of the bottom of the Petri dish, filled with BSS, with an indentation voltage of 1000mV. The total stress relaxation hold time, T, is calculated by:

$$T = Sampling\ Interval * L_{photodiode} \quad \text{Eq. 4.3}$$

where the sampling interval is set to 0.001 seconds and $L_{photodiode}$ is number of data points recorded from the photodiode. A time array is then created from 0 to the total hold time (in seconds) with increments of 0.001 seconds. Force versus time is plotted and fit with a viscoelastic analytical function; this function corresponds to the viscoelastic stress relaxation model that derives the stress relaxation parameters. In addition, the sample indentation is determined by converting the voltage of the piezoelectric actuator (V_{piezo}) into cantilever indentation using the equation:

$$I = abs\left(\frac{60.014\ x\ 10^{-6}}{10.24}\ V_{piezo}\ - CV_{photodiode}\right) \quad \text{Eq. 4.3}$$

where I [m] is the indentation, 60.014 x 10^{-6}/10.24 is the scaling factor defining that a piezoelectric actuator voltage of 10.24V corresponds to 60.014µm displacement, V_{piezo} [V] is the voltage of the piezoelectric actuator, C [V/m] is the slope of the voltage versus displacement, and $V_{photodiode}$ [V] is the voltage detected at the photodiode. The cantilever indentation is plotted as a function of time to ensure that the cantilever indentation on the sample was constant during stress relaxation testing and to calculate the indentation depth at which the testing took place for viscoelastic model fitting. Complete details of the experimental model fitting analysis are performed in the MATLAB program (Appendices 2 and 3).

4.4 Validation of Stress Relaxation Measurements

The developed stress relaxation capability of the custom-built AFM system will be used to determine the viscoelastic properties of the cornea. Therefore, to ensure the

accurate and effective measurement of the corneal force relaxation response during stress relaxation testing, a validation of the system must be performed. To perform such validation, stress relaxation testing was performed on a non-viscoelastic material. By using a material with no viscoelastic behavior, the expected outcome of this validation is the observance of a constant force response over the duration of the stress relaxation testing.

The material chosen for this validation was the same Petri dish used to calibrate the AFM system before elasticity characterization testing. The Petri dish, which is made up of high-quality polystyrene, exhibits high rigidity and no viscoelastic behavior. Using a modified spherical cantilever tip, stress relaxation testing was performed on the bottom of the Petri dish filled with BSS. As expected, the resultant force response of the Petri dish during stress relaxation testing was constant with the presence of some linear drift, due to the piezoelectric actuator (Figure 4.7). The profile of this resultant force response is significantly different from that of the cornea, which exhibits more of an exponential profile that reaches an asymptote and levels off (Figure 4.8).

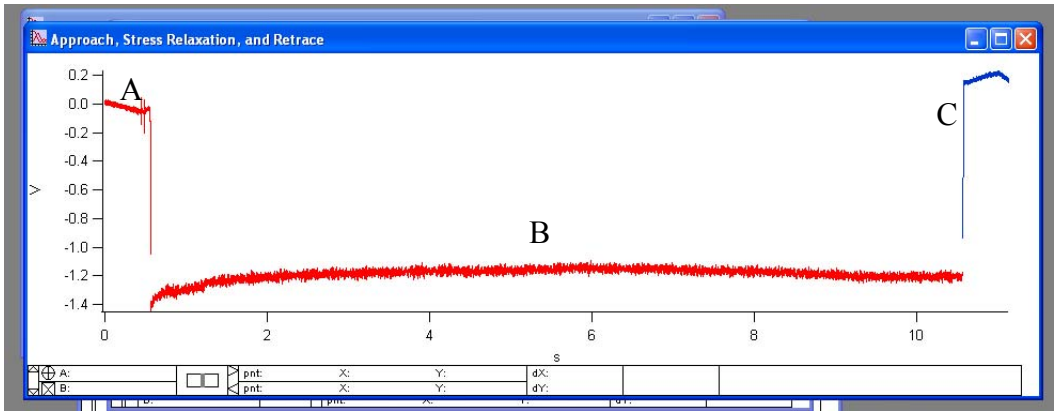

Figure 4.7: Raw data force response of the Petri dish recorded from the position-sensitive photodiode during the cantilever's approach toward the Petri dish (A), stress relaxation testing from the Petri dish (B), and cantilever's retraction away from the Petri dish (C).

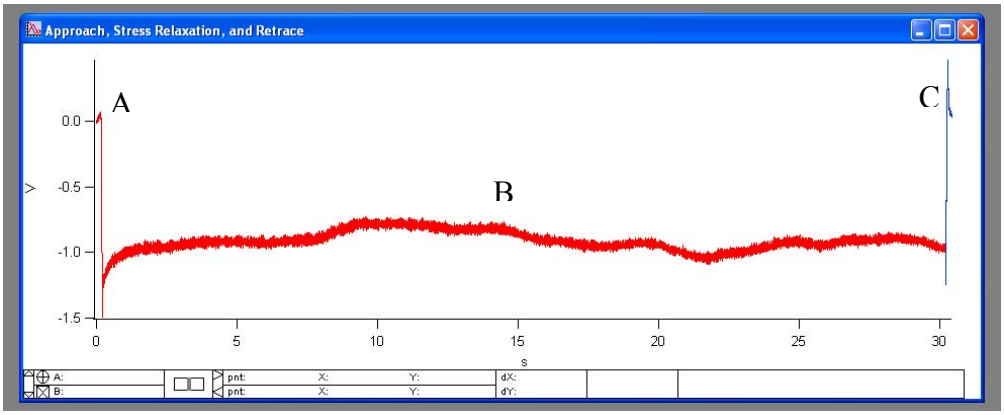

Figure 4.8: Raw data force response of the cornea recorded from the position-sensitive photodiode during the cantilever's approach toward the cornea (A), stress relaxation testing (B), and cantilever's retract away from the cornea (C).

4.5 Summary

The capability of the custom AFM system was extended to enable the full mechanical characterization of the cornea. Although already having the capability to characterize the elastic property of the cornea, AFM instrumentation was developed to enable corneal viscoelastic characterization. This was accomplished by:

- Developing software to perform stress relaxation testing. The custom system is able to implement constant indentation depth onto the surface of the sample of interest and record the resultant force response. Developed MATLAB programs can then be used to derive stress relaxation parameters from the recorded force response.
- Validating the viscoelastic capability of the system by performing stress relaxation on a material exhibiting no viscoelastic behavior. Results of the validation showed the significant difference in the recorded force response between materials without viscoelastic behavior (such as the Petri dish) and with viscoelastic behavior (as in the case of the cornea). Such outcomes signified the

system's ability to detect and record corneal viscoelastic responses during stress relaxation testing.

CHAPTER 5

BIOMECHANICAL MODELS

5.1 Purpose

Within literature, various indentation-based contact mechanical models have been developed for both non-biological (thin metal films) and biological (such as the articular cartilage) samples. The goal of Chapter 5 is to conduct a thorough, comprehensive study of pre-existing contact mechanical models (developed for both non-biological and biological applications) and apply them to the measured corneal mechanical responses obtained from the instrumentation and techniques described in the previous chapters. Determination of respective elastic, viscoelastic, and poroelastic models that best represent the mechanical nature of the corneal tissue is then conducted. This chapter includes an investigation of the elasticity, viscoelasticity, and poroelasticity models as well as the software development to enable model fitting and comparative analysis.

5.2 Elasticity Models

5.2.1 Overview

The utilization of nanoindentation to accurately measure the mechanical properties of biological samples is heavily dependent upon the geometry of the indenter used. Contact mechanical models enable the derivation of mechanical properties, such as Young's modulus of elasticity, by establishing a relationship between the force applied to a body and the resultant deformation that occurs based on the nature of the sample and indenter as well as the indenter geometry. The common indenter geometries used in

nanoindentation testing are spherical, conical, and pyramidal. The contact mechanical models for these three geometries will be described below.

5.2.2 Spherical Indenter: Hertz Model

The most commonly used contact mechanical model for spherical indenters is the Hertz model. The Hertz model describes the contact between two ellipsoidal bodies. The indentation of a flat elastic surface, of an infinite radius of curvature, by a rigid spherical body is mathematically expressed (Lin and Horkay 2008). The Hertz model provides a relationship between the Young's modulus of elasticity of the sample undergoing indentation testing, the force exerted onto a sample, and the consequent sample indentation. The equation is as follows (Hertz 1881):

$$F = \frac{4\,E\,R^{1/2}}{3\,(1\,-\,\nu^2)}\,D^{3/2} \qquad \text{Eq. 5.1}$$

where F [N] is the applied force, E [N/m^2 or Pascal] is the Young's modulus of elasticity of the sample of interest, R [m] is the radius of the indenter, ν [dimensionless] is the Poisson's ratio, and D [m] is the indentation. The contact radius, a [m], which is defined as the radius of the spherical indenter that is entirely in contact with the sample, can be calculated as:

$$a = \sqrt{R\,D} \qquad \text{Eq. 5.2}$$

The Hertz model is valid under the following assumptions (Johnson 1985, Cappella and Dietler 1999, Dimitriadis *et al.* 2002, Seherr-Thomas *et al.* 2006, Lin and Horkay 2008, Last *et al.* 2009):

- The sample is isotropic, homogenous, and linearly elastic
- The sample is infinitely thick

- The sample and indenter are both frictionless, therefore adhesion is neglected
- The contact radius, a, is much smaller than the radius of the indenter, R. Thus, small sample strains (< 10%) occur during contact with the indenter

For corneal elastic responses obtained from the developed AFM system, this model is used to determine the Young's modulus of elasticity. Since indentations less than 10% of the total corneal thickness (which is considered small deformation) are applied during mechanical elastic testing, the resultant corneal responses lie within the linear elastic regime (Fischer-Cripps, 2002). Therefore, the Hertz model lies in good agreement with the experimental corneal elastic response ($0.97 < R^2 < 1$).

5.2.3 Conical Indenter: Sneddon Model

The Sneddon model was developed to provide a practical computational solution to the contact problem solved by Boussinesq (Sneddon 1965). Boussinesq was the first to derive the deformation of an elastic surface by a body of revolution; however his solutions did not produce exact numerical outputs. With the use of Hankel transforms and double integrals, Sneddon was able to describe the contact between an elastic solid and a rigid axisymmetric indenter by first finding explicit formulations for the depth of the indenter penetration, D, and the total load exerted by the indenter onto the elastic solid and then developing a relationship between the two. The Sneddon model is commonly used to describe the contact between a conical indenter and an elastic body. Using the Sneddon model for a conical indenter, the relationship between the force and indentation is as follows (Sneddon 1948):

$$F = \frac{2\,E}{\pi\,(1-\,\nu^2)\,\tan\alpha}\,D^2 \qquad \text{Eq. 5.3}$$

where F [N] is the applied force, E [N/m^2 or Pascal] is the Young's modulus of elasticity of the sample of interest, ν [dimensionless] is the Poisson's ratio, α [dimensionless] is the cone semi-vertical angle, and D [m] is the indentation. The Sneddon model is valid under the following assumptions (Sneddon 1948, Poon *et al.* 2008):

- The sample is isotropic, homogenous, and linearly elastic
- The sample is infinitely thick
- The sample and indenter are both frictionless, therefore adhesion is neglected
- The sample undergoes infinitesimally small strains
- The indenter has an ideal conical geometry with known parameters
- The sample indentation is higher than radius of curvature of the tip apex

5.2.4 Pyramidal Indenter

5.2.4.1 Bilodeau Model

The Bilodeau model was the first to describe the contact problem between a regular, axisymmetric pyramidal indenter and an elastic half-space. With the Bilodeau model for a regular four-sided pyramid indenter, the relationship between the force and indentation is (Bilodeau 1992):

$$F = \frac{3\,E\,\tan\alpha}{4\,(1-\nu^2)}\,D^2 \qquad \text{Eq. 5.4}$$

where F [N] is the applied force, E [N/m^2 or Pascal] is the Young's modulus of elasticity of the sample of interest, ν [dimensionless] is the Poisson's ratio, α [dimensionless] is the pyramid semi- angle, and D [m] is the indentation. The Bilodeau model is valid under the following assumptions (Bilodeau 1992, Pillarisetti 2008, Rosenbluth 2008):

- The sample is isotropic, homogenous, and linearly elastic

- The sample is infinitely thick
- The sample and indenter are both frictionless, therefore adhesion is neglected
- The sample undergoes infinitesimally small strains
- The indenter is a sharp pyramid with perfect geometry and known parameters
- The lateral faces of the pyramid indenter are isosceles triangles of equal length and the base is an 4-sided polygon
- The boundary contact area is assumed to be a polygon of the same type as the pyramid base

5.2.4.2 Rico Model

Another pyramid model was developed by Rico *et al* (2005) to provide a more realistic contact mechanical model specifically for pyramidal atomic force microscopy cantilever tips. The Rico model takes into account the blunt geometry in which commercial AFM pyramidal tips are fabricated (Rico *et al.* 2005). This model describes the contact between a blunted pyramid and an elastic half-space. The blunted pyramid is modeled as a spherical cap that transitions into a 4-sided pyramid (Figure 5.1). With the Rico model for a blunted regular four-sided pyramid indenter, the relationship between the force and indentation can be described these two equations (Rico *et al.* 2005):

$$F = \frac{2E}{(1-\nu^2)}\left[Da - \frac{\sqrt{2}\,a^2}{\pi\,\tan\theta}\left(\frac{\pi}{2} - \sin^{-1}\frac{b}{a}\right) - \frac{a^3}{3R} + \sqrt{a^2-b^2}\left(\frac{\sqrt{2}\,b}{\pi\,\tan\alpha} + \frac{a^2-b^2}{3R}\right)\right] \quad \text{Eq. 5.5}$$

$$D - \frac{a\,\sqrt[3]{2}}{\pi\tan\theta}\left(\frac{\pi}{2} - \sin^{-1}\frac{b}{a}\right) + \frac{a}{R}\left[\left(\sqrt{a^2-b^2} - a\right)\right] = 0 \quad \text{Eq. 5.6}$$

where F [N] is the applied force, E [N/m^2 or Pascal] is the Young's modulus of elasticity of the sample of interest, ν [dimensionless] is the Poisson's ratio, θ [dimensionless] is the pyramid semi- angle, a [m] is the contact radius, b [m] is the radial distance from the transition between the spherical cap and pyramidal face, R [m] is the radius of the spherical cap of the blunted tip, and D [m] is the indentation. The contact radius, a, is defined as:

$$a = \frac{D \tan \theta}{\sqrt{2}} \qquad \text{Eq. 5.7}$$

The Rico model is valid under the following assumptions (Rico *et al.* 2005):

- The sample is isotropic, homogenous, and linearly elastic
- The sample is infinitely thick
- The sample and indenter are both frictionless, therefore adhesion is neglected
- The sample undergoes infinitesimally small strains

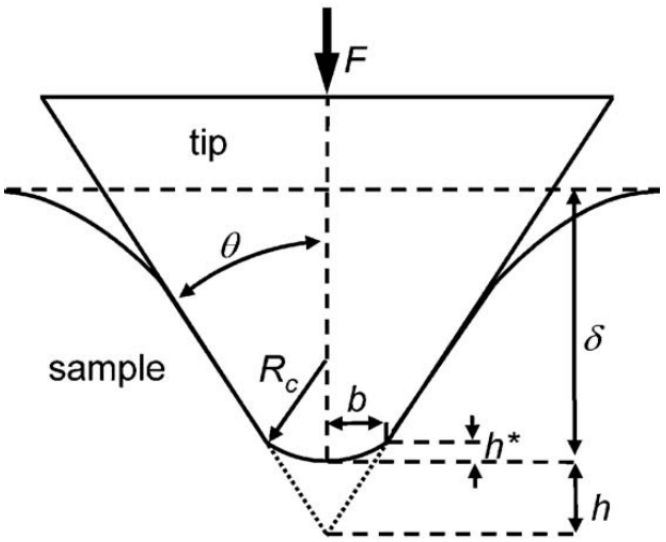

Figure 5.1: Diagram model of the blunted pyramidal indenter (Rico *et al.* 2005).

5.2.5 Multi-Layered Models

5.2.5.1 Overview

The models described above assume that the elastic body indented upon is of infinite sample thickness; thereby neglecting any effect that underlying layers or a substrate may have on the calculated mechanical results. As most biological samples are not isotropic and are comprised of multiple layers of distinct mechanical characteristics, like the cornea, it is important to take into account the influence of such subsequent layers. The generally accepted method to avoid underlying layers and substrate effects is to limit the indentation depth of the indenter on the sample to 10% of the measured layer's thickness (Fischer-Cripps 2002). However, this is not an effective method when the top layer is ultra-small with respect to the underlying layer or substrate. The following models address this important issue and describe the derivation of elastic mechanical properties of: (1) the top layer in bi-layered systems (King and Gao models) and (2) a single biological layer with the effects of a rigid substrate taken into account (Dimitriadis and Chadwick models). For all these models, adhesion is neglected.

5.2.5.2 King Model

The King model was developed to determine the elastic properties of thin films on rigid substrates during the unloading phase of indentation tests (King 1987). This model assumes the layered system to be an isotropic and elastic half-space and is based on infinitesimal indentation (King 1987, Seino 2007). Therefore, the model excludes the indentation depth (Seino 2007). Cylindrical, square, and triangular flat punches are valid for the King model. The main application of this model is the bi-layered systems of thin

metal films on rigid metal substrates (of known Young's modulus of elasticity). Both layers are assumed to be homogenous. The equation of the King model is:

$$\frac{1}{E_{comp}} = \frac{1 - \nu_{film}^2}{E_{film}}\left(1 - e^{\frac{-\alpha t}{a}}\right) + \frac{1 - \nu_{sub}^2}{E_{sub}}\left(e^{\frac{-\alpha t}{a}}\right) \quad \text{Eq. 5.8}$$

where E_{comp} [N/m^2 or Pascal] is the effective composite Young's modulus of elasticity, ν_{film} [dimensionless] is the Poisson's ratio of the thin film layer, E_{film} [N/m^2 or Pascal] is the effective Young's modulus of elasticity of the thin film, ν_{sub} [dimensionless] is the Poisson's ratio of the substrate layer , E_{sub} [N/m^2 or Pascal] is the effective Young's modulus of elasticity of the substrate layer, a [m] is the square root of the projected contact area of a flat punch contact radius, t [m] is the thickness of the thin film layer, and α [dimensionless] is a numerical scaling parameter that is function of a/t.

5.2.5.3 Gao Model

The Gao model describes the elastic contact problem solution of a rigid cylindrical or conical punch indenting a multilayered system of linear elasticity (Gao *et al.* 1992). Like the King model, it also models the unloading phase of an indentation test of thin films on a substrate and has the main application of thin metal films on rigid metal substrates, assuming homogeneity in each layer. The Gao model can be defined as (Gao *et al.* 1992):

$$E_{effective} = E_{substrate}\left(E_{film} - E_{substrate}\right)I_o \quad \text{Eq. 5.9}$$

$$I_o = \frac{2}{\pi}\tan^{-1}\frac{t}{a} + \frac{1}{2\pi(1-\nu)}\left[(1-2\upsilon)\,\frac{t}{a}\,\ln\left(\frac{1+\left(\frac{t}{a}\right)^2}{\left(\frac{t}{a}\right)^2}\right) - \frac{\frac{t}{a}}{1+\left(\frac{t}{a}\right)^2}\right] \quad \text{Eq. 5.10}$$

where $E_{effective}$ [N/m^2 or Pascal] is the combined effective Young's modulus of elasticity of the thin film and substrate, E_{film} [N/m^2 or Pascal] is the effective Young's modulus of

elasticity of the thin film, $E_{substrate}$ [N/m^2 or Pascal] is the effective Young's modulus of elasticity of the substrate layer, ν [dimensionless] is the Poisson's ratio of the thin film layer, a [m] is the contact radius, t [m] is the thickness of the thin film layer, and I_o [dimensionless] is the correction factor for determining the substrate effect as a function of film thickness and contact radius (t/a). Thus, I_o goes to zero as the thin film layer thickness (t) approaches zero, signifying maximal substrate effect and I_o goes to one as the thin film layer thickness (t) increases, thereby signifying minimal substrate effect in Eq. 5.9 (Gao *et al.* 1992).

5.2.5.4 Dimitriadis Model

The Dimitriadis model offers an analytical correction to the infinite sample thickness assumption of the Hertz model (Eq. 5.1). This model theory would, therefore, enable a more accurate determination of the elastic modulus of thin layers of soft material samples on a rigid substrate (Dimitriadis *et al.* 2002). The unique features of this model are its exclusion of layer thickness and its validity for all Poisson's ratio values (from 0-0.5) (Dimitriadis *et al.* 2002). The model equation of Dimitriadis *et al* (2002), establishing a relationship between the force and indentation of a spherical indenter punch on an elastic sample is:

$$F = \frac{4\,E\,R^{1/2}}{3\,(1\,-\,\nu^2)}\,D^{3/2}\left[1-\frac{2\alpha_0}{\pi}\chi+\frac{4\,{\alpha_0}^2}{\pi^2}\chi^2-\frac{8}{\pi^3}\left({\alpha_0}^3+\frac{4\pi^2}{15}\beta_0\right)\chi^3 + \frac{16}{\pi^4}\left({\alpha_0}^3+\frac{3\pi^2}{5}\beta_0\right)\chi^4\right] \quad \text{Eq. 5.11}$$

where $\chi = \frac{\sqrt{RD}}{h}$ in which h[m] is the sample thickness. α_0 and β_0 are constants that are functions of the sample's Poisson's ratio and can be defined as:

$$\alpha_0 = -0.347\,\frac{3-2\upsilon}{1-\upsilon} \qquad \text{Eq. 5.12}$$

$$\beta_0 = 0.056\,\frac{5-2\upsilon}{1-\upsilon} \qquad \text{Eq. 5.13}$$

The Dimitriadis model holds valid for sample thickness (h):

$$0.1R \leq h \leq 12.8R \qquad \text{Eq. 5.14}$$

for a sample thickness less than lower bound, the Chadwick model (Chadwick 2002) can be used and for a sample thickness greater than the upper bound, the Hertz model (Hertz 1881) can be used (Dimitriadis *et al.* 2002).

5.2.5.5 Chadwick Model

The Chadwick model was motivated by the desire to use atomic force microscopy as a microindenter of thin biological samples to measure their Yong's modulus of elasticity (Chadwick 2002). This model provides a numerical solution for the case of indentation of a finite, thin, homogenous, isotropic, incompressible, elastic biological layer by a spherical indenter (Chadwick 2002). The model relates the force and indentation depth during indentation for the scenarios of when the sample is bonded and not bonded to the rigid substrate, respectively, below:

$$F = \frac{2\pi E R^2 D^3}{3\,h^3} \qquad \text{Eq. 5.15}$$

$$F = \frac{2\pi E R^2 D^2}{3\,h} \qquad \text{Eq. 5.16}$$

These two equations show that the force has significant dependence on the sample thickness (h), depending on whether the sample is bonded (Eq. 5.15) or not (Eq. 5.16).

The Chadwick model has validity only in the cases where:

$h < 500nm$ for the bonded sample

$h < 250nm$ for the non-bonded sample

5.2.5.6 Summary of Multi-Layered Models

Elastic characterization experiments were conducted to determine the feasibility of using the aforementioned multi-layered models on the corneal mechanical response. It has been shown in literature that the Young's modulus of Bowman's membrane is lower than that of the stiffer, underlying anterior stroma (see Table 2.2). Therefore, the goal of the feasibility study was to determine whether multi-layered models could mathematically extract the Young's modulus of the Bowman's membrane, if the Young's modulus of underlying anterior stroma layer is known.

Six human donor eye pairs (age: 77.2 ± 9.8 years; post-mortem time: 6.7 ± 2.1 days) were used in this study. Upon receipt from the Florida Lions Eye Bank (Miami,FL), the corneal epithelium was removed using a cotton-tipped applicator. Afterward, the eye globe was placed in 20% Dextran overnight to restore corneal thickness to the physiological range of 400-600μm. Pachymetry measurements were taken with an ultrasound pachymeter (DGH 55 Pachmate, DGH Technology Inc., Exton, PA) to ensure proper thickness restoration. For the left eyes of each pair (n=6), the Bowman's membrane was removed so that direct AFM mechanical testing on the corneal anterior stroma could be performed. The right eyes of each pair (n=6), which were not subjected to any corneal layer removal, were reserved for AFM mechanical testing on Bowman's layer. To perform mechanical testing, all corneas were excised from the eye

globe with a generous scleral rim left intact and placed in a custom corneal holder that was then filled with 15% Dextran to maintain corneal hydration during testing. Modified AFM cantilever tips with spherical microbeads (diameter range: 56-80um) were used in this study. AFM mechanical testing of the corneas yielded force-indentation curves, which were used to derive the Young's modulus of the anterior stroma from the Hertz model (Eq. 5.1). The anterior stromal Young's modulus values were used as the effective Young's modulus of elasticity of the substrate layer in the King and Gao models (E_{sub} and $E_{substrate}$, respectively). The Young's modulus of the Bowman's membrane was mathematically calculated using the respective analytical solutions of King (Eq. 5.8), Gao (Eq. 5.9), Dimitriadis (5.11), and Chadwick (Eq. 5.15 and 5.16).

For each model, Young's modulus of Bowman's membrane was calculated and then compared to that found in literature (7.5kPa; (Last *et al.* 2009)) (Figure 5.2). The calculated Young's moduli were 20.3, 5.7, 2.5, 80.5, and 10.6 times greater than the published values for the King, Gao, Dimitriadis, Chadwick Bonded, and Chadwick Non-bonded models, respectively. Such results show that the Dimitriadis most closely matches that of the published value and is somewhat effective in determining the elastic modulus of a thin layer on top of a stiffer underlying substrate, as in the case of Bowman's membrane on top of the stromal layer. Nonetheless, since all of these models were developed for experimental cases where the top layer is more compliant than the underlying layer and majority of the corneal mechanical experiments that will be conducted within the stroma, where the anterior stromal region is stiffer than the underlying posterior stromal region and Descemet's membrane, it is believed that these models are not effective for the application of corneal stroma mechanical

characterization. Therefore, it was decided to limit corneal stroma mechanical testing to direct indentation application on the particular corneal plane or layer of interest. For example, to obtain the elastic property of the anterior stromal region, the Bowman's membrane layer is first removed to enable direct AFM testing on the anterior stromal region. Small indentations (less than 10% of the stromal layer thickness) will be applied to minimize the substrate effects of the underlying Descemet's membrane layer.

5.3 Viscoelasticity Models

5.3.1 Overview

Materials that exhibit viscoelastic behavior encompass both elastic and viscoelastic properties in a time-dependent manner. One method to determine such properties of viscoelastic materials is through performing stress relaxation testing and analyzing the time-variant response. Models are often used to describe the viscoelastic behavior of materials through means including mechanical analogs as well as non-linear numerical methods.

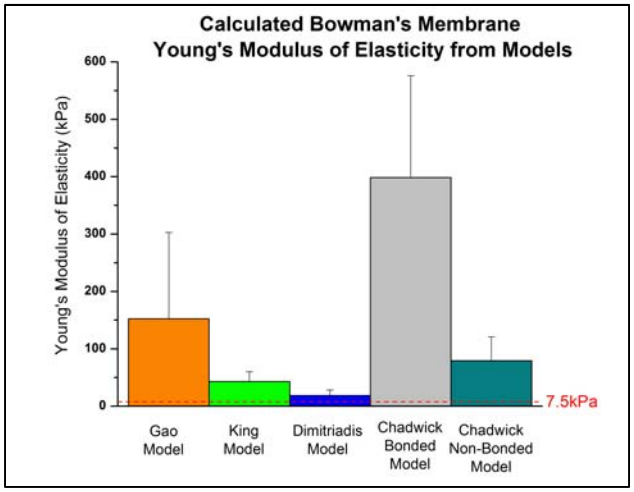

Figure 5.2: Bar Graph of Calculated Bowman's Membrane Young's Modulus from the Multi-Layered Models.

5.3.2 Standard Linear Viscoelastic Models

5.3.2.1 Overview

Linear viscoelasticity models rest on the premise that the relationship between the induced stress (or strain) and its resultant strain (or stress) response within a material is both linear and time-dependent. Such a relationship between stress and strain can be represented by the Volterra equations (Fung 1993):

$$\varepsilon(t) = \int_0^t C_R(t-z)\frac{d\sigma(z)}{dz}dz \qquad \text{Eq. 5.17}$$

$$\sigma(t) = \int_0^t K_R(t-z)\frac{d\varepsilon(z)}{dz}dz \qquad \text{Eq. 5.18}$$

where $\varepsilon(t)$ is the strain, $C_R(t-z)$ is the creep response, $\sigma(t)$ is the stress, and $K_R(t-z)$ is the stress relaxation response. Equations 5.17 and 5.18 can also be rewritten in terms force, F, and indentation, u, and are known as the Boltzmann integrals (Fung 1993):

$$u(t) = \int_0^t c_R(t-\tau)\frac{dF(\tau)}{d\tau}d\tau \qquad \text{Eq. 5.19}$$

$$F(t) = \int_0^t k_R(t-\tau)\frac{d\varepsilon(\tau)}{d\tau}d\tau \qquad \text{Eq. 5.20}$$

where $u(t)$ is displacement, $c_R(t-\tau)$ is the creep response, $F(t)$ is force, and $k_R(t-\tau)$ is the relaxation response. Equations 5.18 and 5.20 describe the case of stress relaxation. The main assumption of linear viscoelasticity is the application of only small deformations onto the material.

In addition to describing linear viscoelastic materials with Equations 5.17-5.20, such materials are also described using simple mechanical models to illustrate their viscoelastic behavior. The two mechanical analogs used are the dashpot and spring (Figure 5.3 and 5.4). The dashpot represents the viscous behavior of a material, likened to a piston moving inside a cylinder filled with fluid. Described as a Newtonian fluid, the

equation for a dashpot produces a velocity proportional to load at any time (Menard 2008):

$$\sigma = \mu \frac{d\varepsilon}{dt} \quad \text{Eq. 5.21}$$

where σ is stress, μ is viscosity, and $d\varepsilon/dt$ is the time derivative of strain. In terms of force and displacement, Eq. 5.21 can be rewritten as:

$$F = \mu \frac{du}{dt} \quad \text{Eq. 5.22}$$

where F is the force, μ is viscosity, and du/dt is the time derivative of the displacement. The spring represents the elastic behavior of the material and is described by Hooke's elastic solid (Ledoux and Ching 2014):

$$\sigma = E\varepsilon \quad \text{Eq. 5.23}$$

where σ is the stress, E is the elastic modulus, and ε is the strain. Or,

$$F = ku \quad \text{Eq. 5.24}$$

where F is the force, k is the spring constant, and u is the displacement.

With these two mechanical analogs, viscoelastic mechanical models have been developed to describe the viscoelastic behavior of materials (Fung 1993). The three most common viscoelastic models are the Maxwell, Voigt, and Kelvin models.

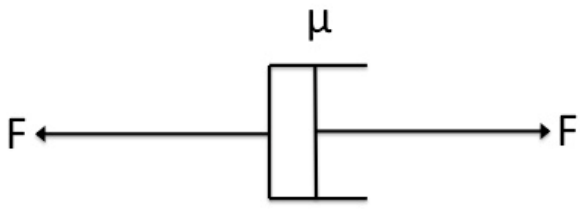

Figure 5.3: The dashpot mechanical analog with spring constant, k.

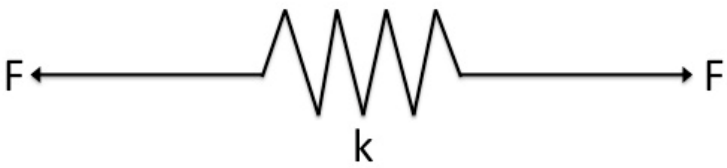

Figure 5.4: The spring mechanical analog with spring constant, k.

5.3.2.2 Maxwell Model

The Maxwell model encompasses the use of an elastic spring in series with a viscous dashpot ((Maxwell 1867); Figure 5.5). In this model setup, when an axial load is applied, the total displacement of the model is defined as:

$$u_T = u_k + u_\eta \qquad \text{Eq. 5.25}$$

where u_T is total displacement, u_k is the displacement experienced by the spring, and u_η is the displacement experienced by the dashpot. Equation 5.25 can be rewritten as:

$$\frac{du_T}{dt} = \frac{du_k}{dt} + \frac{du_\eta}{dt} \qquad \text{Eq. 5.26}$$

Since the same axial force is applied to both the spring and dashpot, the total force of the model is:

$$F_{total} = F_\eta = F_k \qquad \text{Eq. 5.27}$$

where F_{total} is the total force applied to the model, F_η is the force exerted on the dashpot, and F_k is the force exerted on the spring. Substituting F_η and F_k with Eq. 5.22 and 5.24, respectively, the total force can then be written as:

$$F_{total} = \eta \frac{du_\eta}{dt} = k u_k \qquad \text{Eq. 5.28}$$

Integrating Eq. 5.28 into Eq. 5.26 yields the general governing equation of the Maxwell model:

$$\frac{du_{total}}{dt} = \frac{du}{dt} = \frac{F}{\eta} = \frac{1}{k}\frac{dF}{dt} \quad \text{Eq. 5.29}$$

To determine the stress relaxation function, $k_r(t)$, for the Maxwell model, a unit-step function H(t) is assigned as the displacement, u, to signify the sudden deformation applied unto the viscoelastic material during stress relaxation testing. Therefore,

$$u(t) = H(t) \quad \text{Eq. 5.30}$$

and the stress relaxation function $k_r(t)$ is derived by combining Eq. 5.29 and Eq. 5.30:

$$\frac{dH(t)}{dt} = \frac{F}{\eta} = \frac{1}{k}\frac{dF}{dt} \quad \text{Eq. 5.31}$$

Taking the Laplace transform of Eq. 5.31 gives:

$$1 = \frac{1}{\eta}F(s) = \frac{1}{k}sF(s) \quad \text{Eq. 5.32}$$

where F(s) is the Laplace transform of the force. Isolating and solving F(s) gives:

$$1 = F(s)\left[\frac{1}{\eta} + \frac{1}{k}s\right] \quad \text{Eq. 5.33}$$

$$F(s) = \frac{1}{\left[\frac{1}{\eta} + \frac{1}{k}s\right]}\ x\ \frac{k}{k} = \frac{k}{\frac{k}{\eta} + s} \quad \text{Eq. 5.34}$$

To obtain the relaxation function, the inverse Laplace is then taken to get:

$$k_r(t) = f(t) = ke^{-\frac{k}{\eta}t} = ke^{-\frac{t}{\tau}} \quad \text{Eq. 5.35}$$

where τ is the relaxation time that characterizes the rate of decay of the force and is equivalent to η/k.

The Maxwell model is acceptable as a first approximation to relaxation behavior. Since the stress completely relaxes out over time, this model more describes that of a viscoelastic fluid than a viscoelastic solid (Tropea *et al.* 2007).

5.3.2.3 Voigt Model

The Voigt viscoelastic model is comprised of the spring and dashpot connected in parallel (Figure 5.6). In this model, the spring and dashpot experience the same displacement when an axial load is applied. The force experienced by the spring is:

$$F_{spring} = ku \quad \text{Eq. 5.36}$$

where F_{spring} is the force exerted on the spring, k is the spring constant, and u is the displacement. The force experienced by the dashpot is:

$$F_{dashpot} = \eta \frac{du}{dt} \quad \text{Eq. 5.37}$$

where $F_{dashpot}$ is the force exerted on the dashpot, η is the viscosity of the dashpot, and du/dt is the time derivative of the displacement. The total force of the Voigt model, F_{Total} , is sum of the individual components:

$$F_{Total} = F_{spring} + F_{dashpot} = ku + \eta \frac{du}{dt} \quad \text{Eq. 5.38}$$

This is the governing equation for the Voigt model.

The stress relaxation function $k_r(t)$ for the model is obtained by replacing the unit-step function H(t) for the displacement, u, in Eq. 5.38:

$$F(t) = kH(t) + \eta \frac{dH(t)}{dt} \quad \text{Eq. 5.39}$$

Taking the Laplace transform of Eq. 5.39 yields:

$$F(s) = k(1/s) + \eta \quad \text{Eq. 5.40}$$

Taking the inverse Laplace transform of Eq. 5.40, results in the relaxation function:

$$k_r(t) = f(t) = kH(t) + \eta\delta(t) \quad \text{Eq. 5.41}$$

This resultant relaxation function yields an inaccurate representation of stress relaxation response. The presence of the unit impulse suggests that the stress relaxation is

instantaneous. Therefore, the Voigt model is commonly not applied in stress relaxation studies (Rao and Deshpande 2014).

5.3.2.4 Kelvin Model

The Kelvin model is made up of a spring and dashpot connected series with one another and then placed in parallel with an additional spring (Figure 5.7). Similar to the Voigt model, when an axial load is applied to the system, the same displacement is experienced but different forces are exerted on the component. The total displacement, u_{Total}, is given by:

$$u_{Total} = u_{k0} = u_{k1} + u_{\eta} \quad \text{Eq. 5.42}$$

where u_{k0} is the displacement exerted on the spring with spring constant k_0, u_{k1} is the displacement exerted on the spring with spring constant k_1, and u_{η} is the displacement exerted on the dashpot. The forces of the respective components in this model are:

$$F_1 = k_1 u_{k1} = \eta \frac{du_{\eta}}{dt} \quad \text{Eq. 5.43}$$

$$F_2 = k_0 u \quad \text{Eq. 5.44}$$

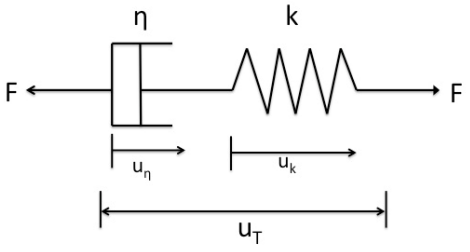

Figure 5.5: The Maxwell Model.

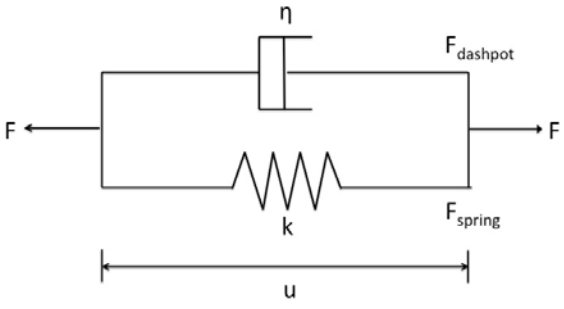

Figure 5.6: The Voigt Model.

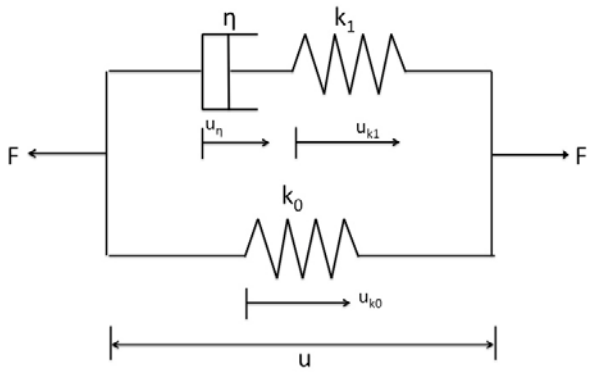

Figure 5.7: The Kelvin Model.

The total force, F_{Total}, is then given by:

$$F_{Total} = F_1 + F_2 = k_0 u + k_1 u_{k1} \quad \text{Eq. 5.45}$$

or

$$F_{Total} = F = F_1 + F_2 = k_0 u + \eta \frac{du_\eta}{dt} \quad \text{Eq. 5.46}$$

Taking the derivative of Eq. 5.45 yields:

$$\frac{dF_{Total}}{dt} = \frac{dF}{dt} = k_0 \frac{du}{dt} + k_1 \frac{du_{k1}}{dt} \quad \text{Eq. 5.47}$$

Then, combining Eq. 5.47 with Eq. 5.46 will give:

$$k_1 \left[F = k_0 u + \eta \frac{du_\eta}{dt} \right] + \eta \left[\frac{dF}{dt} = k_0 \frac{du}{dt} + k_1 \frac{du_{k1}}{dt} \right] \quad \text{Eq. 5.48}$$

This can be rewritten as:

$$k_1 F + \eta \frac{dF}{dt} = k_0 k_1 u + k_0 \eta \frac{du}{dt} + k_1 \eta \left(\frac{du_\eta}{dt} + \frac{du_{k1}}{dt} \right) \quad \text{Eq. 5.49}$$

Simplifying Eq. 5.49 with the relation that $u = u_\eta + u_{k1}$ gives the governing equation for the Kelvin model:

$$k_1 F + \eta \frac{dF}{dt} = k_0 k_1 u + [k_0 \eta + k_1 \eta] \frac{du}{dt} \qquad \text{Eq. 5.50}$$

or

$$F + \tau_\varepsilon \frac{dF}{dt} = E_R \left[u + \tau_0 \frac{du}{dt} \right] \qquad \text{Eq. 5.51}$$

where E_R is the relaxed modulus and equivalent to k_0, τ_ε is the relaxation time for constant strain and equivalent to η/k, and τ_0 is the relaxation time for constant stress and is equivalent to:.

$$\tau_0 = \eta/k_0 \left(1 + {}^{k_0}/_{k_1} \right) \qquad \text{Eq. 5.52}$$

The stress relaxation response can be retrieved by plugging in the unit-step function as displacement in:

$$F + \tau_\varepsilon \frac{dF}{dt} = E_R \left[H(t) + \tau_0 \frac{dH(t)}{dt} \right] \qquad \text{Eq. 5.53}$$

Taking the Laplace transform of Eq. 5.53 yields:

$$F(s) = \frac{E_R}{s(\tau_\varepsilon s + 1)} + \frac{E_R \tau_0}{(\tau_\varepsilon s + 1)} = \frac{1}{\tau_\varepsilon} \left[\frac{E_R \tau_\varepsilon}{s} + \frac{E_R \tau_\varepsilon}{s + {}^{1}/_{\tau_\varepsilon}} \right] + \frac{1}{\tau_\varepsilon} \left[\frac{E_R \tau_0}{s + {}^{1}/_{\tau_\varepsilon}} \right] \qquad \text{Eq. 5.54}$$

The stress relaxation function of the Kelvin function is given by taking the inverse Laplace transform of Eq. 5.54:

$$k_r(t) = f(t) = E_R \left[1 - e^{-\frac{t}{\tau_\varepsilon}} + \frac{\tau_0}{\tau_\varepsilon} e^{-\frac{t}{\tau_\varepsilon}} \right] = E_R \left[1 + e^{-\frac{t}{\tau_\varepsilon}} \left(\frac{\tau_0}{\tau_\varepsilon} - 1 \right) \right] \qquad \text{Eq. 5.55}$$

The Kelvin model is a common model used to describe the viscoelastic behavior of biological samples (Fung 1993, Tropea *et al.* 2007).

The Maxwell, Voigt, and Kelvin models are all based on the linear viscoelasticity with the assumption of infinitesimal strain and have the main drawback of limiting the relaxation of a viscoelastic material to only one single time occurrence. As a result, many different models have been developed by merging these three basic models in various ways to increase improve the mechanical representation of viscoelastic materials. Such models will be discussed in the next sections.

5.3.3 Advanced Linear Viscoelastic Models

5.3.3.1 Overview

The models discussed in this section are comprised of different combinations of the standard viscoelastic models previously mentioned. Although a plethora of viscoelastic response solutions exist within literature, only models developed for AFM- or indentation-based stress relaxation responses are incorporated in this section. These models will first be fitted to a representative sample data set of the corneal viscoelastic responses; afterward, the coefficient of determination, R^2, will be calculated for each respective model to determine best viscoelastic model that describes corneal mechanical behavior.

5.3.3.2 Darling Model

The Darling model was developed to describe the viscoelastic properties of zonal articular chondrocytes measured using atomic force microscopy (Darling *et al.* 2006). The Darling model is a viscoelastic solution for small indentations of an isotropic, incompressible surface with a hard spherical indenter. Derived from the use of the Hertz

equation (Eq. 5.1) and the standard linear solid (or Kelvin) model (Eq. 5.48), the Darling stress relaxation model is given by the following force response (Darling *et al.* 2006):

$$F(t) = \frac{4R^{1/2}\delta_0^{1/2}E_R}{3(1-\nu)}\left[1 + \frac{\tau_0 - \tau_\varepsilon}{\tau_\varepsilon}e^{-\frac{t}{\tau_\varepsilon}}\right] \quad \text{Eq. 5.56}$$

where δ_0 is the penetration indentation depth that the stress relaxation occurs, E_R is the relaxed modulus, ν is the Poisson's ratio of the material, τ_0 is the relaxation time under constant load, τ_ε is the relaxation time under constant deformation, and R is the relative radius that describes the contact between the two spheres, that of the probe tip, R_{tip}, and that of the cell, R_{cell}. The relative radius is defined as (Darling *et al.* 2006):

$$R = \left(\frac{1}{R_{tip}} + \frac{1}{R_{cell}}\right)^{-1} \quad \text{Eq. 5.57}$$

From Darling relaxation response function (Eq. 5.56), the components of the standard linear solid model (which is also known as the Kelvin model) were defined as (Darling *et al.* 2006):

$$k_1 = E_R \quad \text{Eq. 5.58}$$

$$k_2 = E_R\left(\frac{\tau_0 - \tau_\varepsilon}{\tau_\varepsilon}\right) \quad \text{Eq. 5.59}$$

$$\mu = E_R(\tau_0 - \tau_\varepsilon) \quad \text{Eq. 5.60}$$

where k_1 and k_2 are the Kelvin spring elements and μ is the apparent viscosity.

The instantaneous and Young's moduli are respectively defined as (Darling *et al.* 2006):

$$E_0 = E_R\left(1 + \frac{\tau_0 - \tau_\varepsilon}{\tau_\varepsilon}\right) \quad \text{Eq. 5.61}$$

$$E_Y = \frac{3}{2}E_R \quad \text{Eq. 5.62}$$

where E_0 is the instantaneous modulus and E_Y is the Young's modulus.

5.3.3.3 Cheng Model

The Cheng model was developed with the application focus of probing the viscoelastic properties of solidifying/solidified polymeric coatings on substrates with indentation tests (Cheng *et al.* 2005). A viscoelastic solution was derived for a spherical indenter pressed into a semi-infinite medium under load relaxation conditions. The material assumptions of this model include that it is a linear viscoelastic solid and that it can be described as a standard linear solid model (in this case, a spring in series with the Voigt model; Figure 5.8). In addition, the Cheng model is said to be valid for both compressible and incompressible materials (Cheng *et al.* 2005).

Incorporating the Hertz model for a spherical indenter (Eq.5.1), the Cheng relaxation model is defined as (Cheng *et al.* 2005):

$$F(t) = \frac{4R^{1/2}\delta_0^{1/2}}{3} m\left(A_r e^{-\alpha_r t} + B_r e^{-\beta_r t} + C_r\right) \quad \text{Eq. 5.63}$$

where F(t) is the force, R is the radius of the spherical indenter, δ_0 is the penetration indentation depth at the stress relaxation hold, m is a material-dependent parameter given by:

$$m = (2G_1)c \quad \text{Eq. 5.64}$$

where G_1 is the shear modulus of the first spring element and is equivalent to :

$$G_1 = \frac{E_1}{2(1+\upsilon_1)} \quad \text{Eq. 5.65}$$

c is a non-dimensional coefficient equivalent to:

$$c = \frac{6K_1 + 2G_1}{3K_1 + 4G_1} \quad \text{Eq. 5.66}$$

where K_1 is the bulk modulus of the first spring element equivalent to

$$K_1 = \frac{E_1}{3(1-2\upsilon_1)} \quad \text{Eq. 5.67}$$

A_r, B_r, C_r, α_r, and β_r are all coefficients of the stress relaxation fit given by:

$$A_r = \frac{\left(1 - {}^{t_r}/_{t_c}\right)(b-1)}{a-1} \quad \text{Eq. 5.68}$$

$$B_r = \frac{\left(a - {}^{t_r}/_{t_c}\right)(a-b)}{a(a-1)} \quad \text{Eq. 5.69}$$

$$C_r = \frac{b}{a}\frac{t_r}{t_c} \quad \text{Eq. 5.70}$$

$$\alpha_r = \frac{1}{t_r} \quad \text{Eq. 5.71}$$

$$\beta_r = \frac{a}{t_r} \quad \text{Eq. 5.72}$$

where a, b, t_r, and t_c are material property-dependent parameters:

$$a = \frac{3K_1 + 4G^*}{3K_1 + 4G_1} \quad \text{Eq. 5.73}$$

$$b = \frac{6K_1 + 2G^*}{6K_1 + 2G_1} \quad \text{Eq. 5.74}$$

$$t_r = \frac{\eta}{G_1 + G_2} \quad \text{Eq. 5.75}$$

$$t_c = \frac{\eta}{G_2} \quad \text{Eq. 5.76}$$

For these parameters, G_2 is the shear modulus of the second spring element and is equivalent to:

$$G_2 = \frac{E_2}{2(1+\upsilon_2)} \quad \text{Eq. 5.77}$$

where η is the viscosity of the dashpot element in the model, and G^* is equal to:

$$G^* = \frac{G_1 G_2}{G_1 + G_2} \quad \text{Eq. 5.78}$$

For polymers that are assumed to be incompressible, where $\upsilon_1 = \upsilon_2 = 0.5$, the model is reduced to:

$$F(t) = \frac{16R^{1/2}\delta_0^{1/2}}{9} E_1 \left(\frac{E_1}{E_1 + E_2} e^{-\left(\frac{E_1+E_2}{3\eta}\right)t} + \frac{E_2}{E_1 + E_2} \right) \quad \text{Eq. 5.79}$$

It will be this version of the model that will be fitted to the corneal viscoelastic response.

5.3.3.4 Mattice Model

The Mattice Model was developed in efforts to examine the time-dependent mechanical response of soft biological tissues, porcine kidneys and costal cartilage, through spherical indentation. The starting point of the model was the Hertz model (Eq.5.1; (Mattice *et al.* 2006)):

$$F(t) = \frac{4R^{\frac{1}{2}}\delta_0^{\frac{1}{2}}E}{3(1-\upsilon^2)}\delta^{\frac{3}{2}} = \frac{8R^{\frac{1}{2}}}{3}[2G]\delta^{\frac{3}{2}} \quad \text{Eq. 5.80}$$

where F(t) is the load, δ is the indentation, R is the radius of the probe, E is the material elastic modulus, υ is the material Poisson's ratio, and G is the shear modulus. The relationship between the elastic and shear modulus for an incompressible solid (υ=0.5) is E=2G. The step load-relaxation experiment is then expressed by the relaxation response:

$$F(t) = \frac{8R^{\frac{1}{2}}}{3}\delta^{\frac{3}{2}}G(t) \quad \text{Eq. 5.81}$$

where G(t) is the relaxation function. Unlike the previously discussed models, Mattice used the Boltzmann hereditary integral operators to determine solutions for indentation load relaxation (Eq. 5.20). The generalized Boltzmann integral expression for spherical indentation under displacement control used by Mattice et al (2006) was:

$$F(t) = \frac{8R^{\frac{1}{2}}}{3}\int_0^t G(t-u)\left[\frac{d}{du}\delta^{\frac{3}{2}}(u)\right]du \qquad \text{Eq. 5.82}$$

where $G(t-u)$ is the relaxation function.

The Mattice model takes into account the displacement-controlled ramp portion to get to the stress-relaxation indentation hold, δ_{max}, as opposed to just assuming an instantaneous unit-step function. The displacement control is defined as:

$$\begin{matrix}\delta(t) = kt & for\ 0 \le t \le t_r \\ \delta(t) = kt_r = \delta_{max} & for\ t \ge t_r\end{matrix} \qquad \text{Eq. 5.83}$$

where δ is the indentation, k is the velocity of the indenter approaching the sample, and t_r is the rise time it takes the indenter to reach the stress relaxation indentation hold. However, due to displacement-controlled relaxation, the integral (Eq. 5.82) has no explicit analytical solution and must be solved numerically (Mattice *et al.* 2006). Therefore, to derive a relaxation response, a ramp-correction factor (RCF) is incorporated in the material relaxation function, G(t). The Mattice model defines G(t) as:

$$G(t) = C_0 + C_1e^{-t/\tau_1} + C_2e^{-t/\tau_2} + C_3e^{-t/\tau_3} \qquad \text{Eq. 5.84}$$

where C_0, C_1, C_2, and C_3 are coefficients of the material relaxation function while τ_1, τ_2, and τ_3 are relaxation time constants. In addition, the load relaxation function in terms of force, F, is given as (Mattice *et al.* 2006):

$$F(t) = B_0 + B_1e^{-t/\tau_1} + B_2e^{-t/\tau_2} + B_3e^{-t/\tau_3} \qquad \text{Eq. 5.85}$$

where B_0, B_1, B_2, and B_3 are coefficients of the load relaxation function and τ_1, τ_2, and τ_3 are relaxation time constants. The coefficients of the load relaxation function, B_0, B_1, B_2, and B_3 correspond to the coefficients of the material relaxation function as:

$$C_0 = \frac{B_0}{\delta_{max}\left(\frac{8\sqrt{R}}{3}\right)} \quad \text{Eq. 5.86}$$

$$C_k = \frac{B_k}{(RCF_k)\delta_{max}\left(\frac{8\sqrt{R}}{3}\right)} \text{ for k= 1, 2, and 3} \quad \text{Eq. 5.87}$$

where RCF_k is the ramp correction factor that defines the analytical difference between the observed values for analysis using ramp loading as opposed to the unit-step assumption and is given by:

$$RCF_k = \frac{\tau_k}{t_r}\left[e^{\frac{t_r}{\tau_k}} - 1\right] \text{ for k=1, 2, and 3} \quad \text{Eq. 5.88}$$

where τ_k (for k=1-3) are the relaxation time constants and t_r is the rise time it takes the indenter to reach the stress relaxation indentation hold. From these coefficients, the instantaneous shear modulus (G_0) and long term shear modulus (G_∞) values can be calculated as:

$$G_0 = \frac{G(0)}{2} = \frac{C_0 + C_1 + C_2 + C_3}{2} \quad \text{Eq. 5.89}$$

and

$$G_\infty = \frac{C_0}{2} \quad \text{Eq. 5.90}$$

The instantaneous and long term elastic modulus values, E_0 and E_∞, can also be calculated with the relationship, G=3E:

$$E_0 = \frac{G_0}{3} \quad \text{Eq. 5.91}$$

$$E_\infty = \frac{G_\infty}{3} \quad \text{Eq. 5.92}$$

This Mattice model has been used by Yoo *et al* (2011) to characterize the viscoelastic properties of bovine sclera, iris, crystalline lens, connective tissue, and kidney fat as well human orbital fat, eye-lid fat, and dermal fat (Yoo *et al.* 2011).

5.3.3.5 Kaufman Model

The Kaufman *et al* (2008) study purposed to establish a correlation between material properties obtained from hydrated nanoindentation and that of macroscale testing. To achieve this goal, nanoindentation and unconfined compression stress relaxation testing was performed on poly-2-hydroxyethyl methacrylate (pHEMA) hydrogels constructed at varied crosslinking concentrations. The Maxwell-Weichert model, which is a generalized mechanical model of one spring element connected in parallel with *j* Maxwell elements, was used to model the viscoelastic behavior of these hydrogels (Figure 5.9). In particular, only 2 Maxwell elements (*j*=2) were incorporated in the model, creating 3 springs and 2 dashpots (Kaufman *et al.* 2008).

In the Maxwell-Weichert model, each arm shares the same applied stress (or force) resulting in:

$$\sigma = \sigma_e + \sigma_1 + \sigma_2 \qquad \text{Eq. 5.93}$$

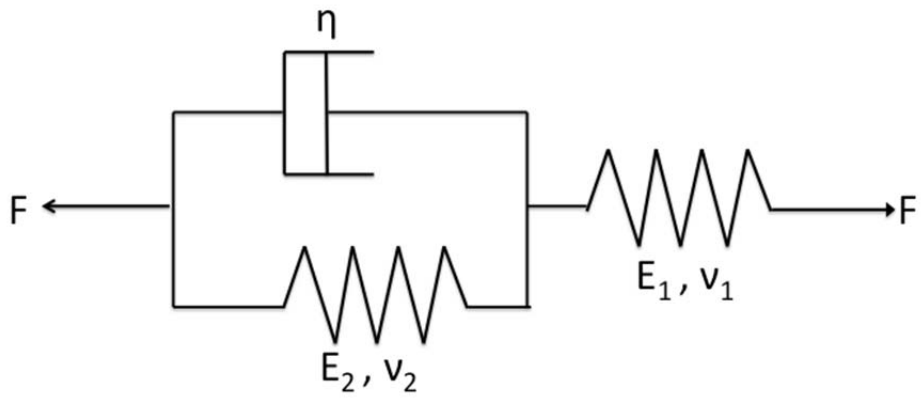

Figure 5.8: The Cheng Viscoelastic model.

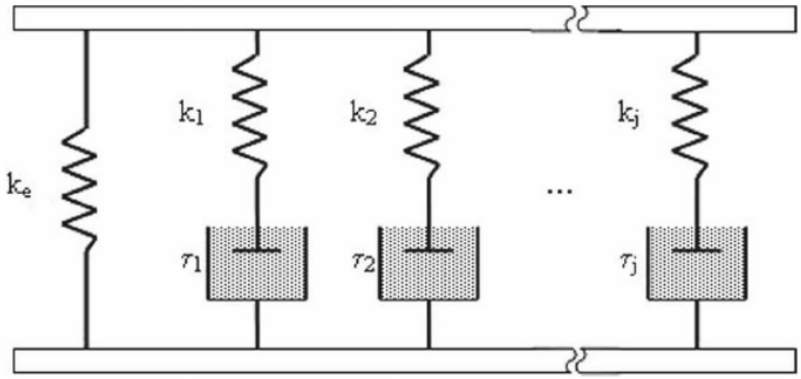

Figure 5.9: The Maxwell-Weichert Viscoelastic model used by Kaufman *et al* (2008).

At constant strain $\in_0$ (or indentation), the stress relaxation relationship between stress and strain is:

$$\sigma(t) = \left\{k_e + \sum k_j e^{-t/\tau_j}\right\} \in_0 \qquad \text{Eq. 5.94}$$

The relaxation modulus function $G_{rel}(t)$ is obtained by dividing the constant strain on both sides of Eq. 5.94:

$$G_{rel}(t) = k_e + \sum k_j e^{-t/\tau_j} \qquad \text{Eq. 5.95}$$

To model the behavior of soft material in stress relaxation testing, Eq. 5.95 can be placed in the Hertzian elastic solid equation to yield:

$$F(t) = \frac{8R^{1/2}\delta^{3/2}}{3(1-v)}\left[k_e + k_1 e^{-t/\tau_1} + k_2 e^{-t/\tau_2}\right] \qquad \text{Eq. 5.96}$$

5.3.3.6 Wang Model

Wang *et al* (2013) developed a viscoelastic solution of stress relaxation to determine the microrheology of cancer cells using AFM. The Wang model incorporates two correction factors to the Hertz model (Eq. 5.1; (Hertz 1881)) that take into account large indentation and the finite thickness of the biological material. The correction factor

for large indentation was developed by comparing the force calculated by finite-element modeling (FEM) and numerical computation using the Hertz equation (Wang *et al.* 2013). This comparison yielded the correction factor:

$$F = \frac{4R^{1/2}h^{3/2}}{3(1-v^2)}\left(1 - \frac{h}{10R}\right) \quad \text{Eq. 5.97}$$

where F is the force, R is the radius of spherical indenter, h is the indentation, and v is the Poisson's ratio of the material.

The correction factor, f(h), for the finite thickness of the sample, L, was adopted from the work of Srinivasa and Eswara (2008) (Srinivasa and Eswara 2008):

$$f(h) = 1 - \frac{2\alpha_0}{\pi}\frac{\sqrt{R}}{L}\sqrt{h} + \frac{4{\alpha_0}^2}{\pi^2}\frac{R}{L^2}h - \frac{8}{\pi^3}\left({\alpha_0}^3 + \frac{4\pi^2}{15}\beta_0\right)\frac{R^{\frac{3}{2}}}{L^3}h^{\frac{3}{2}} + \frac{16\alpha_0}{\pi^4}\left({\alpha_0}^3 + \frac{3\pi^2}{5}\beta_0\right)\frac{R^2}{L^4}h^2 \quad \text{Eq. 5.98}$$

where

$$\alpha_0 = -\frac{1.2876 - 1.4678v + 1.3442v^2}{1-v} \quad \text{Eq. 5.99}$$

$$\beta_0 = \frac{0.6387 - 1.0277v + 1.5164v^2}{1-v} \quad \text{Eq. 5.100}$$

The Wang model describes the cells with the Zener model (or Kelvin model), which is comprised of a spring with shear modulus G_0 connected in parallel with a Maxwell element of a spring with shear modulus G_1 and dashpot of viscosity η_1 (Figure 5.10). The relaxation function for this model is:

$$G(t) = G_0 + G_1 e^{-t/\tau_1} \quad \text{Eq. 5.101}$$

where τ_1 is the relaxation time of the Maxwell branch, equivalent to:

$$\tau_1 = {\eta_1}/{G_1} \quad \text{Eq. 5.102}$$

The load response for this model, which is fitted to the experimental data, is:

$$F(t) = \frac{16\sqrt{R}}{3}\left[(G_0 + G_1)\, h(t)^{3/2}\, g\big(h(t)\big) - F_1(t)\right] \quad \text{Eq. 5.103}$$

where h(t) is the indentation profile during the stress relaxation, including the initial ramp-up portion to arrive to the indentation depth hold, g(h(t)) is the function combining both correction factors equivalent to:

$$g(h) = \left[\left(1 - \frac{h}{10R}\right) f(h)\right] \quad \text{Eq. 5.104}$$

$F_1(t)$ is the function that takes into account the possibility that relaxation occurs during the indentation ramp-up portion. This function is equivalent to:

$$F_1(t) = \frac{G_1}{\tau_1}\int_0^t e^{-\frac{(t-t')}{\tau_1}} h(t')^{3/2} g\left(h(t')\right) dt' \quad \text{Eq. 5.105}$$

5.3.3.7 Cheneler Model

With the goal of extending the work of Dimitriadis *et al* (2002), the Cheneler model was developed to obtain viscoelastic mechanical behavior of thin layers of soft materials. Cheneler *et al* (2013) solved for the viscoelastic equation of the generalized standard linear solid model, which is comprised of *N* paralleled elements of a spring in series with the Voigt model (Figure 5.11; (Ferry 1980)). Afterward, the Dimitriadis model was incorporated to take into account the thickness of a thin film and the effects of its underlying substrate. For corneal viscoelastic analysis, however, only the uncorrected viscoelastic model solution of Cheneler *et al* (2013), not including the Dimitriadis modification, will be used for analysis since the thickness of the corneal stroma cannot be assumed to be a thin film in relation to its thinner underlying substrate, Descemet's membrane.

The general Cheneler relaxation response to the generalized standard linear solid model (Figure 5.8) is (Cheneler *et al.* 2013):

$$\Psi(t) = \sum_{n=1}^{N} \left[\left(\frac{k_{1n} k_{2n}}{k_{1n} + k_{2n}} \right) + \left(\frac{{k_{1n}}^2}{k_{1n} + k_{2n}} \right) e^{-t/T_n} \right] \quad \text{Eq. 5.106}$$

where N is the number of elements within the model, T_n represents the relaxation time constants for each element N and is equivalent to:

$$T_n = \frac{\eta_n}{k_{1n} + k_{2n}} \quad \text{Eq. 5.107}$$

k_{1n} is the spring constant of the spring in series with the Voigt model for each element N, k_{2n} is the spring constant of the spring within the Voigt configuration for each element N, and η is the viscosity of the dashpot within the Voigt configuration within each element N. This stress relaxation model relates to the shear modulus by the mathematical relations (Oyen 2006, Cheneler *et al.* 2013):

$$\sigma(t) = \Psi(t)\gamma_0 \quad \text{Eq. 5.108}$$

$$\sigma(t) = 2\mathrm{G}(t)\gamma_0 \quad \text{Eq. 5.109}$$

Therefore,

$$\mathrm{G}(t) = \Psi(t)/2 \quad \text{Eq. 5.110}$$

where $\sigma(t)$ is the stress, γ_0 is the constant strain, and $\mathrm{G}(t)$ is the shear relaxation modulus. The shear relaxation modulus can then be equated as:

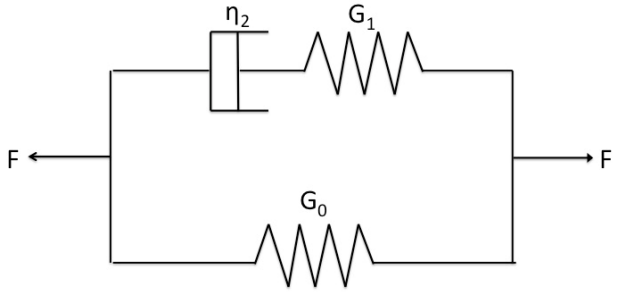

Figure 5.10: The Zener (or Kelvin) Viscoelastic model used by Wang *et al* (2013).

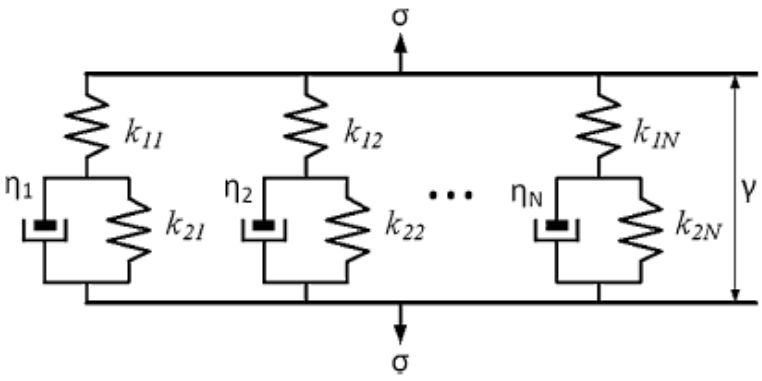

Figure 5.11: The Generalized Standard Linear Solid Viscoelastic model used by Cheneler *et al* (2013).

$$\mathrm{G}(t) = \frac{1}{2}\sum_{n=1}^{N}\left[\left(\frac{k_{1n}k_{2n}}{k_{1n}+k_{2n}}\right) + \left(\frac{{k_{1n}}^2}{k_{1n}+k_{2n}}\right)e^{-t/T_n}\right] \qquad \text{Eq. 5.111}$$

The limits of Eq. 5.111 are when t=0 and t=∞, respectively. When t=0, G(0) describes the instantaneous shear modulus of the material (Eq. 5.112). When t=∞, G(∞) describes the relaxed shear modulus (Eq. 5.113).

$$\mathrm{G}_0 = G(0) = \frac{1}{2}\sum_{n=1}^{N}[k_{1n}] \qquad \text{Eq. 5.112}$$

$$\mathrm{G}_\infty = G(\infty) = \frac{1}{2}\sum_{n=1}^{N}\left[\left(\frac{k_{1n}k_{2n}}{k_{1n}+k_{2n}}\right)\right] \qquad \text{Eq. 5.113}$$

Using equations 5.110, 5.111, 5.112, and 5.113, the stress relaxation model can then be simplified to:

$$\Psi(t) = 2\mathrm{G}_\infty + 2\sum_{n=1}^{N}\left[G_n e^{-t/T_n}\right] \qquad \text{Eq. 5.114}$$

Relating the stress relaxation response to the force and indentation, the contact force of a spherical indenter is given by:

$$\mathrm{F}_0(t) = \frac{8}{3R}\int_0^t \Psi(t-\tau')\frac{d}{d\tau'}a^3(\tau')d\tau' \qquad \text{Eq. 5.115}$$

where R is the radius of the spherical indenter, $\Psi(t-\tau')$ is the relaxation response (Eq.5.114), and a is the contact radius, which is given by:

$$a = \sqrt{R\delta} \qquad \text{Eq. 5.116}$$

where δ is the penetration depth of the spherical indenter into the viscoelastic material.

For this model, the corneal viscoelastic response was fit to the Cheneler model for the instance where N=2.

5.3.4 Quasi-linear Viscoelasticity: Tripathy Model

Up until this point, the models described use phenomenological spring-dashpot models to describe the relaxation of viscoelastic materials obtained by AFM. The use of such discrete models corresponds to the assumption that the viscoelastic material has a discrete hysteresis response, as evidenced by discrete relaxation time constants (Tripathy and Berger 2009). However, it has been observed that the hysteresis curves of biological viscoelastic samples are independent of strain over a range of frequencies (Fung 1965, Fung 1993, Tripathy and Berger 2009). To provide a more realistic representation of biological materials, the quasi-linear viscoelastic (QVL) theory was developed, describing the viscoelastic relaxation response as a continuous spectrum, as opposed to discrete time constants (Neubert 1963, Fung 1965, Fung 1993). The application of this theory has been established for uniaxial compression testing, but not for indentation testing. Therefore, with the intent of addressing this model deficiency, Tripathy and Berger developed an analytical model extending the QVL theory to AFM indentation data (Tripathy and Berger 2009, Tripathy and Berger 2012).

The QVL theory describes the relaxation function of a viscoelastic material as (Fung 1993):

$$\mathrm{K}(\lambda, \mathrm{t}) = T^{(e)}(\lambda)G(t) \qquad \text{Eq. 5.117}$$

where $\mathrm{K}(\lambda, \mathrm{t})$ is the relaxation function, $T^{(e)}(\lambda)$ is the instantaneous elastic response, which is only a function of stretch (λ), and $G(t)$ is normalized function of time called the reduced relaxation response (Fung 1993). To extend this theory to AFM indentation data, Eq. 5.117 can be combined with Eq. 5.18 to yield (Tripathy and Berger 2009):

$$\mathrm{F(t)} = \int_0^t G(t-\tau)\frac{dT^{(e)}(\delta)}{d\delta}\frac{d\delta(\tau)}{d\tau}d\tau \qquad \text{Eq. 5.118}$$

where F(t) is the force response, δ is the penetration depth, $G(t-\tau)$ is the relaxation response, and $T^{(e)}(\delta)$ is the instantaneous response. For indentation testing, $T^{(e)}(\delta)$, is equivalent to the Hertzian solution for spherical indenter on an elastic half-space:

$$T^{(e)}(\delta) = \frac{16}{9}R^{1/2}E\delta^{3/2} \qquad \text{Eq. 5.119}$$

where R is the radius of the spherical indenter and E is the Young's modulus. In addition, the generalized reduced relaxation function, G(t) is written as:

$$G(t) = \frac{1 + \int_0^\infty S(\tau)e^{-t/\tau}d\tau}{1 + \int_0^\infty S(\tau)d\tau} \qquad \text{Eq. 5.120}$$

where τ is a continuous variable and $S(\tau)$ is a function describing the amplitude of the viscous effects as a continuous function of time, thereby yielding a continuous spectrum of the relaxation times. This special function, $S(\tau)$, is equivalent to (Fung 1993):

$$S(\tau) = \begin{cases} \dfrac{C}{\tau}, & for: \tau_1 < \tau < \tau_2 \\ 0, & for: \tau < \tau_1, \tau > \tau_2 \end{cases} \qquad \text{Eq. 5.121}$$

where C is a material parameter that needs to be determined and τ_1 and τ_2 are the time limits for which the relaxation function is continuous. Plugging Eq. 5.121 into Eq. 5.120, the reduced relaxation function can be rewritten as:

$$G(t) = \frac{1 + C\left[E_1(\frac{t}{\tau_2}) - E_1(\frac{t}{\tau_1})\right]}{1 + Cln(\frac{\tau_2}{\tau_1})} \quad \text{Eq. 5.122}$$

where $E_1(t)$ is an exponential integral defined as:

$$E_1(t) = \int_t^{\infty} \frac{e^{-\tau}}{\tau} d\tau \quad \text{Eq. 5.123}$$

In addition, Tripathy incorporated two approximations to describe the indentation depth profile during stress relaxation testing. The first approximation is the commonly used indentation depth description of a ramp-up and hold period, which is referred as linear averaging (LA) in Tripathy's model (Tripathy and Berger 2009):

$$\delta = \begin{cases} kt, & for:\ 0 < t < t_1 \\ kt_1, & for: t_1 \leq t < \infty \end{cases} \quad \text{Eq. 5.124}$$

where k is the ramp slope and t_1 is the end of the ramp time.

The other approximation was developed to take into account the possibility of gradual increase in indentation depth during the hold period due to the decrease in cantilever deflection as the viscoelastic material relaxes. As a result, the indentation depth hold period is fitted to an exponential function (Tripathy and Berger 2009):

$$\delta = \begin{cases} kt, & for:\ 0 < t < t_1 \\ P_1 e^{P_2 t} + P_3 e^{P_4 t}, & for: t_1 \leq t < \infty \end{cases} \quad \text{Eq. 5.125}$$

where P_1,P_2, P_3, P_4 are the parameters derived from the fitting the exponential function. This approximation is referred as the exponential approximation (EA) in Tripathy's model.

The force response of the material due to stress relaxation can then be equated by plugging Eq. 5.119, Eq. 5.122, and the respective approximations of indentation depth: Eq. 5.124 and Eq. 5.125 into Eq. 5.118 (Tripathy and Berger 2009):

- For ramp-up period of the indentation depth, the force response is given as:

$$P(t:\langle 0,t_1\rangle)=\frac{\frac{8}{3}R^{1/2}k^{3/2}}{1+Cln(\frac{\tau_2}{\tau_1})}\int_0^t\left[1+C\left\{E_1(\frac{t-\tau}{\tau_2})-E_1(\frac{t-\tau}{\tau_1})\right\}\tau^{1/2}\right]d\tau \quad \text{Eq. 5.126}$$

- During the hold period, the LA model is given as:

$$P(t:\langle t_1,\infty\rangle)=\frac{\frac{8}{3}R^{1/2}k^{3/2}}{1+Cln(\frac{\tau_2}{\tau_1})}\int_0^{t_1}\left[1+C\left\{E_1(\frac{t-\tau}{\tau_2})-E_1(\frac{t-\tau}{\tau_1})\right\}\tau^{1/2}\right]d\tau \quad \text{Eq. 5.127}$$

- During the hold period, the EA model is given as:

$$P(t:\langle t_1,\infty\rangle)=\frac{\frac{8}{3}R^{1/2}k^{3/2}}{1+Cln(\frac{\tau_2}{\tau_1})}\left(\int_0^{t_1}\left[1+C\left\{E_1(\frac{t-\tau}{\tau_2})-E_1(\frac{t-\tau}{\tau_1})\right\}\tau^{1/2}\right]d\tau + \int_{t_2}^{t}\left[1+C\left\{E_1(\frac{t-\tau}{\tau_2})-E_1(\frac{t-\tau}{\tau_1})\right\}\mathrm{M}^{1/2}\frac{d\mathrm{M}}{d\tau}\right]d\tau\right) \quad \text{Eq. 5.128}$$

where M and its derivative $\frac{dM}{d\tau}$ are respectively equivalent to:

$$\mathrm{M}=P_1e^{P_2t}+P_3e^{P_4t} \quad \text{Eq. 5.129}$$

$$\frac{dM}{d\tau}=P_1P_2e^{P_2t}+P_3P_4e^{P_4t} \quad \text{Eq. 5.130}$$

and t_2 is the next time step after t_1 in the discrete AFM data. Therefore, four material parameters that the Tripathy model yields are E, C, τ_1, and τ_2.

5.4 Poroelasticity Models

5.4.1 Overview

Hydrogels, as well as most biological tissues including the cornea, are comprised of both solid and fluid components. These materials can be classified as porous, in which its solid matrix is interconnected with a network of fluid-filled pores. The viscoelasticity of such materials gives insight into their time-dependent behaviors due to the exertion of force or indentation, but does not take into consideration these materials' structural composition. The mechanical behavior of a material comprised of both solid and fluid

constituents can be described by its poroelastic properties. Therefore, poroelasticity models provide the interaction between the deformation of the elastic solid matrix and the flow of the viscous fluid embedded within the solid matrix of porous materials (Cowin 1999). Poroelastic properties of a material give insight not only into the time-dependent nature of the material, as in the case of viscoelasticity, but also into the material's transport properties. Poroelastic properties can be derived from performing either creep or stress relaxation tests using various experimental techniques including unconfined and confined compression testing as well as tensile stretching. However, this section encompasses the poroelastic model developed for AFM- or indentation-based stress relaxation testing.

5.4.2 Kalcioglu-Hu Model

Kalcioglu *et al* (2012) sought to extend and validate the load relaxation approach of Hu *et al* (2010) to derive the poroelastic properties of hydrated hydrogels using indentation testing. This was achieved by comparing the poroelastic analysis of hydrogels at the microscale (using AFM indentation with a $45\mu m$ diameter probe) and macroscale (using indentation with a 2cm diameter probe) levels to determine whether poroelasticity could be identified as the dominant regime at the microscale level as well as to determine whether the elastic and transport properties of the hydrogels could be extracted accurately and more rapidly using microscale indentation than macroscale indentation. The method to derive the poroelastic parameters of shear modulus, Poisson's ratio of the elastic solid matrix within the porous material, diffusivity, and the intrinsic permeability from indentation testing originated from that of Hu *et al* (2010).

When an indenter presses onto the hydrogel at a fixed depth, h, the force on the indenter relaxes over time. At short times, the hydrogel acts as an incompressible solid since the there is no fluid diffusion within the network during this short duration; however, at extended times, the hydrogel acts like a compressible material (Kalcioglu *et al.* 2012). Therefore, for a spherical indenter pressed into an incompressible elastic solid, the force exerted by the indenter is given as:

$$F_0 = \frac{16}{3} Gah \qquad \text{Eq. 5.131}$$

where F_o is the initial force when penetration indentation depth during stress relaxation is first reached, G is the shear modulus, h is the indentation depth held constant during stress relaxation, and a is the radius of contact (Eq. 5.116).

The ratio of the initial force, F_o, and the fully relaxed force at long times, F_∞ is:

$$\frac{F_0}{F_\infty} = 2(1 - \nu_s) \qquad \text{Eq. 5.132}$$

where ν_s is the Poisson's ratio of the solid matrix.

Using Eq. 5.131 and Eq. 5.132, the shear modulus (G), and the Poisson's ratio of the solid matrix within the porous material (ν_s) can be calculated since F_o and F_∞ are known from the experimental data:

$$G = \frac{3}{16}\left(\frac{F_0}{ah}\right) \qquad \text{Eq. 5.133}$$

$$\nu_s = 1 - 0.5\left(\frac{F_0}{F_\infty}\right) \qquad \text{Eq. 5.134}$$

The study of Hu *et al* (2010) performed FEM simulations of different geometry indenters pressed against a porous medium to determine their respective poroelastic contact solutions. From that study, the poroelastic contact solution of a spherical indenter pressed against a porous medium is given as (Hu *et al.* 2010):

$$g(\tau) = 0.491e^{-0.908\sqrt{\tau}} + 0.509e^{-1.679\tau} \quad \text{Eq. 5.135}$$

where $g(\tau)$ is a dimensionless function of the poroelastic contact solution and τ is the characteristic relaxation time constant equivalent to:

$$\tau = \frac{Dt}{a^2} \quad \text{Eq. 5.136}$$

where *D* is the diffusivity, *t* is the time scale during stress relaxation, and *a* is the contact radius.

In relation to the stress relaxation response of the hydrogel, for the hydrogel to reach equilibrium, the solvent within the material must migrate a distance equivalent to the contact radius (Kalcioglu *et al.* 2012). Thus, at a given time *t*, the solvent migrates at a length equal to $\sqrt{Dt}$. Therefore, stress relaxation force response *F(t)* can be written as:

$$\frac{F(t) - F_\infty}{F_0 - F_\infty} = \mathrm{g}\left(\frac{Dt}{a^2}\right) \quad \text{Eq. 5.137}$$

The left-hand side of Eq. 5.137 measures how far away the hydrogel is away from reaching equilibrium (Kalcioglu *et al.* 2012). The calculation of diffusivity *D* can be conducted by finding the best fit of Eq. 5.137 to the experimental stress relaxation force response *F(t)*:

$$F(t) = \mathrm{g}\left(\frac{Dt}{a^2}\right)(F_0 - F_\infty) + F_\infty \quad \text{Eq. 5.138}$$

Lastly, the intrinsic permeability κ can be calculated using the equation:

$$\kappa = \frac{\mathrm{D}(1 - 2\nu_s)\eta}{2(1 - 2\nu_s)G} \quad \text{Eq. 5.139}$$

where η is the solvent viscosity, which was assumed to be that of water (0.89 x 10^{-3} Pa s) in the Kalcioglu *et al* (2012) study. However, in the case of our study, η will be that of PBS (0.90 x 10^{-3} Pa s;(Armstrong *et al.* 2004)) since PBS is the solvent used for making the dextran solutions.

5.5 Implementation of Models for Stress Relaxation on Sample Corneal Data

A corneal stress relaxation mechanical response data set of the control human anterior stroma was used as a sample data representative. Using the developed MATLAB curve-fitting codes, each viscoelastic and poroelastic model was applied to the data and the coefficient of determination, R^2, was calculated for each model. The most effective viscoelastic model to describe corneal stress relaxation mechanical response was then determined, while the applicability of the poroelastic model was assessed.

Selection of the most effective viscoelastic model was based not only on the model's ability to fit the corneal mechanical response well but also on whether the outcome of the model produced results of mechanical significance. The Darling, Cheng, Mattice, Wang, and Kaufman models correlated well with the representative corneal stress relaxation response data, yielding coefficients of determination close to 1 (Table 5.1; Figure 5.12). While fitting the representative corneal data in good agreement, the Darling model was chosen as most effective in describing the corneal stress relaxation response due to the model's ability to output a standard mechanical property of substantial meaning (apparent viscosity). Such ability enables a concrete measure for comparison to other materials as well as the results of other studies. It is important to note that the stress relaxation analytical solutions of these four models (Darling, Cheng, Mattice, Wang, and Kaufman) were developed to fit to the force stress relaxation response during the time that the cantilever is held constant at the prescribed indentation depth. The Cheneler model encompasses an analytical solution that incorporates the initial force response as the cantilever travels to prescribed indentation depth for stress relaxation in addition to the force stress relaxation response. This model was not as

effective in fitting the corneal data as the previous five models (Table 5.1; Figure 5.13). The Tripathy model could not successfully fit the sample corneal data due to the inability to converge to a solution during curve-fitting optimization.

The curve fit performance of the poroelastic Kalcioglu-Hu model proved adequate in describing the sample corneal data (Table 5.1; Figure 5.14); therefore, the diffusivity parameter can be successfully derived. However, the estimation of the Poisson's ratio of the solid matrix from Equation 5.134, and consequently the intrinsic permeability parameter, proved inadequate as the calculated value (v_s=0.03) suggesting that the cornea experiences minimal resultant transverse strain during axial indentation. The estimation of shear modulus also proved inadequate due to the calculation subjectivity to the initial force measurement obtained during stress relaxation testing, as opposed to taking into account the stress relaxation response profile. Therefore, only the model's output parameter of diffusivity can be used in describing the poroelastic behavior of the cornea.

Stress Relaxation Model	**Coefficient of Determination (R^2)**
Darling	0.962
Mattice	0.973
Cheng	0.950
Kaufman	0.961
Wang	0.950
Cheneler	0.375
Tripathy	----
Kalcioglu-Hu	0.604

Table 5.1: Table of Coefficients of Determination for the Stress Relaxation Models.

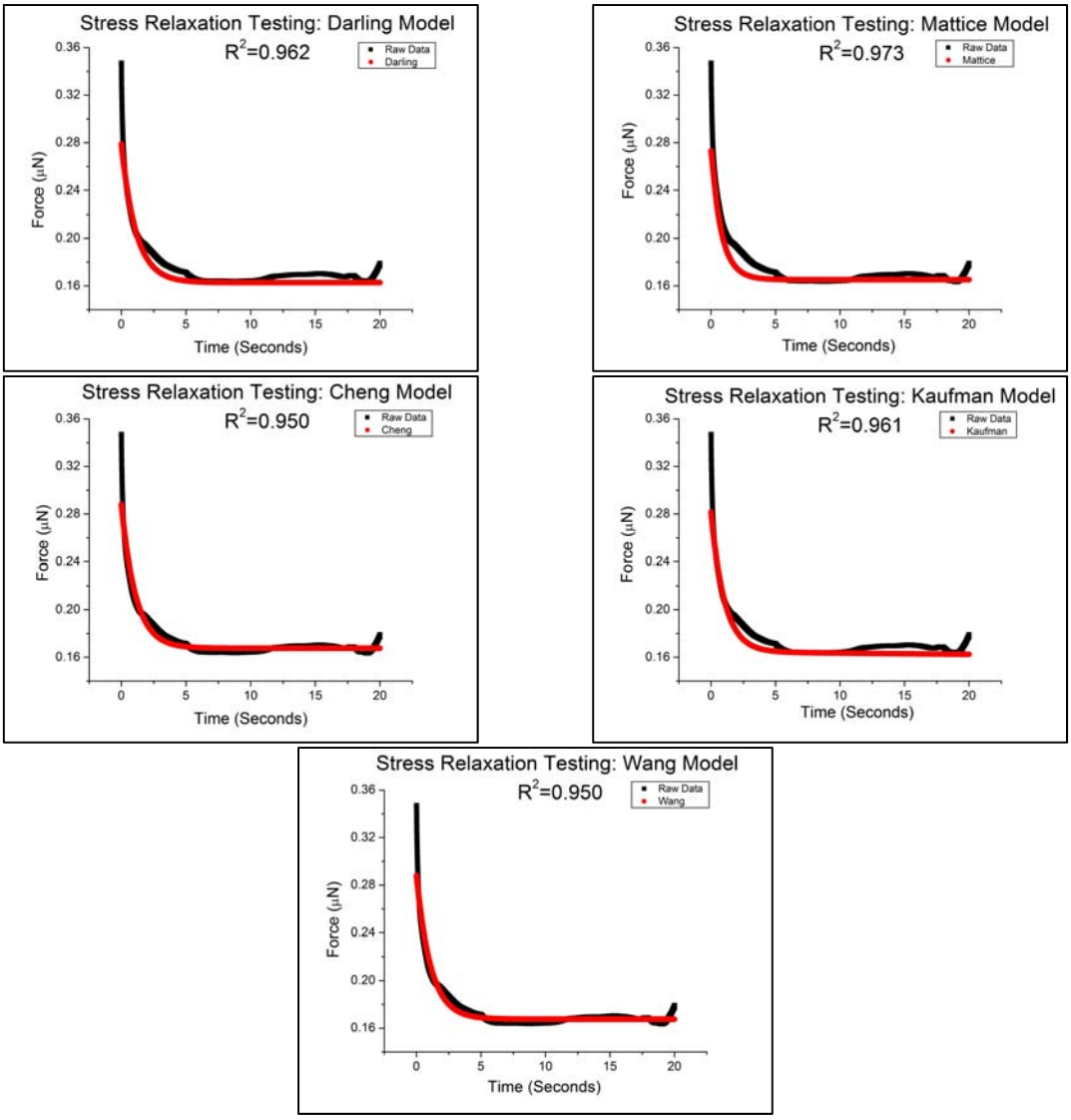

Figure 5.12: Curve Fits of the Darling, Mattice, Cheng, Kaufman, and Wang Stress Relaxation Models with Sample Corneal Mechanical Data.

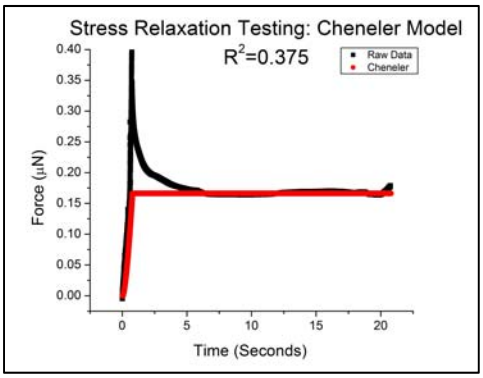

Figure 5.13: Curve Fit of the Cheneler Stress Relaxation Model with Sample Corneal Mechanical Data.

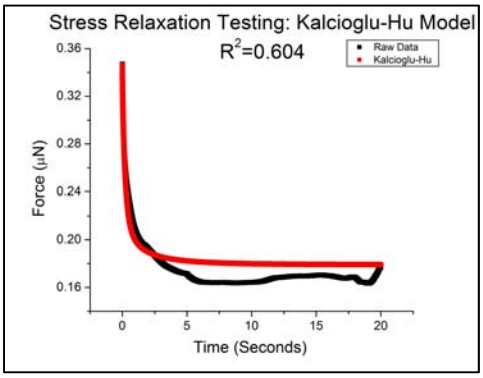

Figure 5.14: Curve Fit of the Kalcioglu-Hu Poroelastic Model with Sample Corneal Mechanical Data.

5.6 Summary

A comprehensive literature review of existing indentation-based contact mechanical models of elasticity, stress relaxation-based viscoelasticity, and stress relaxation-based poroelasticity was conducted. The elastic, viscoelastic, and poroelastic models obtained were then incorporated into custom MATLAB data analysis programs and used to fit representative corneal mechanical response data to determine their feasibility in describing corneal mechanical responses. It was determined that:

- The Hertz model most effectively described the corneal elastic mechanical response. Although multi-layered elastic models exist, the lack of their applicability for corneal stromal mechanical testing resulted in the decision to perform mechanical testing on the particular corneal layer of interest through direct application. Indentation performed on the cornea will be limited to 10% of the corneal layer's thickness to minimize effects of the underlying layers and substrate.

- The Darling model was most effective stress relaxation viscoelastic model in fitting the corneal stress relaxation response and producing a standard mechanical measure.
- The Kalcioglu-Hu model, which enables the derivation of poroelastic parameters from the stress relaxation response, is adequate in determining diffusivity but not shear modulus, Poisson's ratio of the solid matrix, or intrinsic permeability.

CHAPTER 6

CHARACTERIZATION OF CORNEAL BIOMECHANICAL PROPERTIES

6.1 Purpose

The goal of this chapter is to apply the developed AFM characterization capabilities, instrumentation, sample preparation methods, and biomechanical models to the porcine and human cornea. The efficacy of corneal crosslinking as a treatment method for keratoconus will be investigated using the aforementioned AFM techniques. Comparisons between the measured corneal elastic and stress relaxation response of the normal and cross-linked samples will be conducted. Finally, any age-dependence of any corneal mechanical property will be determined.

6.2 Crosslinking Protocols

6.2.1 Dresden

The standard corneal crosslinking procedure to combat the progression of keratoconus originated from Theo Seiler and researchers of Dresden, Germany. Using this protocol, a cotton-tipped applicator was used to detach the epithelium. Afterwards, 0.1% riboflavin solution (10 mg riboflavin-5-phosphate in 10 mL Dextran 20% solution) was applied onto the corneal surface one drop every 5 minutes for 30 minutes. This pretreatment enables the riboflavin, which is the photosensitizing agent, to permeate through to the corneal stromal region. The cornea is then irradiated using ultraviolet-A (UVA) light at 378 nm wavelength and with an intensity of $3mW/cm^2$. This irradiance is performed for 30 minutes, corresponding to a total surface dose of $5.4\ J/cm^2$. During

UVA irradiation, riboflavin solution is then applied every 5 minutes to maintain corneal saturation with riboflavin, and thereby crosslinking formation. After treatment, the cornea is placed in 15% Dextran for 30 minutes to allow equilibrium to be reached.

6.2.2 Accelerated Crosslinking

Researchers have begun to investigate the efficacy of using different UVA irradiance-exposure time combinations, while still maintaining the original energy dose of the standard protocol (5.4J/cm^2). One accelerated protocol incorporated in such studies is the 30mW/cm^2-3minute combination (Touboul *et al.* 2012, Mastropasqua *et al.* 2014, Mita *et al.* 2014, Tomita *et al.* 2014). This protocol was incorporated in this study. Like the Dresden protocol, this accelerated crosslinking protocol first consists of corneal epithelium removal and the 30-mintue pretreatment of 0.1% riboflavin. The accelerated crosslinking protocol reduces the UVA irradiation treatment time to 3 minutes at a UVA intensity of 30mW/cm^2. After treatment, the cornea is placed in 15% Dextran for 30 minutes to allow equilibrium to be reached.

6.2.3 Genipin

A promising alternative to the UVA crosslinking methods described previously is the use of genipin. Genipin is a natural chemical crosslinker, derived from the *Gardenia jazminoides* plant. Research has been conducted by Dr. Marcel Avila showing the effectiveness of genipin in increasing corneal mechanical strength (Avila and Navia 2010, Avila *et al.* 2012). Therefore, collaboration with Dr. Avila was established to devise an experimental protocol for genipin corneal crosslinking. The developed protocol

encompasses removing the corneal epithelium with a cotton-tipped applicator and placing the cornea, concave up, in 1% genipin solution (1g genipin/100mL balanced salt solution) for a duration of 4 hours. The cornea is then placed in 15% Dextran (15g dextran/100mL phosphate buffered salt solution) overnight to allow crosslinking completion and equilibrium to be reached (Figure 6.2).

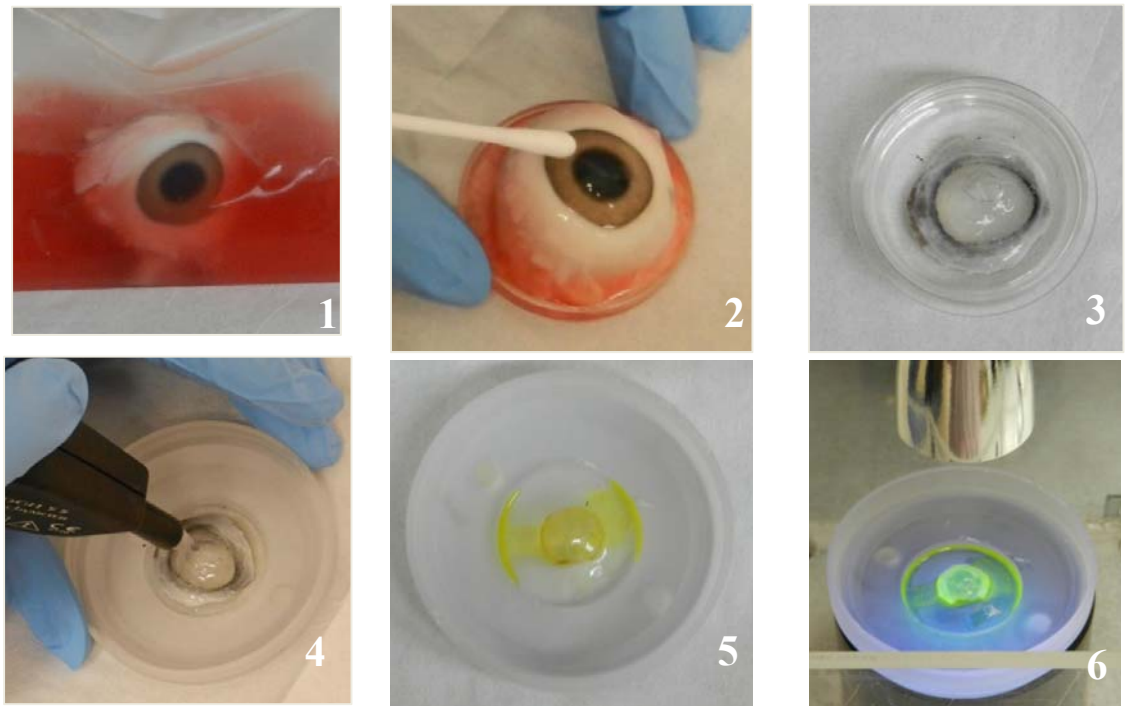

Figure 6.1: Dresden and Accelerated Corneal Crosslinking Methods: (1) Porcine eye globes are retrieved from a local abattoir. (2) Corneal epithelium is removed using a cotton-tipped applicator. (3) Cornea is placed in 20% Dextran to restore cornea to physiological thickness range. (4) Pachymetry measurements taken to ensure proper thickness restoration. (5) A 30-minute pretreatment of 0.1% riboflavin is performed. (6) Cornea is irradiated with UVA light (for Dresden, the irradiation time and intensity are: 30 minutes at $3mW/cm^2$; for the accelerated crosslinking, the irradiation time and intensity are: 3 minutes at $30mW/cm^2$. Afterward, the corneal thickness is measured and cornea is then placed in 15% Dextran for 30 minutes to allow crosslinking equilibrium to be reached.

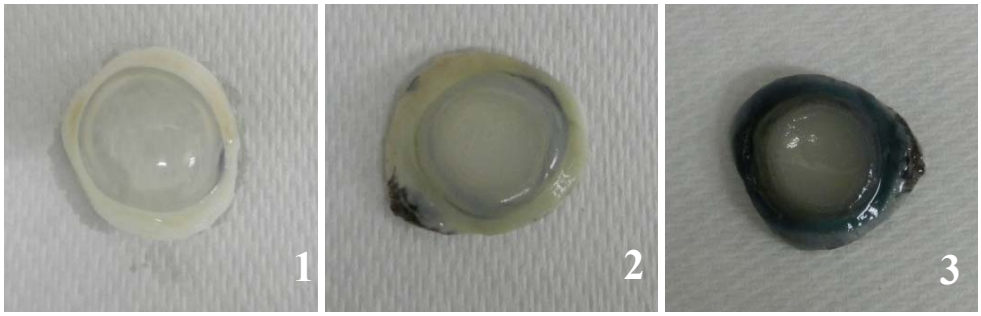

Figure 6.2: Genipin Corneal Crosslinking: (1) Porcine cornea untreated. (2) Porcine cornea post-4 hour treatment in 1% Genipin solution. (3) Porcine cornea after 24 hour equilibrium in 15% Dextran.

6.3 Porcine Corneal Study

6.3.1 Tissue Acquisition

The purpose of this study was to quantify the effect of the different crosslinking methods (Dresden, Accelerated crosslinking, and Genipin protocols) on corneal biomechanics at various stromal depths using the developed AFM instrumentation and techniques.

For this study, porcine eye globes were obtained from an abattoir. Upon receipt, the corneal epithelium was removed and the cornea was excised, leaving a generous scleral rim. The cornea was then placed in 20% Dextran overnight to restore the cornea to its physiological thickness range of 500 to 800μm (Faber *et al.* 2008). Pachymetry measurements were taken to ensure thickness restoration (DGH 55 Pachmate, DGH Technology Inc., Exton, PA).

A total of 40 porcine corneas were used in this study. Ten porcine corneas were then assigned to the respective experimental groups: control, Dresden, Accelerated crosslinking, and Genipin. Corneas within the control experimental group were subjected to no treatments, while corneas within the other experimental groups were subjected to

the experimental treatment protocols of Dresden, Accelerated crosslinking, and Genipin mentioned previously. After treatment, corneas within their respective experimental group were then evenly divided for mechanical testing at the anterior and middle stromal regions. Since the porcine cornea lacks Bowman's membrane, the superficial anterior stromal region was readily accessed after removing the corneal epithelium. For corneas reserved for middle anterior stromal mechanical testing, the middle stromal region was accessed using a Moria microkeratome system (LSK Evolution 2, Moria SA, Antony, FR) with a 200μm head (CBSU 200 Head, Moria-SA, Antony, FR). The corneal samples were then placed in a custom cornea holder with 15% Dextran solution to maintain corneal hydration during mechanical testing.

6.3.2 AFM Mechanical Testing

Mechanical property measurements were performed using the developed custom-built AFM system with elastic and viscoelastic characterization capability. Tip-less AFM cantilevers (nominal spring constant: 4.5 N/m, NSC12 series, Mikromasch, San Jose, CA) were modified with glass microspheres (59–74 μm diameter, 15926-100, Polysciences Inc). The modified tip was then calibrated to determine its spring constant using a reference force calibration cantilever (nominal spring constant: 10.4N/m, CLFC-NOBO, Bruker, Camarillo, CA) manufactured specifically for the calibration of other probes (calibrated modified tip spring constant: 29.8N/m). The modified cantilever tips were lowered onto the corneal samples using a piezoelectric mechanism (60μm maximal expansion, P-841.40, Physik Instrumente, Germany) with an approach speed of 15μm/s. For elasticity testing, a maximal indentation force of 1000mV (<20 nN, which

corresponds to <6μm indentation) was applied by the cantilever onto the cornea and then was immediately retracted at the same speed of 15μm/s. For stress-relaxation testing, the same indentation force of 1000mV was applied onto the cornea and remained at that indentation depth for a minimum stress hold time of 10 seconds. In both testing scenarios, the voltage detected at the photodiode due to deflection of the cantilever was recorded as a function of time. After factoring out the cantilever deflection on a hard surface and incorporating the measured spring constant, these recordings were used to derive the sample's force-indentation curves for elasticity testing and the sample's force response over time for viscoelasticity testing. With the use of custom MATLAB programs, the indentation force-indentation depth curves were analyzed using the Hertz model for a spherical indenter and the stress relaxation force response curves were analyzed using the Darling viscoelastic and Kalcioglu-Hu poroelastic models mentioned in the previous chapter.

6.3.3 Results

6.3.3.1 Thickness

The average central corneal thickness for all the eyes at the start of the experiments was 662.8 ± 30.7μm (range: 600-705 μm). For the porcine corneas subjected to middle anterior stromal mechanical testing, the average amount of stroma removed using the 200μm microkeratome head was 222.2 ± 41.3μm (range: 141-284 μm). For each crosslinking experimental group, the percentage change of corneal thickness (change in thickness relative to initial thickness) before and after treatment was calculated for each sample (Figure 6.3). The percentage change in thickness was: -11.8 ±

4.3% for the accelerated protocol, -15.4 ± 4.2% for Dresden, and 32.1 ± 11.2% for genipin (Figure 6.4). A paired Student's t-test was performed to compare the initial and final corneal thickness measurements for each crosslinking group. Such tests resulted in statistical significance for all the crosslinking groups ($p<0.05$).

6.3.3.2 Elasticity

The average effective Young's modulus for each experimental group at the superficial anterior stromal region was: 0.595 ± 0.584 MPa for the control, 0.858 ± 0.462MPa for the accelerated protocol, 1.82 ± 1.03MPa for Dresden, and 1.70 ± 0.512MPa for genipin (Figure 6.5). The factors of increase produced by the accelerated, Dresden, and genipin treatments were 0.50, 1.84, and 2.86, respectively, in relation to the control. For the middle anterior stromal region, the average effective Young's modulus was: 49.4 ± 4.9kPa for the control, 76.6 ± 43.6kPa for the accelerated protocol, 82.6 ± 44.9kPa for Dresden, and 56.3 ± 14.8kPa for genipin (Figure 6.5). The factors of increase for the accelerated, Dresden, and genipin treatments were 1.03, 1.36, and 0.24, respectively.

Unpaired Student's t-tests were performed to compare the effective Young's moduli of each crosslinking group with the control group for the superficial and middle anterior stromal regions, respectively. At the superficial anterior stromal level, the Dresden and genipin crosslinking treatments proved statistically significant from the control ($p<0.05$) while the accelerated protocol was comparable ($p=0.23$). However, at the middle anterior stromal region, all of the crosslinking groups deemed comparable to the control ($p=0.12$ for accelerated, $p=0.09$ for Dresden, and $p=0.19$ for genipin).

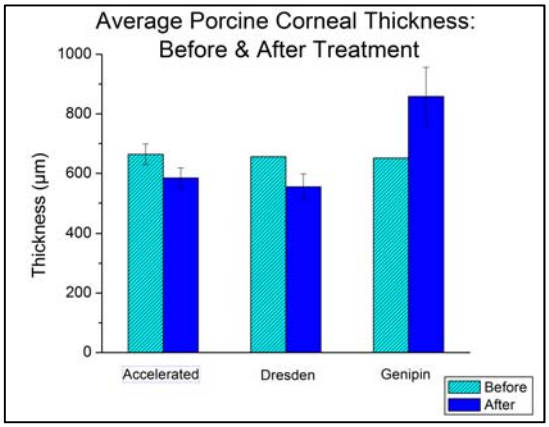

Figure 6.3: Average Porcine Corneal Thickness Before and After the Accelerated, Dresden, and Genipin Crosslinking Treatments.

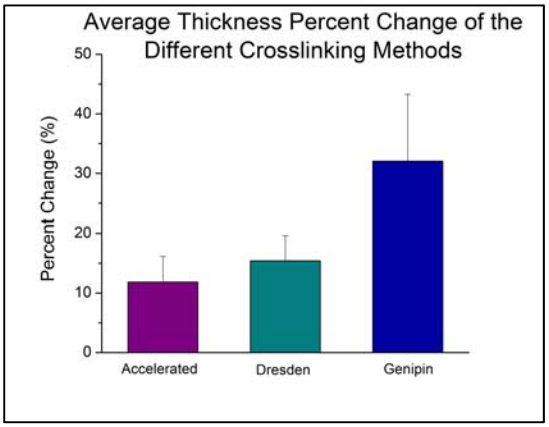

Figure 6.4: Average Thickness Percentage Change Produced by the Crosslinking Treatments.

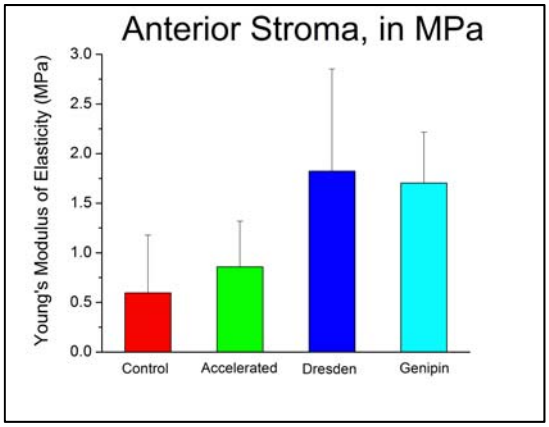

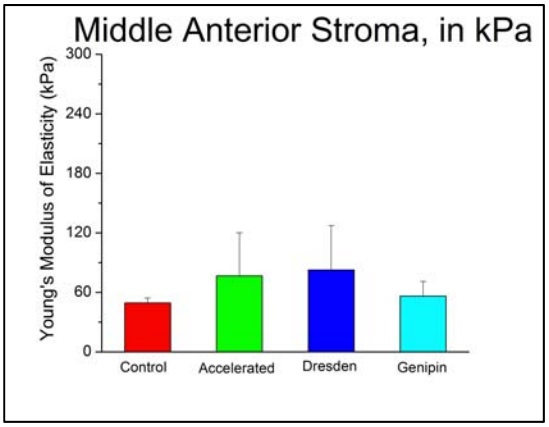

Figure 6.5: Bar Graphs of the Measured Corneal Young's Moduli for the Experimental Groups. *Left*, Superficial Anterior Stromal Region. *Right*, Middle Anterior Stromal Region.

6.3.3.3 Viscoelasticity

Using the Darling model, the apparent viscosity (Eq. 5.60) of each corneal sample was calculated. The average calculated apparent viscosity for each experimental group at the superficial anterior stromal region was: 64.1 ± 61.2kPa-s for the control, 6.3 ± 3.3kPa-s for the accelerated protocol, 2.4 ± 2.4kPa-s for Dresden, and 11.6 ± 5.3kPa-s for genipin (Figure 6.6). The factors of decrease in apparent viscosity for each crosslinking

group, compared to the control were: 0.08 for the accelerated protocol, 0.04 for the Dresden protocol, and 0.35 for the genipin protocol. For the middle anterior stromal region, the average calculated apparent viscosity was: 20.9 ± 22.2kPa-s for the control, 18.4 ± 23.6kPa-s for the accelerated protocol, 21.5 ± 19.1kPa-s for Dresden, and 27.6 ± 19.5kPa-s for genipin (Figure 6.7). The factors of increase in this stromal region were: 3.06 for the accelerated protocol, 1.03 for the Dresden protocol, and 1.32 for the genipin protocol.

Unpaired Student's t-tests were performed to compare calculated apparent viscosities of each crosslinking group with the control group for both superficial and middle anterior stromal regions. At the superficial anterior stromal level, the apparent viscosities of corneas treated with the accelerated and Dresden crosslinking treatments were statistically different than those within the control group ($p=0.049$ for the accelerated and $p=0.044$ for Dresden). The apparent viscosities of the corneas within the genipin treatment group were comparable to those of the control group ($p=0.11$). The three crosslinking groups were comparable to the control at the middle anterior stromal region ($p=0.08$ for accelerated, $p=0.48$ for Dresden, and $p=0.32$ for genipin).

6.3.3.4 Poroelasticity

The poroelastic parameter of diffusivity (Eq. 5.137) was derived for each cornea using the Kalcioglu-Hu model. The average diffusivity values derived for each experiment group at the superficial anterior stromal level were: 0.05 ± 0.03 ($x10^{-9}$) m^2/s for the control, 0.18 ± 0.2 ($x10^{-9}$)m^2/s for the accelerated protocol, 0.13 ± 0.1 ($x10^{-9}$)m^2/s for Dresden, and 0.14 ± 0.1 ($x10^{-9}$)m^2/s for genipin (Figure 6.8). The factors of increase

in diffusivity, compared to the control, at the superficial anterior were: 3.6 for the accelerated protocol, 2.6 for Dresden, and 2.8 for genipin. Within the middle stromal region, the average diffusivity values derived for each experiment group were: 0.17 ± 0.07 ($x10^{-9}$)m^2/s for the control, 0.16 ± 0.10 ($x10^{-9}$)m^2/s for the accelerated protocol, 0.28 ± 0.2 ($x10^{-9}$)m^2/s for Dresden, and 0.02 ± 0.1 ($x10^{-9}$)m^2/s for genipin (Figure 6.8). At the middle anterior stroma, the factors of decrease for the accelerated and genipin treatments were 0.91 and 0.11, while the factor of increase for Dresden was 1.66.

Unpaired Student's t-tests were performed to compare calculated shear moduli and diffusivity values of each crosslinking group with the control group for both superficial and middle anterior stromal regions. For both superficial and middle anterior stromal regions, the diffusivity values for the corneas within the crosslinking groups were comparable to those of the control group ($p>0.05$) with the exception of genipin at the middle stromal region ($p=0.03$).

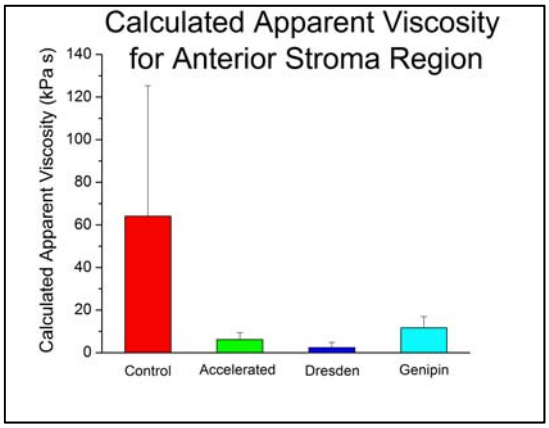

Figure 6.6: Bar Graph of the Calculated Apparent Viscosities Measured in the Superficial Anterior Stromal Region for the Experimental Groups.

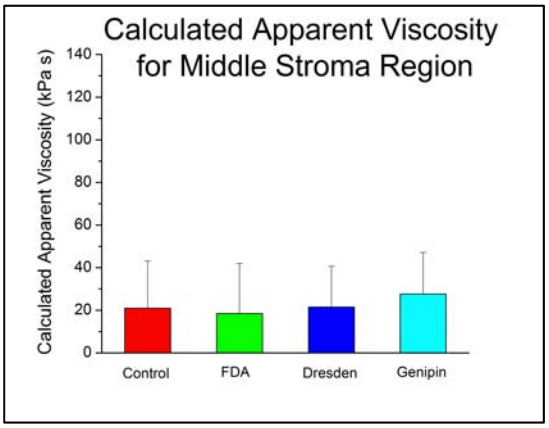

Figure 6.7: Bar Graph of the Calculated Apparent Viscosities Measured in the Middle Anterior Stromal Region for the Experimental Groups.

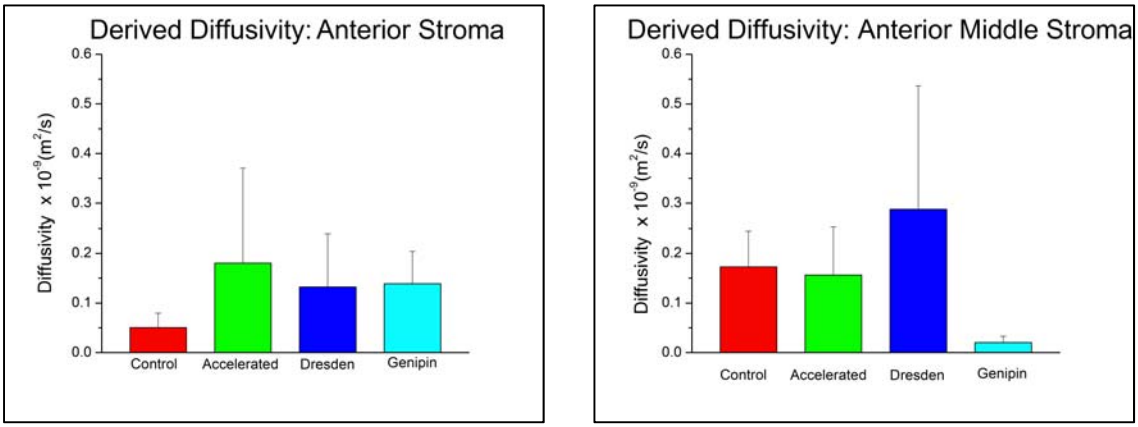

Figure 6.8: Bar Graphs of the Derived Diffusivity for each Experimental Group. *Left*, Superficial Anterior Stromal Region. *Right*, Anterior Middle Stromal Region.

	Sample Size (n)	ELASTIC Young's Modulus (MPa)	VISCOELASTIC Apparent Viscosity (kPa-s)	POROELASTIC Diffusivity ($x10^{-9}$ m^2/s)
Control	5	0.595 ± 0.584	64.1 ± 61.2	0.05 ± 0.03
Accelerated	5	0.858 ± 0.462	6.3 ± 3.3 *	0.18 ± 0.20
Dresden	5	1.82 ± 1.03 *	2.4 ± 2.4 *	0.13 ± 0.10
Genipin	5	1.70 ± 0.512 *	11.6 ± 5.3	0.14 ± 0.10

Table 6.1: Summary Table of Porcine Corneal Elastic, Viscoelastic, and Poroelastic Properties at the Superficial Anterior Stroma Level for all Experimental Groups (* Means Statistically Significant).

	Sample Size (n)	ELASTIC Young's Modulus (kPa)	VISCOELASTIC Apparent Viscosity (kPa-s)	POROELASTIC Diffusivity ($x10^{-9}$ m^2/s)
Control	5	49.4 ± 4.9	20.9 ± 22.2	0.17 ± 0.90
Accelerated	5	76.6 ± 43.6	18.4 ± 23.6	0.16 ± 0.10
Dresden	5	82.6 ± 44.9	21.5 ± 19.1	0.28 ± 0.20
Genipin	5	56.3 ± 14.8	27.6 ± 19.5	0.02 ± 0.10 *

Table 6.2: Summary Table of Porcine Corneal Elastic, Viscoelastic, and Poroelastic Properties at the Middle Anterior Stroma Level for all Experimental Groups (* Means Statistically Significant).

6.3.4 Discussion

6.3.4.1 Elasticity

Results of this study revealed that the Dresden and genipin crosslinking treatments were most effective in increasing corneal stiffness within the superficial anterior stromal region, with statistical significance. The increase in corneal elasticity for the Dresden and genipin treatments correspond to the increase of mechanical stiffness of collagen fibers as well as the increase crosslink formation between collagen fibers within this region. However, the accelerated crosslinking protocol did not produce any effect on the corneal elasticity compared to the control.

At the middle anterior stromal region, none of the treatments produced the significant changes in corneal elasticity. This signifies that the stiffness and crosslink formation of the collagen fibers at this region remained unchanged. This can be attributed to factors including the limited diffusion of the riboflavin and genipin solutions into the deeper stromal regions as well as the limited exposure of these deeper stromal regions to UV irradiation due to the Beer-Lambert Law, which describes light attenuation as an exponential decrease with increasing distances.

Overall, these corneal elasticity results revealed that the stiffening effect of the genipin and Dresden crosslinking treatments appear to be depth-dependent, with the majority taking place in the superficial anterior region and less in the middle stromal regions. The outcome seen for Dresden crosslinking treatment in this study confirms the findings of Kohlhaas *et al* (2006), Dias and Ziebarth (2003), and Sondergaard *et al* (2013), who also observed such depth-dependence.

With regards to the corneal control experimental groups at the superficial and middle anterior stromal regions, the corneal elasticity was statistically comparable between the two regions (p=0.14). Such result was also observed in the study of Kohlhaas *et al* (2006). This observation is believed to be correlated to the stromal organization of the porcine corneal model, which is highly organized and consistent through its stromal depth, compared to the varied stromal organization of the human cornea.

6.3.4.2 Viscosity

Viscosity represents the resistance of a material to fluid flow within its microstructure. Therefore, it is hypothesized that the viscous properties of the cornea correspond to the nature of the proteoglycan-keratocyte content within the stroma. Within the superficial anterior stromal region, the crosslinking treatments produced notable decreases in corneal viscosity compared to the control corneas, with Dresden and the accelerated crosslinking obtaining statistical significance. Such decrease observed corresponds to probable modification to the proteoglycan-keratocyte content within the stroma. The study of Zhang *et al* (2011) demonstrated that riboflavin-UVA crosslinking yielded not only crosslinking between the collagen fibers but also crosslinking between the proteoglycan content (Zhang *et al*. 2011). Future studies should be conducted to obtain further insight regarding the effect of the crosslinking treatments on the stromal proteoglycan-keratocyte content as well as to establish a correlation between the viscosity parameter and the corneal structure, particularly related to the proteoglycan-keratocyte matrix.

With regards to the middle stromal regions, none of the crosslinking treatments produced statistically significant differences in corneal viscosity, compared to the control group. These results reveal that the proteoglycan-keratocyte content within the deeper stromal regions remain unaffected by the crosslinking treatments.

Overall, the trends observed with regards to corneal elasticity and viscosity imply that the crosslinking treatments are producing a stiffer and less viscoelastic corneal nature.

6.3.4.3 Diffusivity

The diffusivity parameter describes the ability of a solute and fluid to diffuse through a porous material. Therefore, within the context of the cornea, diffusivity gives insight into the ability of solutes and fluid to traverse through the collagenous fiber networks in the stroma, hence describing the cornea's transport properties. In the superficial anterior and middle anterior stromal regions, no treatments produced statistically significant changes in corneal diffusivity with the exception of the genipin at the middle anterior stromal regions. For genipin, a significant decrease in corneal diffusivity was observed, which signifies that solute and fluid movement in this region decreased compared to the control. More experiments will be conducted to determine if this trend exists, as probable reason for this observance is currently unknown.

6.4 Human Corneal Study

6.4.1 Tissue Acquisition

The purpose of this study was to quantify the effect of the Dresden crosslinking method on human corneal biomechanics at the anterior stromal depth using the developed AFM instrumentation and techniques.

Experiments were conducted on 10 pairs of human cadaver corneas (age range: 22-90 years). Corneal samples were retrieved from the Florida Lions Eye Bank (Miami, FL) in two forms: corneas attached to the eye globe and corneas already excised from the eye globe with a generous scleral rim. Retrieved human eye globes (n=3 pairs) arrived from the eye bank in sealed vials placed in Styrofoam containers filled with ice. Upon arrival in the laboratory, the corneal epithelium was removed using a cotton-tipped applicator and the cornea was excised from the eye globe, leaving a generous scleral rim. The corneas were then placed in 20% Dextran solution for 24 hours and stored in the refrigerator at 4 °C to restore corneal thickness to physiological levels. The mean postmortem time of the eyes at the time of receipt was 5.5±1.5 days (range: 6–8 days), but the actual experiments were performed 24 hours later to enable this initial pretreatment with 20% Dextran. Pachymetry measurements were taken after pretreatment (DGH 55 Pachmate, DGH Technology Inc., Exton, PA) to ensure the restoration of the corneal thickness within the physiological range of 400-600μm.

The retrieved corneal pairs (n=7 pairs), already excised from the eye globe with a generous scleral rim, were originally reserved for corneal transplantation surgery but were no longer selected for such purposes once reaching the eye bank. Since prepared for corneal transplantation, the corneas were received from the eye bank in sealed vials filled

with Optisol solution to preserve the life and integrity of the corneal epithelium. Upon arrival at the laboratory, these corneas were placed in the refrigerator at 4°C until the day of experimental testing. The mean postmortem time of these corneas at the time of receipt was 22.9±8.5 days (range: 8-35 days). On the day of experimental testing, the corneal epithelium was removed using a cotton-tipped applicator and pachymetry measurements were taken. If the measured corneal thickness was out of the normal physiological range of 400-600μm (n=4 pairs), the cornea was then placed in 20% Dextran until its thickness reached the acceptable range. All human corneas were obtained and used in compliance with the guidelines of the Declaration of Helsinki for research involving the use of human tissue.

6.4.2 Corneal Crosslinking Treatment

For this study, the right eyes (OD) served as the untreated controls (with no riboflavin pretreatment) and the left eyes (OS) were treated using the standard CXL Dresden protocol (Figure 6.1). A Moria microkeratome (LSK Evolution 2, Moria SA, Antony, FR) with a disposable 50μm microkeratome head (CBSU 50 Head, Moria-SA, Antony, FR) was used to remove approximately 50μm of corneal tissue from the intact cornea, thereby removing Bowman's membrane (17.7μm thickness; (Tao *et al.* 2011)) to expose the anterior stromal region, but leaving it connected to the remaining stromal layer and Descemet's membrane. The corneal samples were then placed in a custom cornea holder with 15% Dextran solution to maintain corneal hydration during mechanical testing.

6.4.3 AFM Mechanical Testing

Mechanical property measurements were performed using a custom-built atomic force microscopy (AFM) system. The AFM system and experimental procedure have been described in detail previously (Ziebarth *et al.* 2010, Dias *et al.* 2013). Briefly, tip-less AFM cantilevers (nominal spring constant: 1.0 N/m, NSC36 series, Mikromasch, San Jose, CA) were modified with glass microspheres (59–74 μm diameter, 15926-100, Polysciences Inc). The modified tip was then calibrated to determine its spring constant using a reference force calibration cantilever (nominal spring constant: 10.4 N/m, CLFC-NOBO, Bruker, Camarillo, CA) manufactured specifically for the calibration of other probes (calibrated modified tip spring constant range: 2-19.8N/m). The modified cantilever tips were lowered onto the corneal samples using a piezoelectric mechanism (60μm maximal expansion, P-841.40, Physik Instrumente, Germany) with an approach speed of 15μm/s. For elasticity testing, a maximal indentation force of 1000mV (<20 nN, which corresponds to <6μm indentation) was applied by the cantilever onto the cornea and then was immediately retracted at the same speed of 15μm/s. For stress-relaxation testing, the same indentation force of 1000mV, was applied onto the cornea and remained at that indentation depth for a stress hold time of 10-20 seconds. In both testing scenarios, the voltage detected at the photodiode due to deflection of the cantilever was recorded as a function of time. After factoring out the cantilever deflection on a hard surface and incorporating the measured spring constant, these recordings were used to derive the sample's force-indentation curves for elasticity testing and the sample's force response over time for viscoelasticity testing. With the use of custom MATLAB programs, the indentation force-indentation depth curves were analyzed using the Hertz model for a

spherical indenter and the stress relaxation force response curves were analyzed using the Darling viscoelastic and Kalcioglu-Hu poroelastic models mentioned in the previous chapter.

6.4.4 Results

6.4.4.1 Thickness

The mean central corneal thickness of all eyes was 479.2 ± 52.4μm (range: 410-585μm) after epithelial removal and 20% dextran pretreatment; while the average stromal depth cut produced by the 50μm microkeratome head was 64.5 ± 32.1μm (range: 25-139μm). For the Dresden crosslinking experimental group, the percentage change of corneal thickness (change in thickness relative to initial thickness) before and after treatment was calculated for each cornea (Figure 6.9). The average percentage change in thickness was: -26.1 ± 8.9%. A paired Student's t-test was performed to compare the initial and final corneal thickness measurements for the crosslinked corneal group, which resulted in statistical significance ($p<0.05$).

6.4.4.2 Elasticity

The mean Young's modulus of elasticity within the anterior stromal region was 219.9 ± 204.3kPa (range: 10.3 – 544.2kPa) for the untreated control eyes and 425.8 ± 445.1kPa for the Dresden treatment group (Figure 6.10). A paired Student's t-test was performed to compare the Young's moduli of Dresden group with the control group. Although a majority increase in corneal elasticity was observed among the eye pairs, the

Young's moduli of the crosslinked corneas were not statistically significant to those left untreated (p=0.10).

To determine age-related dependency, the corneal elasticity results of the Dias *et al* (2013) were also incorporated. The Young's moduli of both the control (OD) and crosslinked (OS) corneas were plotted as a function of age, for the anterior and posterior stromal regions (Figure 6.11). For the anterior stromal region, an overall increasing trend in corneal elasticity with age was observed for the control and crosslinked corneas, although not statistically significant. For the posterior stromal region, no apparent age-related trend was observed for the corneal elasticity of the control and crosslinked corneas. In addition, the factors of increase in corneal elasticity between the crosslinked and control corneas were also plotted with age for the anterior and posterior stromal regions, respectively (Figure 6.12). There appeared to be a decreasing trend for the anterior stromal region, although not significant, and a uniform trend for the posterior stromal region. The average factors of increase at the anterior and posterior stromal regions were 2.3± 2.1 and 1.0±0.7, respectively.

6.4.4.3 Viscoelasticity

The average calculated apparent viscosities for control and Dresden experimental groups was 3.45 ± 3.62kPa-s (range: 0.22 – 9.74kPa-s) and 3.38 ± 3.59kPa-s (range: 0.33 – 8.79kPa-s), respectively (Figure 6.13). A paired Student's t-test showed that the apparent viscosities of the crosslinked corneas were comparable to their control counterparts (p=0.48). This was further evidenced when the control and crosslinked

apparent viscosities were plotted as function of age (Figure 6.14). Age-related trends for the apparent viscosities of the control and crosslinked corneas remain inconclusive.

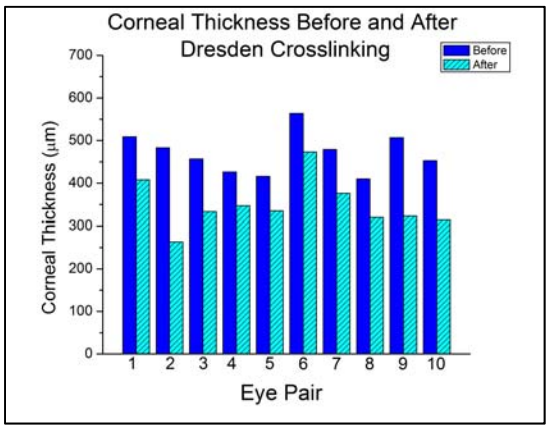

Figure 6.9: Bar Graph of the Corneal Thickness Before and After the Dresden Crosslinking Procedure

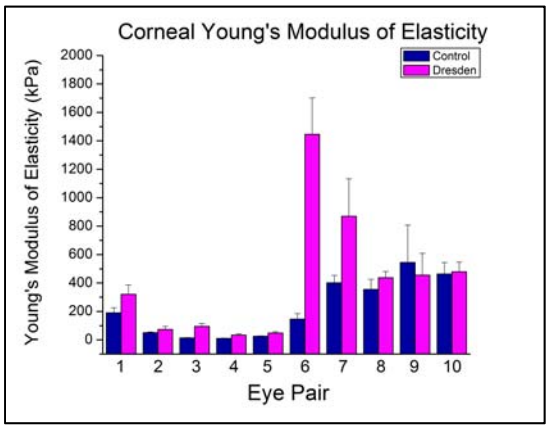

Figure 6.10: Bar Graph of the Control and Dresden Corneal Young's Modulus for each Eye Pair.

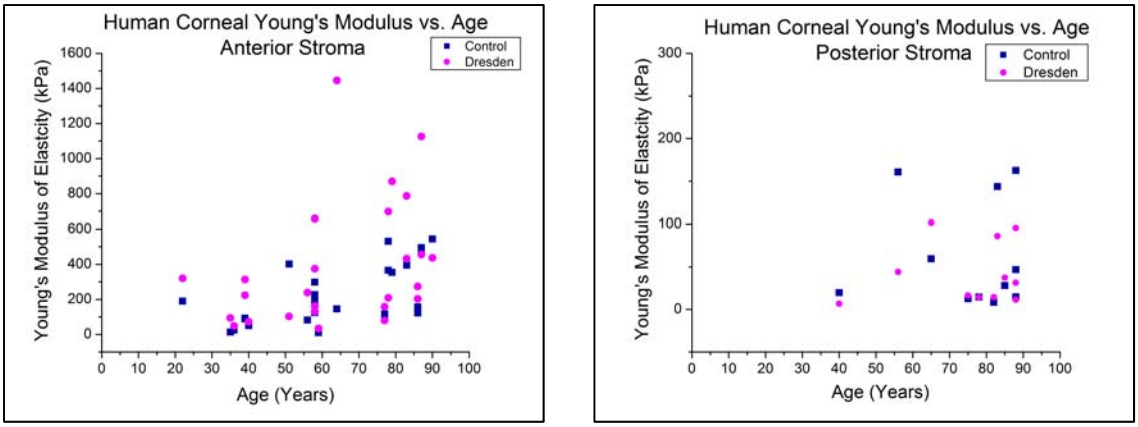

Figure 6.11: The Control and Dresden Corneal Young's Modulus vs Age for the Anterior Stroma, *Left*, and the Posterior Stroma, *Right*.

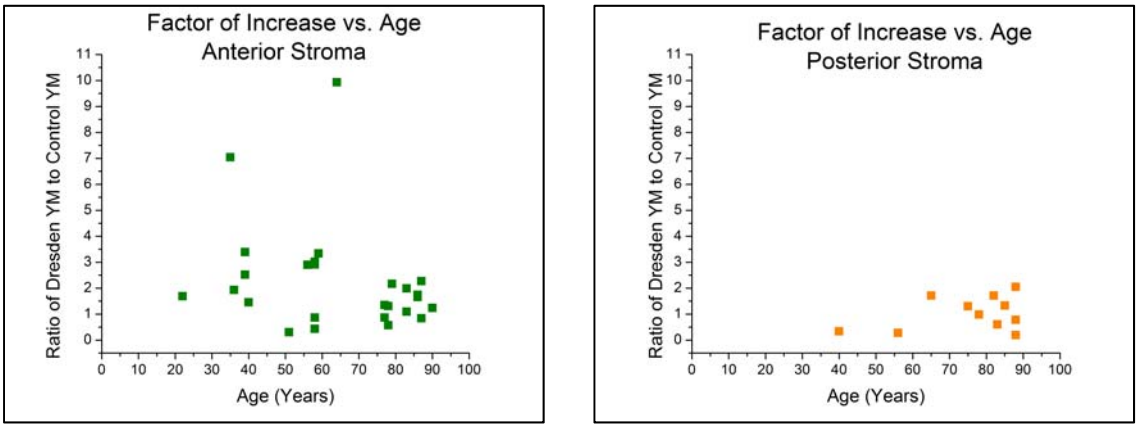

Figure 6.12: Plot of Factor of Increase vs Age for the Anterior Stroma, *Left*, and the Posterior Stroma, *Right*.

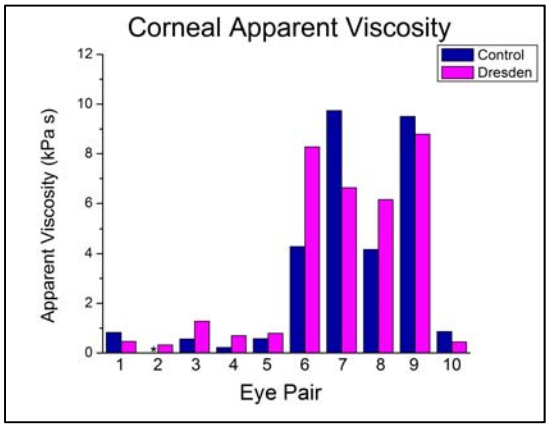

Figure 6.13: Bar Graph of the Control and Dresden Corneal Apparent Viscosity for each Eye Pair.

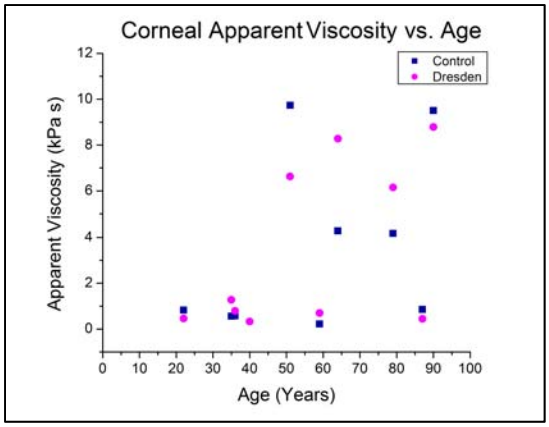

Figure 6.14: Plot of Control and Dresden Corneal Apparent Viscosity vs Age.

6.4.4.4 Poroelasticity

The average diffusivity for the control group was 0.309 ± 0.209 ($x10^{-9}$) m^2/s (range: 0.04- 0.675($x10^{-9}$) m^2/s) and that of the Dresden group was 0.437 ± 0.268 ($x10^{-9}$)m^2/s (range: 0.10- 0.851($x10^{-9}$) m^2/s), being comparable with one another (p=0.14) (Figure 6.15). In addition, there were no statistically significant observances of any distinct age-dependent trends for both groups' corneal diffusivities (Figure 6.16).

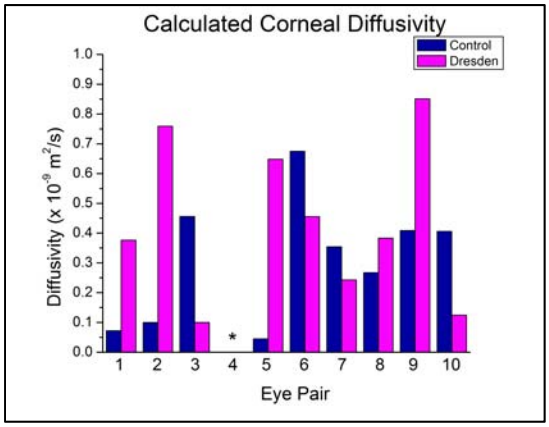

Figure 6.15: Bar Graph of the Calculated Diffusivity for the Control and Dresden Groups. The asterisk sign (*) shown for Eye Pair 4 indicates that the diffusivity could be obtained.

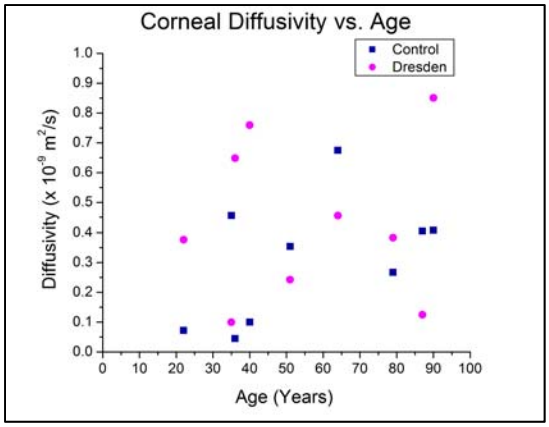

Figure 6.16: Plot of Control and Dresden Corneal Diffusivity vs. Age.

	Sample Size (n)	ELASTIC	VISCOELASTIC	POROELASTIC
		Young's Modulus (kPa)	Apparent Viscosity (kPa-s)	Diffusivity ($x10^{-9}m^2/s$)
Control	5	57.8 ± 75.4	0.545 ± 0.24	0.168 ± 0.19
Dresden	5	114.1 ± 117.4	0.711 ± 0.37	0.471 ± 0.29

Table 6.3: Summary Table of Corneal Elastic, Viscoelastic, and Poroelastic Properties for the Control and Dresden Corneal Groups

6.4.5 Discussion

6.4.5.1 Elasticity

In this study, Young's modulus of elasticity increased in the majority of the samples due to the Dresden crosslinking treatment (Figure 6.10). Such increase in corneal stiffness can be attributed to the increase in mechanical stiffness of the corneal collagen fibers as well as the increase in crosslink formation between the collagen fibers. This outcome confirms the qualitative findings for the *ex vivo* human cornea seen in literature (Wollensak *et al.* 2003, Kohlhaas *et al.* 2006, Cartwright *et al.* 2012, Beshtawi *et al.* 2013, Choi *et al.* 2013, Dias *et al.* 2013, Sondergaard *et al.* 2013, Beshtawi *et al.* 2014, Lombardo *et al.* 2014). In addition, the average factor of increase for the anterior stromal

region lies within the range of 1.051 – 4.5 observed in literature (Wollensak *et al.* 2003, Kohlhaas *et al.* 2006, Cartwright *et al.* 2012, Beshtawi *et al.* 2013, Choi *et al.* 2013, Dias *et al.* 2013, Sondergaard *et al.* 2013, Beshtawi *et al.* 2014, Lombardo *et al.* 2014).

An increasing trend was observed when plotting corneal elasticity as a function of age at the anterior stromal region. This finding confirms the previous studies showing an increase in corneal stiffness with age (Malik *et al.* 1992, Daxer *et al.* 1998, Elsheikh *et al.* 2007, Kotecha 2007, Randleman *et al.* 2008, Ruberti *et al.* 2011, Cartwright *et al.* 2012). Nonetheless, the decreasing trend for the factor of increase in corneal elasticity with age, at the anterior stromal region, implies that the Dresden treatment is less effective in older patients. Therefore, the Dresden treatment should be targeting younger keratoconus patients. With regards to the posterior stromal region, a generally uniform trend was observed for corneal elasticity as function of age for both the control and crosslinked corneas. Such observations imply that the overall corneal mechanical strength is attributed to the anterior stromal region in normal corneas and that the Dresden treatment has no mechanical effect at deeper stromal regions.

6.4.5.2 Viscosity

Corneal viscosity provides insight into the nature of the proteoglycan-keratocyte content, whether it be more fluid-like (lower viscosity values) or gel-like (high viscosity values), within the corneal stroma ultrastructure. The findings of this study revealed no conclusive trend in corneal viscosity change due to the Dresden treatment at the anterior stromal region, as both increases and decreases in corneal viscosity were observed (Figure 6.13). Such results indicate that probable modification to the proteoglycan-

keratocyte content occurs due to crosslinking, although the precise effect is not known. In addition, no apparent age-related trends in corneal viscosity were observed for the control and crosslinked corneas. These inconclusive outcomes may imply that the effect of the Dresden treatment on the proteoglycan-keratocyte content is dependent on patient-specific factors such as genetics and possible health diseases. More experiments should be performed to determine if these trends persist.

6.4.5.3 Diffusivity

Corneal diffusivity reflects the ability of solutes and fluid to move throughout the corneal stromal ultrastructure. Similar to corneal viscosity, no apparent effect of the Dresden treatment on corneal diffusivity was demonstrated, thereby revealing that the crosslinking treatment does not significantly affect solute and fluid movement through the cornea's anterior stromal region. Such uninhibited solute-fluid transport is important for the facilitation of corneal healing processes after the crosslinking is performed.

6.5 Summary

The developed AFM techniques and the contact mechanical models for elasticity, viscoelasticity, and poroelasticity were applied to quantify the effect of the corneal crosslinking techniques on the porcine and human corneal mechanical properties. To accomplish such quantification, two studies were conducted. The first study comprised of the assessing the effects of the Dresden crosslinking treatment, an accelerated crosslinking technique, and genipin on porcine corneal mechanical properties at the superficial and middle anterior stromal depths. The latter study encompassed quantifying

the effect of the Dresden crosslinking treatment on human corneal mechanical properties at the anterior stromal region. Age-dependency trends were then determined.

The porcine study revealed that the effect of the crosslinking treatments on porcine stromal mechanical properties were depth-dependent, with the majority of mechanical effects taking place in the superficial anterior stromal region. In this region, the crosslinking treatments produced an overall increase in corneal elasticity and decrease in corneal viscosity. Such results indicate that the crosslinking treatments are causing the porcine anterior stroma to become stiffer and less viscoelastic in nature. At the middle anterior stromal region, the crosslinking techniques produced no changes in corneal elasticity and viscosity and possible modification in corneal solute transport.

The human corneal study showed that the Dresden crosslinking treatment produced an increase in corneal elasticity but varied effects for corneal viscosity and diffusivity, compared to the control corneal group. Age-related trends were observed for corneal elasticity, demonstrating that, although the Dresden treatment improves corneal mechanical strength, its efficacy is limited to younger patient populations rather than older patient populations.

The developed AFM instrumentation and techniques were successfully implemented to perform a full mechanical characterization of the corneal model.

CHAPTER 7

SUMMARY

The goal of this project was to develop techniques and instrumentation to characterize *ex vivo* corneal biomechanical response using atomic force microscopy (AFM). Proving insight regarding the relationship between corneal structure and physiological function, corneal biomechanics has become a relevant field for understanding corneal pathologies and providing a quantitative measure in effective treatment development for such diseases. The ability to understand corneal biomechanics requires knowledge of corneal elasticity and viscoelasticity. Therefore, this project focused on using atomic force microscopy as a suitable characterization technique to measure corneal elasticity and viscoelasticity, in near-physiological experimental settings. A custom-built AFM system capable of nanoscale elastic characterization of the lens was previously developed by Dr. Noel Ziebarth. To enable full corneal mechanical characterization capability, techniques were developed to probe the cornea at the tissue-level and the existing AFM system's capability was extended for viscoelastic characterization testing.

Methods were developed to obtain accurate tissue-level measurements of the corneal biomechanical response. To perform AFM mechanical testing of the *ex vivo* cornea in a near-physiological environment, a custom corneal holder was developed. This holder allows for the minimization of corneal sample manipulation as well as the preservation of corneal integrity by maintaining the curvature and hydration of an intact *ex vivo* cornea during mechanical testing. The flexibility of atomic force microscopy to measure mechanical properties at different length scales stems from the geometrical

profile of the AFM cantilever used. Conical and pyramidal-shaped cantilevers are commonly used to measure cellular and individual tissue components at the nanoscale level; however, to probe the cornea at the tissue-level, specifically the networks of collagen fibers, spherical AFM cantilevers were needed. As a result, the modification of tipless AFM cantilevers with spherical microbeads and their corresponding calibration was conducted. Since corneal hydration significantly influences the accuracy of the mechanical properties obtained, a study was also conducted to determine the best hydration media that would maintain corneal hydration. Results of this study showed that 15% Dextran was most effective in stabilizing and maintaining corneal thickness, so this hydration medium was used during AFM mechanical testing.

With these developed AFM techniques, corneal elastic characterization using the AFM system was successfully performed. The system's capability was then expanded to conduct corneal viscoelastic characterization by incorporating AFM stress relaxation testing. Custom code was incorporated into the AFM control software to allow stress relaxation testing. The viscoelastic stress relaxation capability of the custom system was validated by comparing relaxation responses of a material exhibiting no viscoelasticity with that of the viscoelastic cornea. Results of the validation demonstrated that a non-viscous material produced no relaxation while the response of the viscoelastic cornea was of the expected exponential profile.

With this new viscoelastic ability, contact mechanical models were then needed to translate the measured responses into standard mechanical parameters. A comprehensive literature review of indentation-based contact mechanical models was conducted in attempts to describe the corneal elastic and stress relaxation response. Elastic,

viscoelastic, and poroelastic models were assessed to determine their applicability to corneal biomechanical responses by performing model fits to sample corneal data and determining the goodness of model fit. The Hertz, Darling, and Kalcioglu-Hu models deemed effective in describing the respective elastic, viscoelastic, and poroelastic properties of the cornea. These models provided the respective output parameters of Young's modulus of elasticity, apparent viscosity, and diffusivity. The Young's modulus of elasticity corresponds to the mechanical stiffness of and crosslink formation between collagen fibers. The apparent viscosity gives insight about the nature of the keratocyte-proteoglycan content within the corneal stroma, and diffusivity describes the solute-fluid transport ability within the corneal stroma.

The tasks performed to develop AFM experimental techniques, add stress relaxation capability to the AFM system, and determine applicable contact mechanical models to corneal biomechanical response were then applied to the clinical application of keratoconus. Keratoconus is the most common corneal dystrophy in the United States, characterized by corneal mechanical compromise that leads to abnormal corneal thinning and steepening. Of the available treatment methods used to address this condition, corneal crosslinking techniques have been most effective in halting the progression of the disease. This treatment method encompasses the use of riboflavin, a photosensitizing agent, and ultraviolet light to induce crosslink formation between the collagen fibers within the corneal stroma, thereby increasing corneal mechanical strength. The Dresden protocol is the most widely-used corneal crosslinking technique, and is referred to as the standard crosslinking procedure. The developed AFM techniques and instrumentation were implemented to quantify the efficacy of the Dresden protocol along with two other

crosslinking alternates (one is an accelerated riboflavin-UV crosslinking technique and the other is a natural crosslinking agent, genipin) on the corneal biomechanical response. Two studies were conducted to quantify their effects within the porcine and human corneal models

The porcine corneal study investigated the effects of the three crosslinking techniques on measured mechanical properties at two stromal depths, the superficial and middle anterior regions. Results of the study revealed that the effect of the crosslinking techniques were depth-dependent, with the majority of mechanical effects occurring in the superficial anterior region. At the superficial anterior region, the crosslinking treatments produced statistically significant increases in corneal elasticity and decreases in corneal viscosity. However, no significant changes were observed for the corneal diffusivity. At the middle anterior stroma, no significant changes were produced by the treatments for corneal elasticity and viscoelasticity, but possible modification in solute transport was observed for the genipin treatment.

The human corneal study consisted of quantifying the effect of the Dresden technique, which is clinically approved in Europe, on the measured mechanical responses within the anterior stromal region. The results of the study showed that the Dresden crosslinking treatment method increased the human cornea's mechanical strength as corneal elasticity increased, yet its effect on corneal viscosity and diffusivity varied. Clinical implications of this study revealed that the Dresden treatment would be more effective in younger patient populations than older patient populations.

In conclusion, customized instrumentation and techniques were developed to adapt the technology of atomic force microscopy as a suitable characterization technique

within the field of corneal biomechanics. The constructed AFM system, experimentation techniques, and identified contact mechanical models enabled the ability to measure accurate elastic, viscoelastic, and poroelastic biomechanical responses of the corneal tissue *in situ*. Such engineering contributions were successfully applied to provide an objective and quantitative measure to determine the treatment efficacy of corneal crosslinking for keratoconus.

REFERENCES

Abad, J.C. and Panesso, J.L. (2008). "Corneal Crosslinking Induced by UVA and Riboflavin (CXL)." Techniques in Ophthalmology **6**(1): 8-12.

Abahussin, M., Hayes, S., Cartwright, N.E.K., Kamma-Lorger, C.S., Khan, Y., Marshall, J. and Meek, K.M. (2009). "3D Collagen Orientation Study of the Human Cornea Using X-ray Diffraction and Femtosecond Laser Technology." Investigative Ophthalmology & Visual Science **50**(11): 5159-5164.

Ahearne, M., Yang, Y., Then, K. and Liu, K.-K. (2007). "An Indentation Technique to Characterize the Mechanical and Viscoelastic Properties of Human and Porcine Corneas." Annals of Biomedical Engineering **35**(9): 1608-1616.

Andreassen, T.T., Simonsen, A.H. and Oxlund, H. (1980). "Biomechanical Properties of Keratoconus and Normal Corneas." Experimental Eye Research **31**(4): 435-441.

Arffa, R.C. and Grayson, M. (1997). Grayson's Diseases of the Cornea. St. Louis, Mo., Mosby.

Armstrong, J.K., Wenby, R.B., Meiselman, H.J. and Fisher, T.C. (2004). "The Hydrodynamic Radii of Macromolecules and Their Effect on Red Blood Cell Aggregation." Biophysical Journal **87**: 4259-4270.

Atchison, D.A. and Smith, G. (2003). Optics of the Human Eye. Oxford, England, Butterworth-Heinemann.

Avila, M.Y., Gerena, V.A. and Navia, J.L. (2012). "Corneal Crosslinking with Genipin, Comparison with UV-Riboflavin in Ex-Vivo Model." Molecular Vision **18**(112-14): 1068-1073.

Avila, M.Y. and Navia, J.L. (2010). "Effect of Genipin Collagen Crosslinking on Porcine Corneas." Journal of Cataract & Refractive Surgery **36**(4): 659-664.

Beshtawi, I.M., Akhtar, R., Hillarby, M.C., O'Donnell, C., Zhao, X.G., Brahma, A., Carley, F., Derby, B. and Radhakrishnan, H. (2013). "Biomechanical Properties of Human Corneas Following Low- and High-Intensity Collagen Cross-Linking Determined With Scanning Acoustic Microscopy." Investigative Ophthalmology & Visual Science **54**(8): 5273-5280.

Beshtawi, I.M., Akhtar, R., Hillarby, M.C., O'Donnell, C., Zhao, X.G., Brahma, A., Carley, F., Derby, B. and Radhakrishnan, H. (2014). "Biomechanical Changes After Repeated Collagen Cross-Linking on Human Corneas Assessed In Vitro Using Scanning Acoustic Microscopy." Investigative Ophthalmology & Visual Science **55**(3): 1549-1554.

Beuerman, R.W. and Pedroza, L. (1996). "Ultrastructure of the Human Cornea." Microscopy Research and Technique **33**(4): 320-335.

Bilodeau, G.G. (1992). "Regular Pyramid Punch Problem." Journal of Applied Mechanics-Transactions of the ASME **59**(3): 519-523.

Binnig, G., Quate, C.F. and Gerber, C. (1986). "Atomic Force Microscope." Physical Review Letters **56**: 930-933.

Borja, D., Manns, F., Lamar, P., Rosen, A., Fernandez, V. and Parel, J.-M. (2004). "Preparation and Hydration Control of Corneal Tissue Strips for Experimental Use." Cornea **23**(1).

Bourne, W.M., Nelson, L.R., Maguire, L.J., Baratz, K.H. and Hodge, D.O. (2001). "Comparison of Chen Medium and Optisol-GS for Human Corneal Preservation at 4 Degrees C: Results of Transplantation." Cornea **20**(7): 683-686.

Boyce, B.L., Grazier, J.M., Jones, R.E. and Nguyen, T.D. (2008). "Full-Field Deformation of Bovine Cornea under Constrained Inflation Conditions." Biomaterials **29**(28): 3896-3904.

Brightbill, F.S., McDonnell, P.J., McGhee, C.N.J., Farjo, A.A. and Serdarevic, O.N. (1986). Cornea Surgery: Theory, Technique, and Tissue. St. Louis, MO, Mosby/Elsevier.

Bron, A.J. (2001). "The Architecture of the Corneal Stroma." British Journal of Ophthalmology **85**(4): 379-381.

Bron, A.J., Tripathi, R.C. and Tripathi, B.J. (1997). Wolff's Anatomy of the Eye and Orbit. London, Chapman and Hall.

Brown, K.E. and Congdon, N.G. (2006). "Corneal Structure and Biomechanics: Impact on the Diagnosis and Management of Glaucoma." Current Opinion in Ophthalmology **17**(4): 338-343.

Bueno, J.M., Gualda, E.J. and Artal, P. (2011). "Analysis of Corneal Stroma Organization With Wavefront Optimized Nonlinear Microscopy." Cornea **30**(6): 692-701.

Cappella, B. and Dietler, G. (1999). "Force-Distance Curves by Atomic Force Microscopy." Surface Science Reports **34**(1-3): 1-+.

Cartwright, N.E.K., Tyrer, J.R. and Marshall, J. (2011). "Age-Related Differences in the Elasticity of the Human Cornea." Investigative Ophthalmology & Visual Science **52**(7): 4324-4329.

Cartwright, N.E.K., Tyrer, J.R. and Marshall, J. (2012). "In Vitro Quantification of the Stiffening Effect of Corneal Cross-linking in the Human Cornea using Radial Shearing Speckle Pattern Interferometry." Journal of Refractive Surgery **28**(7): 503-507.

Chadwick, R.S. (2002). "Axisymmetric Indentation of a Thin Incompressible Elastic Layer." SIAM Journal on Applied Mathematics **62**(5): 1520-1530.

Cheema, A.S., Mozayan, A. and Channa, P. (2012). "Corneal Collagen Crosslinking in Refractive Surgery." Current Opinion in Ophthalmology **23**(4): 251-256.

Cheneler, D., Mehrban, N. and Bowen, J. (2013). "Spherical Indentation Analysis of Stress Relaxation for Thin Film Viscoelastic Materials." Rheologica Acta **52**(7): 695-706.

Cheng, L., Xia, X., Scriven, L.E. and Gerberich, W.W. (2005). "Spherical-Tip Indentation of Viscoelastic Material." Mechanics of Materials **37**(1): 213-226.

Choi, S., Shin, J.-H., Cheong, Y., Jin, K.-H. and Park, H.-K. (2013). "Structural and Biomechanical Effects of Photooxidative Collagen Cross-Linking with Photosensitizer Riboflavin and 370 nm UVA Light on Human Corneoscleral Tissues." Microscopy and Microanalysis **19**(05): 1334-1340.

Clifford, C.A. and Seah, M.P. (2009). "Improved Methods and Uncertainty Analysis in the Calibration of the Spring Constant of an Atomic Force Microscope Cantilever using Static Experimental Methods." Measurement Science & Technology **20**(12).

Cowin, S.C. (1999). "Bone Poroelasticity." Journal of Biomechanics **32**(3): 217-238.

Dahl, B.J., Spotts, E. and Truong, J.Q. (2012). "Corneal Collagen Cross-linking: An Introduction and Literature Review." Optometry-Journal of the American Optometric Association **83**(1): 33-42.

Darling, E.M., Zauscher, S. and Guilak, F. (2006). "Viscoelastic Properties of Zonal Articular Chondrocytes Measured by Atomic Force Microscopy." Osteoarthritis and Cartilage **14**(6): 571-579.

Daxer, A., Misof, K., Grabner, B., Ettl, A. and Fratzl, P. (1998). "Collagen Fibrils in the Human Corneal Stroma: Structure and Aging." Investigative Ophthalmology & Visual Science **39**(3): 644-648.

DelMonte, D.W. and Kim, T. (2011). "Anatomy and Physiology of the Cornea." Journal of Cataract & Refractive Surgery **37**(3): 588-598.

Dias J, Ziebarth NM. Impact of Hydration Media on Ex Vivo Corneal Elasticity Measurements. Eye and Contact Lens. In press, 2014.

Dias, J., Diakonis, V.F., Kankariya, V.P., Yoo, S.H. and Ziebarth, N.M. (2013). "Anterior and Posterior Corneal Stroma Elasticity after Corneal Collagen Crosslinking Treatment." Experimental Eye Research **116**(0): 58-62.

Dias, J.M. and Ziebarth, N.M. (2013). "Anterior and Posterior Corneal Stroma Elasticity Assessed using Nanoindentation." Experimental Eye Research **115**: 41-46.

Dimitriadis, E.K., Horkay, F., Maresca, J., Kachar, B. and Chadwick, R.S. (2002). "Determination of Elastic Moduli of Thin Layers of Soft Material using the Atomic Force Microscope." Biophysical Journal **82**(5): 2798-2810.

Dorronsoro, C., Pascual, D., Perez-Merino, P., Kling, S. and Marcos, S. (2012). "Dynamic OCT Measurement of Corneal Deformation by an Air Puff in Normal and Cross-Linked Corneas." Biomedical Optics Express **3**(3): 473-487.

Duffey, R.J., Tchah, H. and Lindstrom, R.L. (1989). "Human Cadaver Corneal Thinning for Experimental Refractive Surgery." Refractive & Corneal Surgery **5**(1): 41-42.

Dupps, W.J., Netto, M.V., Herekar, S. and Krueger, R.R. (2007). "Surface Wave Elastometry of the Cornea in Porcine and Human Donor Eyes." Journal of Refractive Surgery **23**(1): 66-75.

Dupps, W.J. and Wilson, S.E. (2006). "Biomechanics and Wound Healing in the Cornea." Experimental Eye Research **83**(4): 709-720.

Ebenstein, D. and Pruitt, L. (2004). "Nanoindentation of Soft Hydrated Materials for Application to Vascular Tissues." Journal of Biomedical Materials Research Part A **69**(2): 222-232.

Ebenstein, D.M. and Pruitt, L.A. (2006). "Nanoindentation of Biological Materials." Nano Today **1**(3): 26-33.

Edwards, S.A., Ducker, W.A. and Sader, J.E. (2008). "Influence of Atomic Force Microscope Cantilever Tilt and Induced Torque on Force Measurements." Journal of Applied Physics **103**(6).

Elsheikh, A., Alhasso, D. and Rama, P. (2008). "Biomechanical Properties of Human and Porcine Corneas." Experimental Eye Research **86**(5): 783-790.

Elsheikh, A. and Anderson, K. (2005). "Comparative Study of Corneal Strip Extensometry and Inflation Tests." Journal of the Royal Society Interface **2**(3): 177-185.

Elsheikh, A., Geraghty, B., Rama, P., Campanelli, M. and Meek, K.M. (2010). "Characterization of Age-Related Variation in Corneal Biomechanical Properties." Journal of the Royal Society Interface **7**(51): 1475-1485.

Elsheikh, A., Wang, D.F., Brown, M., Rama, P., Campanelli, M. and Pye, D. (2007). "Assessment of Corneal Biomechanical Properties and Their Variation with Age." Current Eye Research **32**(1): 11-19.

Faber, C., Scherfig, E., Prause, J.U. and Sorensen, K.E. (2008). "Corneal Thickness in Pigs Measured by Ultrasound Pachymetry In Vivo." Scandinavian Journal of Laboratory Animal Science **35**(1): 39-43.

Fernandez, D.C., Niazy, A.M., Kurtz, R.M., Djotyan, G.P. and Juhasz, T. (2005). "Finite Element Analysis Applied to Cornea Reshaping." Journal of Biomedical Optics **10**(6).

Ferry, J.D. (1980). Viscoelastic Properties of Polymers. New York, Wiley.

Fischer-Cripps, A.C. (2002). Nanoindentation. Springer-Verlag.

Ford, M., Dupps, W.J., Huprikar, N., Lin, R. and Rollins, A.M. (2006). "OCT Corneal Elastography by Pressure-Induced Optical Feature Flow - art. no. 61380P." Ophthalmic Technologies XVI **6138**: P1380-P1380.

Ford, M.R., Dupps, W.J., Rollins, A.M., Roy, A.S. and Hu, Z.L. (2011). "Method for Optical Coherence Elastography of the Cornea." Journal of Biomedical Optics **16**(1).

Freund, D.E., Mccally, R.L., Farrell, R.A., Cristol, S.M., Lhernault, N.L. and Edelhauser, H.F. (1995). "Ultrastructure in Anterior and Posterior Stroma of Perfused Human and Rabbit Corneas - Relation to Transparency." Investigative Ophthalmology & Visual Science **36**(8): 1508-1523.

Fung, Y.C. (1965). Foundations of Solid Mechanics. Englewood Cliffs, N.J., Prentice-Hall.

Fung, Y.C. (1993). Biomechanics : Mechanical Properties of Living Tissues. New York, Springer-Verlag.

Gao, H., Chiu, C.H. and Lee, J. (1992). "Elastic Contact Versus Indentation Modeling of Multi-Layered Materials." International Journal of Solids and Structures **29**(20): 2471-2492.

Gates, R.S. and Reitsma, M.G. (2007). "Precise Atomic Force Microscope Cantilever Spring Constant Calibration using a Reference Cantilever Array." Review of Scientific Instruments **78**(8).

Gibson, C.T., Watson, G.S. and Myhra, S. (1996). "Determination of the Spring Constants of Probes for Force Microscopy/Spectroscopy." Nanotechnology **7**(3): 259-262.

Gibson, C.T., Watson, G.S. and Myhra, S. (1997). "Scanning Force Microscopy - Calibrative Procedures for 'Best Practice'." Scanning **19**(8): 564-581.

Grabner, G., Ellmsteiner, R., Steindl, C., Ruckhofer, J., Mattioli, R. and Husinsky, W. (2005). "Dynamic Corneal Imaging." Journal of Cataract & Refractive Surgery **31**(1): 163-174.

Hamaoui, M., Tahi, H., Chapon, P., Duchesne, B., Fantes, F., Feuer, W. and Parel, J.M. (2001). "Corneal Preparation of Eye Bank Eyes for Experimental Surgery." Cornea **20**(3): 317-320.

Hammer, A., Richoz, O., Mosquera, S.A., Tabibian, D., Hoogewoud, F. and Hafezi, F. (2014). "Corneal Biomechanical Properties at Different Corneal Cross-Linking (CXL) Irradiances." Investigative Ophthalmology & Visual Science **55**(5): 2881-2884.

Harada, Y. and Naoi, N. (2004). "Corneal Elasticity as a Measure of Intra-Ocular Pressure: A Controlled Clinical Examination." The Kobe Journal of Medical Sciences **50**(5-6): 141-152.

Hatami-Marbini, H. and Rahimi, A. (2014). "Effects of Bathing Solution on Tensile Properties of the Cornea." Experimental Eye Research **120**: 103-108.

Hertz, H. (1881). "Uber die beruhrung fester elastischer korper (On the Contact of Elastic Solids)." J. Reine Angew. Math **92**.

Hjortdal, J.O. (1996). "Regional Elastic Performance of the Human Cornea." Journal of Biomechanics **29**(7): 931-942.

Hjortdal, J.O. and Ehlers, N. (1995). "Effect of Excimer Laser Keratectomy on the Mechanical Performance of the Human Cornea." Acta Ophthalmologica Scandinavica **73**(1): 18-24.

Hoeltzel, D.A., Altman, P., Buzard, K. and Choe, K. (1992). "Strip Extensiometry for Comparison of the Mechanical Response of Bovine, Rabbit, and Human Corneas." Journal of Biomechanical Engineering **114**(2): 202-215.

Hollman, K.W., Emelianov, S.Y., Neiss, J.H., Jotyan, G., Spooner, G.J.R., Juhasz, T., Kurtz, R.M. and O'Donnell, M. (2002). "Strain Imaging of Corneal Tissue with an Ultrasound Elasticity Microscope." Cornea **21**(1): 68-73.

Hovakimyan, M., Guthoff, R.F. and Stachs, O. (2012). "Collagen Cross-linking: Current Status and Future Directions." Journal of Ophthalmology **2012**: 406850.

Hu, Y.H., Zhao, X.H., Vlassak, J.J. and Suo, Z.G. (2010). "Using Indentation to Characterize the Poroelasticity of Gels." Applied Physics Letters **96**(12).

Hutter, J.L. and Bechhoefer, J. (1993). "Calibration of Atomic-Force Microscope Tips." Review of Scientific Instruments **64**(7): 1868-1873.

Institute, N.E. (2013). "Facts about Cornea and Corneal Disease." Retrieved July 30, 2012, from http://www.nei.nih.gov/health/cornealdisease.

Iseli, H.P., Popp, M., Seiler, T., Spoerl, E. and Mrochen, M. (2011). "Laboratory Measurement of the Absorption Coefficient of Riboflavin for Ultraviolet Light (365 nm)." Journal of Refractive Surgery **27**(3): 195-201.

Jablonski-Stiemke, M.M. and Edelhauser, H.F. (1998). "Storage of Human Corneas in Dextran and Chondroitin Sulfate–Based Corneal Storage Medium: Changes in Stromal Free Sodium." Archives of Ophthalmology **116**(5): 627-632.

Jayasuriya, A.C., Ghosh, S., Scheinbeim, J.I., Lubkin, V., Bennett, G. and Kramer, P. (2003). "A Study of Piezoelectric and Mechanical Anisotropies of the Human Cornea." Biosensors & Bioelectronics **18**(4): 381-387.

Jaycock, P.D., Lobo, L., Ibrahim, J., Tyrer, J. and Marshall, J. (2005). "Interferometric Technique to Measure Biomechanical Changes in the Cornea Induced by Refractive Surgery." Journal of Cataract & Refractive Surgery **31**(1): 175-184.

Johnson, K.L. (1985). Contact Mechanics. Cambridge Cambridgeshire ; New York, Cambridge University Press.

Jue, B. and Maurice, D.M. (1986). "The Mechanical Properties of the Rabbit and Human Cornea." Journal of Biomechanics **19**(10): 847-853.

Kalcioglu, Z.I., Mahmoodian, R., Hu, Y.H., Suo, Z.G. and Van Vliet, K.J. (2012). "From Macro- to Microscale Poroelastic Characterization of Polymeric Hydrogels Via Indentation." Soft Matter **8**(12): 3393-3398.

Karrasch, S., Hegerl, R., Hoh, J.H., Baumeister, W. and Engel, A. (1994). "Atomic Force Microscopy Produces Faithful High-Resolution Images of Protein Surfaces in an Aqueous Environment." Proceedings of the National Academy of Sciences of the United States of America **91**(3): 836-838.

Kaufman, J.D., Miller, G.J., Morgan, E.F. and Klapperich, C.M. (2008). "Time-Dependent Mechanical Characterization of Poly(2-hydroxyethyl methacrylate) Hydrogels using Nanoindentation and Unconfined Compression." Journal of Materials Research **23**(5): 1472-1481.

Khadem, J., Truong, T. and Ernest, J.T. (1994). "Photodynamic Biologic Tissue Glue." Cornea **13**(5): 406-410.

King, R. (1987). "Elastic Analysis of Some Punch Problems for a Layered Medium." International Journal of Solids and Structures **23**(12): 1657-1664.

Kling, S., Ginis, H. and Marcos, S. (2012). "Corneal Biomechanical Properties from Two-Dimensional Corneal Flap Extensiometry: Application to UV-Riboflavin Cross-Linking." Investigative Ophthalmology & Visual Science **53**(8): 5010-5015.

Kling, S. and Marcos, S. (2013). "Effect of Hydration State and Storage Media on Corneal Biomechanical Response from In Vitro Inflation Tests." Journal of Refractive Surgery **29**(7): 490-497.

Kling, S., Remon, L., Perez-Escudero, A., Merayo-Lloves, J. and Marcos, S. (2010). "Corneal Biomechanical Changes after Collagen Cross-Linking from Porcine Eye Inflation Experiments." Investigative Ophthalmology & Visual Science **51**(8): 3961-3968.

Kohlhaas, M., Spoerl, E., Schilde, T., Unger, G., Wittig, C. and Pillunat, L.E. (2006). "Biomechanical Evidence of the Distribution Of Cross-Links in Corneas Treated with Riboflavin And Ultraviolet A Light." Journal of Cataract & Refractive Surgery **32**(2): 279-283.

Komai, Y. and Ushiki, T. (1991). "The Three-Dimensional Organization of Collagen Fibrils in the Human Cornea and Sclera." Investigative Ophthalmology & Visual Science **32**(8): 2244-2258.

Kotecha, A. (2007). "What Biomechanical Properties of the Cornea Are Relevant for the Clinician?" Survey of Ophthalmology **52**: S109-S114.

Krachmer, J.H., Feder, R.S. and Belin, M.W. (1984). "Keratoconus and Related Noninflammatory Corneal Thinning Disorders." Survey of Ophthalmology **28**(4): 293-322.

Krachmer, J.H., Mannis, M.J. and Holland, E.J. (2011). Cornea. St. Louis, MO, Elsevier/Mosby.

Kuo, I.C., Broman, A., Pirouzmanesh, A. and Melia, M. (2006). "Is There An Association Between Diabetes and Keratoconus?" Ophthalmology **113**(2): 184-190.

Lal, R. and John, S.A. (1994). "Biological Applications of Atomic Force Microscopy." American Journal of Physiology **266**(1 Pt 1): C1-21.

Lanchares, E., del Buey, M.A., Cristobal, J.A., Lavilla, L. and Calvo, B. (2011). "Biomechanical Property Analysis after Corneal Collagen Cross-Linking in Relation to Ultraviolet A Irradiation Time." Graefes Arch Clin Exp Ophthalmol **249**(8): 1223-1227.

Last, J.A., Liliensiek, S.J., Nealey, P.F. and Murphy, C.J. (2009). "Determining the Mechanical Properties of Human Corneal Basement Membranes with Atomic Force Microscopy." Journal of Structural Biology **167**(1): 19-24.

Last, J.A., Thomasy, S.M., Croasdale, C.R., Russell, P. and Murphy, C.J. (2012). "Compliance Profile of the Human Cornea as Measured by Atomic Force Microscopy." Micron **43**(12): 1293-1298.

Ledoux, B. and Ching, R. (2014). "BIOEN 520 Musculoskeletal (Orthopedic) Biomechanics Lecture Notes: Mechanical Properties of Biological Tissues." University of Washington, Depts. of Bioengineering and Mechanical Engineering.

Lens, A. (1999). Ocular Anatomy and Physiology. Thorofare, NJ, SLACK.

Li, C., Guan, G., Huang, Z., Johnstone, M. and Wang, R.K. (2012). "Noncontact All-Optical Measurement of Corneal Elasticity." Optics letters **37**(10): 1625-1627.

Lin, D.C. and Horkay, F. (2008). "Nanomechanicsof Polymer Gels and Biological Tissues: A Critical Review of Analytical Approaches in the Hertzian Regime And Beyond." Soft Matter **4**(4): 669-682.

Liu, J., He, X., Pan, X. and Roberts, C.J. (2007). "Ultrasonic Model and System for Measurement of Corneal Biomechanical Properties and Validation on Phantoms." Journal of Biomechanics **40**(5): 1177-1182.

Liu, J. and Roberts, C.J. (2005). "Influence of Corneal Biomechanical Properties on Intraocular Pressure Measurement: Quantitative Analysis." Journal of Cataract & Refractive Surgery **31**(1): 146-155.

Lombardo, M., Lombardo, G., Carbone, G., De Santo, M.P., Barberi, R. and Serrao, S. (2012). "Biomechanics of the Anterior Human Corneal Tissue Investigated with Atomic Force Microscopy." Investigative Ophthalmology & Visual Science **53**(2): 1050-1057.

Lombardo, M., Serrao, S., Rosati, M., Ducoli, P. and Lombardo, G. (2014). "Biomechanical Changes in the Human Cornea after Transepithelial Corneal Crosslinking using Iontophoresis." Journal of Cataract & Refractive Surgery **40**(10): 1706-1715.

Luce, D.A. (2005). "Determining In Vivo Biomechanical Properties of the Cornea with an Ocular Response Analyzer." Journal of Cataract & Refractive Surgery **31**(1): 156-162.

Mahaffy, R.E., Park, S., Gerde, E., Kas, J. and Shih, C.K. (2004). "Quantitative Analysis of the Viscoelastic Properties of Thin Regions of Fibroblasts using Atomic Force Microscopy." Biophysical Journal **86**(3): 1777-1793.

Malik, N.S., Moss, S.J., Ahmed, N., Furth, A.J., Wall, R.S. and Meek, K.M. (1992). "Aging of the Human Corneal Stroma - Structural and Biochemical-Changes." Biochimica Et Biophysica Acta **1138**(3): 222-228.

Mansouri, K., Leite, M.T., Weinreb, R.N., Tafreshi, A., Zangwill, L.M. and Medeiros, F.A. (2012). "Association Between Corneal Biomechanical Properties and Glaucoma Severity." American Journal of Ophthalmology **153**(3): 419-427.e411.

Marcos, S., Kling, S., Bekesi, N. and Dorronsoro, C. (2014). "Corneal Biomechanical Properties from Air-Puff Corneal Deformation Imaging." Optical Elastography and Tissue Biomechanics **8946**.

Mastropasqua, L., Lanzini, M., Curcio, C., Calienno, R., Mastropasqua, R., Colasante, M., Mastropasqua, A. and Nubile, M. (2014). "Structural Modifications and Tissue Response after Standard Epi-Off and Iontophoretic Corneal Crosslinking with Different Irradiation Procedures." Investigative Ophthalmology & Visual Science **55**(4): 2526-2533.

Mattice, J.M., Lau, A.G., Oyen, M.L. and Kent, R.W. (2006). "Spherical Indentation Load-Relaxation of Soft Biological Tissues." Journal of Materials Research **21**(8): 2003-2010.

Maxwell, J.C. (1867). "On the Dynamical Theory of Gases." Phil. Trans. R. Soc. Lond. **157**.

Mazzotta, C., Balestrazzi, A., Traversi, C., Baiocchi, S., Caporossi, T., Tommasi, C. and Caporossi, A. (2007). "Treatment of Progressive Keratoconus by Riboflavin-UVA-Induced Cross-Linking of Corneal Collagen - Ultrastructural Analysis by Heidelberg Retinal Tomograph In Vivo Confocal Microscopy in Humans." Cornea **26**(4): 390-397.

Medeiros, F.A. and Weinreb, R.N. (2006). "Evaluation of the Influence of Corneal Biomechanical Properties on Intraocular Pressure Measurements using the Ocular Response Analyzer." Journal of Glaucoma **15**(5): 364-370.

Menard, K.P. (2008). Dynamic Mechanical Analysis : A Practical Introduction. Boca Raton, FL, CRC Press.

Mikula, E., Hollman, K., Chai, D., Jester, J.V. and Juhasz, T. (2014). "Measurement of Corneal Elasticity with an Acoustic Radiation Force Elasticity Microscope." Ultrasound Med Biol **40**(7): 1671-1679.

Mita, M., Waring Iv, G.O. and Tomita, M. (2014). "High-Irradiance Accelerated Collagen Crosslinking for the Treatment of Keratoconus: Six-Month Results." Journal of Cataract & Refractive Surgery **40**(6): 1032-1040.

Morishige, N., Takagi, Y., Chikama, T., Takahara, A. and Nishida, T. (2011). "Three-Dimensional Analysis of Collagen Lamellae in the Anterior Stroma of the Human Cornea Visualized by Second Harmonic Generation Imaging Microscopy." Investigative Ophthalmology & Visual Science **52**(2): 911-915.

Nash, I.S., Greene, P.R. and Foster, C.S. (1982). "Comparison of Mechanical Properties of Keratoconus and Normal Corneas." Experimental Eye Research **35**(5): 413-424.

Neubert, H.K.P. (1963). "A Simple Model Representing Internal Damping in Solid Materials." Aeronautical Quarterly **14**(2): 187-210.

Ohler, B. "Practical Advice on the Determination of Cantilever Spring Constants." Veeco Application Note.

Ortiz, D., Pinero, D., Shabayek, M.H., Arnalich-Montiel, F. and Alio, J.L. (2007). "Corneal Biomechanical Properties in Normal, Post-Laser In Situ Keratomileusis, and Keratoconic Eyes." Journal of Cataract & Refractive Surgery **33**(8): 1371-1375.

Overney, G., Tomanek, D., Zhong, W., Sun, Z., Miyazaki, H., Mahanti, S.D. and Guntherodt, H.J. (1992). "Theory for the Atomic Force Microscopy of Layered Elastic Surfaces." Journal of Physics-Condensed Matter **4**(17): 4233-4249.

Oyen, M.L. (2006). "Analytical Techniques for Indentation Of Viscoelastic Materials." Philosophical Magazine **86**(33-35): 5625-5641.

Palomino, C., Castillo, A., Cristobal, J.A., Angeles del Buey, M. and Carmona, D. (2011). "Corneal Biomechanics after Refractive Surgery: A Comparison Between Surgical Techniques." Journal of Emmetropia **2**: 127-130.

Patel, S., Marshall, J. and Fitzke, F.W., 3rd (1995). "Refractive Index of the Human Corneal Epithelium and Stroma." Journal Of Refractive Surgery (Thorofare, N J : 1995) **11**(2): 100-105.

Pepose, J.S., Feigenbaum, S.K., Qazi, M.A., Sanderson, J.P. and Roberts, C.J. (2007). "Changes in Corneal Biomechanics and Intraocular Pressure Following LASIK using Static, Dynamic, and Noncontact Tonometry." American Journal of Ophthalmology **143**(1): 39-47.

Pillarisetti, A. (2008). Mechanical Manipulation and Characterization of Biological Cells. 3341362 Ph.D., University of Maryland, College Park.

Poon, B., Rittel, D. and Ravichandran, G. (2008). "An Analysis of Nanoindentation in Linearly Elastic Solids." International Journal of Solids and Structures **45**(24): 6018-6033.

Randleman, J.B., Dawson, D.G., Grossniklaus, H.E., McCarey, B.E. and Edelhauser, H.F. (2008). "Depth-Dependent Cohesive Tensile Strength in Human Donor Corneas: Implications for Refractive Surgery." Journal Of Refractive Surgery (Thorofare, N J : 1995) **24**(1): S85-89.

Rao, C.L. and Deshpande, A.P. (2014). Modelling of Engineering Materials, John Wiley & Sons, Limited.

Reichert. (2009). "Reichert's Ocular Response Analyzer: How Does It Work?", from http://www.ocularresponseanalyzer.com/how.htm.

Reinstein, D.Z., Archer, T.J., Gobbe, M., Silverman, R.H. and Coleman, D.J. (2009). "Stromal Thickness in the Normal Cornea: Three-Dimensional Display with Artemis Very High-Frequency Digital Ultrasound." Journal of Refractive Surgery (Thorofare, N J : 1995) **25**(9): 776-786.

Rico, F., Roca-Cusachs, P., Gavara, N., Farre, R., Rotger, M. and Navajas, D. (2005). "Probing Mechanical Properties of Living Cells by Atomic Force Microscopy with Blunted Pyramidal Cantilever Tips." Physical Review E, Statistical, Nonlinear, and Soft Matter Physics **72**(2 Pt 1): 021914.

Romero-Jimenez, M., Santodomingo-Rubido, J. and Wolffsohn, J.S. (2010). "Keratoconus: A Review." Contact Lens & Anterior Eye : The Journal of the British Contact Lens Association **33**(4): 157-166; quiz 205.

Rosenbluth, M.J. (2008). Probing the Role of Single Cell Mechanics in Disease with Atomic Force Microscopy and Microfluidics. 3334274 Ph.D., University of California, Berkeley.

Roy, A.S., Rocha, K.M., Randleman, J.B., Stulting, R.D. and Dupps, W.J. (2013). "Inverse Computational Analysis of In Vivo Corneal Elastic Modulus Change after Collagen Crosslinking for Keratoconus." Experimental Eye Research **113**: 92-104.

Ruberti, J.W., Roy, A.S. and Roberts, C.J. (2011). "Corneal Biomechanics and Biomaterials." Annual Review of Biomedical Engineering **13**: 269-295.

Sader, J.E., Larson, I., Mulvaney, P. and White, L.R. (1995). "Method for the Calibration of Atomic-Force Microscope Cantilevers." Review of Scientific Instruments **66**(7): 3789-3798.

Scarcelli, G., Pineda, R. and Yun, S.H. (2012). "Brillouin Optical Microscopy for Corneal Biomechanics." Investigative Ophthalmology & Visual Science **53**(1): 185-190.

Schumacher, S., Oeftiger, L. and Mrochen, M. (2011). "Equivalence of Biomechanical Changes Induced by Rapid and Standard Corneal Cross-Linking, using Riboflavin and Ultraviolet Radiation." Investigative Ophthalmology & Visual Science **52**(12): 9048-9052.

Seherr-Thomas, H.C., Schmelz, F. and Aucktor, E. (2006). Hertzian Theory and the Limits of Its Application. Universal Joints and Driveshafts: Analysis, Design, Applications. New York, Springer.

Seiler, T., Huhle, S., Spoerl, E. and Kunath, H. (2000). "Manifest Diabetes and Keratoconus: A Retrospective Case-Control Study." Graefe's Archive for Clinical and Experimental Ophthalmology = Albrecht von Graefes Archiv fur klinische und experimentelle Ophthalmologie **238**(10): 822-825.

Seiler, T., Matallana, M., Sendler, S. and Bende, T. (1992). "Does Bowman's Layer Determine the Biomechanical Properties of the Cornea?" Refractive & Corneal Surgery **8**(2): 139-142.

Seino, Y. (2007). Analysis of Indentation Depth Dependence of Elastic Properties of Inter-Layer Dielectric Films on Silicon. HARDMEKO 2007. Tsukuba, Japan**:** 130-135.

Shah, S., Laiquzzaman, M., Bhojwani, R., Mantry, S. and Cunliffe, I. (2007). "Assessment of the Biomechanical Properties of the Cornea with the Ocular Response Analyzer in Normal and Keratoconic Eyes." Investigative Ophthalmology & Visual Science **48**(7): 3026-3031.

Slattery, A.D., Blanch, A.J., Quinton, J.S. and Gibson, C.T. (2013). "Calibration of Atomic Force Microscope Cantilevers using Standard and Inverted Static Methods assisted by FIB-Milled Spatial Markers." Nanotechnology **24**(1).

Sneddon, I.N. (1948). "Boussinesq's Problem for a Rigid Cone." Mathematical Proceedings of the Cambridge Philosophical Society **44**: 492-507.

Sneddon, I.N. (1965). "The Relation between Load and Penetration in the Axisymmetric Boussinesq Problem for a Punch of Arbitrary Profile." International Journal of Engineering Science **3**: 47-57.

Sondergaard, A.P., Ivarsen, A. and Hjortdal, J. (2013). "Corneal Resistance to Shear Force After UVA-Riboflavin Cross-Linking." Investigative Ophthalmology & Visual Science **54**(7): 5059-5069.

Spoerl, E., Huhle, M. and Seiler, T. (1998). "Induction of Cross-Links in Corneal Tissue." Experimental Eye Research **66**(1): 97-103.

Spoerl, E. and Seiler, T. (1999). "Techniques for Stiffening the Cornea." Journal of Refractive Surgery **15**(6): 711-713.

Srinivasa, R. and Eswara, R. (2008). "An FEM Approach into Nanoindentation on Linear Elastic and Viscoelastic Characterization of Soft Living Cells." International Journal of Nanotechnology Applications **2**(1): 55-68.

Swinger, C.A. and Kornmehl, E.W. (1985). "Dehydration of Post-Mortem Eyes for Practice and Experimental Surgery." Ophthalmic Surgery **16**(3): 182-183.

Tanter, M., Touboul, D., Gennisson, J.L., Bercoff, J. and Fink, M. (2009). "High-Resolution Quantitative Imaging of Cornea Elasticity Using Supersonic Shear Imaging." IEEE Transactions on Medical Imaging **28**(12): 1881-1893.

Tao, A.Z., Wang, J.H., Chen, Q., Shen, M.X., Lu, F., Dubovy, S.R. and Abou Shousha, M. (2011). "Topographic Thickness of Bowman's Layer Determined by Ultra-High Resolution Spectral Domain-Optical Coherence Tomography." Investigative Ophthalmology & Visual Science **52**(6): 3901-3907.

Terry, M.A., Ousley, P.J. and Zjhra, M.L. (1994). "Hydration Changes in Cadaver Eyes Prepared for Practice and Experimental Surgery." Archives of Ophthalmology **112**(4): 538-543.

Thomasy, S.M., Raghunathan, V.K., Winkler, M., Reilly, C.M., Sadeli, A.R., Russell, P., Jester, J.V. and Murphy, C.J. (2014). "Elastic Modulus and Collagen Organization of the Rabbit Cornea: Epithelium to Endothelium." Acta Biomaterialia **10**(2): 785-791.

Tomanek, D., Overney, G., Miyazaki, H., Mahanti, S.D. and Guntherodt, H.J. (1989). "Theory for the Atomic Force Microscopy of Deformable Surfaces." Physical Review Letters **63**(8): 876-879.

Tomita, M., Mita, M. and Huseynova, T. (2014). "Accelerated versus Conventional Corneal Collagen Crosslinking." Journal of Cataract & Refractive Surgery **40**(6): 1013-1020.

Touboul, D., Efron, N., Smadja, D., Praud, D., Malet, F. and Colin, J. (2012). "Corneal Confocal Microscopy Following Conventional, Transepithelial, and accelerated Corneal Collagen Cross-Linking Procedures for Keratoconus." Journal of Refractive Surgery (Thorofare, NJ: 1995) **28**(11): 769-776.

Trattler, W.B. (2010). Cornea Handbook. Thorofare, NJ, SLACK.

Tripathy, S. and Berger, E.J. (2009). "Measuring Viscoelasticity of Soft Samples Using Atomic Force Microscopy." Journal of Biomechanical Engineering-Transactions of the Asme **131**(9).

Tripathy, S. and Berger, E.J. (2012). "Quasi-linear Viscoelastic Properties of Costal Cartilage using Atomic Force Microscopy." Computer Methods in Biomechanics and Biomedical Engineering **15**(5): 475-486.

Tropea, C., Yarin, A.L. and Foss, J.F. (2007). Springer Handbook of Experimental Fluid Mechanics. Berlin, Springer.

Turss, R., Friend, J., Reim, M. and Dohlman, C. (1971). "Glucose Concentration and Hydration of the Corneal Stroma." Ophthalmic Research **2**: 253-260.

Vadillo-Rodriguez, V., Beveridge, T.J. and Dutcher, J.R. (2008). "Surface Viscoelasticity of Individual Gram-Negative Bacterial Cells Measured using Atomic Force Microscopy." Journal of Bacteriology **190**(12): 4225-4232.

Wang, B.R., Lancon, P., Bienvenu, C., Vierling, P., Di Giorgio, C. and Bossis, G. (2013). "A General Approach for the Microrheology of Cancer Cells by Atomic Force Microscopy." Micron **44**: 287-297.

Wang, H., Prendiville, P.L., McDonnell, P.J. and Chang, W.V. (1996). "An Ultrasonic Technique for the Measurement of the Elastic Moduli of Human Cornea." Journal of Biomechanics **29**(12): 1633-1636.

Wernli, J., Schumacher, S., Spoerl, E. and Mrochen, M. (2013). "The Efficacy of Corneal Cross-Linking Shows a Sudden Decrease with Very High Intensity UV Light and Short Treatment Time." Investigative Ophthalmology & Visual Science **54**(2): 1176-1180.

Wilson, S.E. and Hong, J.W. (2000). "Bowman's Layer Structure and Function: Critical or Dispensable to Corneal Function? A Hypothesis." Cornea **19**(4): 417-420.

Winkler, M., Chai, D., Kriling, S., Nien, C.J., Brown, D.J., Jester, B., Juhasz, T. and Jester, J.V. (2011). "Nonlinear Optical Macroscopic Assessment of 3-D Corneal Collagen Organization and Axial Biomechanics." Investigative Ophthalmology & Visual Science **52**(12): 8818-8827.

Wojcikiewicz, E.P., Zhang, X., Chen, A. and Moy, V.T. (2003). "Contributions of Molecular Binding Events and Cellular Compliance to the Modulation of Leukocyte Adhesion." Journal of Cell Science **116**(Pt 12): 2531-2539.

Wollensak, G. (2006). "Crosslinking Treatment of Progressive Keratoconus: New Hope." Current Opinion In Ophthalmology **17**(4): 356-360.

Wollensak, G., Aurich, H., Wirbelauer, C. and Sel, S. (2010). "Significance of the Riboflavin Film in Corneal Collagen Crosslinking." Journal of Cataract & Refractive Surgery **36**(1): 114-120.

Wollensak, G. and Iomdina, E. (2009). "Biomechanical and Histological Changes after Corneal Crosslinking With and Without Epithelial Debridement." Journal of Cataract & Refractive Surgery **35**(3): 540-546.

Wollensak, G. and Iomdina, E. (2009). "Long-term Biomechanical Properties of Rabbit Sclera after Collagen Crosslinking using Riboflavin and Ultraviolet A (UVA)." Acta Ophthalmologica **87**(2): 193-198.

Wollensak, G., Spoerl, E. and Seiler, T. (2003). "Riboflavin/Ultraviolet-A-Induced Collagen Crosslinking for the Treatment of Keratoconus." American Journal of Ophthalmology **135**(5): 620-627.

Wollensak, G., Spoerl, E. and Seiler, T. (2003). "Stress-Strain Measurements of Human and Porcine Corneas after Riboflavin-Ultraviolet-A-Induced Cross-Linking." Journal of Cataract & Refractive Surgery **29**(9): 1780-1785.

Wollensak, G., Wilsch, M., Spoerl, E. and Seiler, T. (2004). "Collagen Fiber Diameter in the Rabbit Cornea after Collagen Crosslinking by Riboflavin/UVA." Cornea **23**(5): 503-507.

Wu, H.W., Kuhn, T. and Moy, V.T. (1998). "Mechanical Properties of L929 Cells Measured by Atomic Force Microscopy: Effects of Anticytoskeletal Drugs and Membrane Crosslinking." Scanning **20**(5): 389-397.

Yoo, L., Reed, J., Shin, A., Kung, J., Gimzewski, J.K., Poukens, V., Goldberg, R.A., Mancini, R., Taban, M., Moy, R. and Demer, J.L. (2011). "Characterization of Ocular Tissues Using Microindentation and Hertzian Viscoelastic Models." Investigative Ophthalmology & Visual Science **52**(6): 3475-3482.

Zeng, Y., Yang, J., Huang, K., Lee, Z. and Lee, X. (2001). "A Comparison of Biomechanical Properties between Human and Porcine Cornea." Journal of Biomechanics **34**(4): 533-537.

Zhang, Y.T., Conrad, A.H. and Conrad, G.W. (2011). "Effects of Ultraviolet-A and Riboflavin on the Interaction of Collagen and Proteoglycans during Corneal Cross-linking." Journal of Biological Chemistry **286**(15): 13011-13022.

Ziebarth, N.M. (2008). Atomic Force Microscopy Measurement of the Elastic Properties of the Lens. PhD, University of Miami.

Ziebarth, N.M., Rico, F. and Moy, V.T. (2010). Structural and Mechanical Mechanisms of Ocular Tissues Probed by AFM. Applied Scanning Probe Methods. B. Bhushan**:** 14-16.

APPENDIX 1

STRESS RELAXATION IGOR PRO CODE MODIFICATIONS

DoForceScan Function

```
//Does a force scan
Function DoForceScan(ctrName) : ButtonControl
String ctrName
SVAR experimentName=root:userParams:experimentName
SVAR setName=root:userParams:setName
if (strlen(experimentName)*strlen(setName)==0)
doAlert 0, "You must provide an experiment Name and a set Name"
return 1
endif
SetDataFolder root:userFlags
NVAR channel0selected, channel1selected, channel2Selected, channel3Selected,
channel3LimitSelected, displayDataBetweenScans, autosaveData,osciInsteadDwell,
showCalibrated
SetDataFolder root:userParams
NVAR startptnm, endptnm, stepsize,stepsized, delaydown, dwellTime,
timeBetweenScans, delayup, numscans
WAVE ForceScanChannelNumber, LastForceScanChannelNumber,
ForceScanChannelLimitSettings
NVAR UpdateRate, windowKilling
SetDataFolder root:systemParams
NVAR startptV, endptV,lastChannelCount, nmOf0V, nmOf10V
SVAR TxtForceCmt
NVAR lastCollectedRetractSampleCount, lastCollectedForwardSampleCount
SetDataFolder root:systemFlags
NVAR MultimeterOn, calibrated
SetDataFolder root:userFlags
NVAR UpdateMultimeterBetweenScans
NewDataFolder /O/S root:forceScans
String name, NumStr, sStr, sStr1, sStrA, sStrR
String sStrC, sStrCE
Variable i=0, wsize, smid, j, k, sL2,smid1, smf, sSegT, d=0
Variable/G ForwardSampleBlocks, BitCollectingDelay, RetractSampleBlocks, sFlag1,
sL, multstatus
Variable numscansD, integersearch,indexloc
Variable lengthInWave, SRContactSampleBlocks, SRSamplingInterval, index,
SRstartingV
Variable/G SRBitCollectingDelay

….
//Stress Relaxation Parameters
SRBitCollectingDelay=400 //Total Sampling Rate/# channels used
```

```
SRSamplingInterval=0.001 //Total Sampling Rate is 1 millisecond sampling interval
SRContactSampleBlocks=((dwellTime*(1/60))/SRSamplingInterval) //Calculates # of
sample blocks

//PREPARING FOR STRESS RELAXATION
if (dwellTime!=0)
        //Making Stress Relaxation contact outwave
        Make/O /N=12000 FWaveWSRC
        Make/O /N=12000 FWaveCI
        //Creating InWave for SRContact
        Make /N=(SRContactSampleBlocks*lastChannelCount) /O FWaveSRWaveIn
endif

….
//Making Stress Relaxation contact outwave
if (osciInsteadDwell==0 && dwellTime!=0)
        FWaveWSRC=FWaveWA[lastCollectedForwardSampleCount-1]
        sStrC=" "
endif
if (osciInsteadDwell==0 && dwellTime!=0)
        //Sending Stress Relaxation Output Wave to ITC-18 FIFO
        Execute "ITC18stim FWaveWSRC"
        //Writing date of stress relaxation
        sSegT=ticks
        sStrC=sStrC+"\r\nStress Relaxation @ Start at: "+secs2date(datetime,1)+ "
        "+secs2time(datetime,3)
        print secs2time(datetime,3)
        printf "start sr acquisition"
        //Start Acquiring Data
        Execute "ITC18startacq "+num2str(SRBitCollectingDelay)+",2,0"
        //Retrieve data and place into FWaveSRWaveIn
        Execute "ITC18samp FWaveSRWaveIn"
        //Stop Acquisition
        Execute "ITC18stopAcq"
        //Saving FWaveSRWaveIn
        save /J/O FWaveSRWaveIn as "C:\\Documents and
        Settings\\AFM2\Desktop\\TEST VARIABLES\\FWaveSRWaveInWithData.txt"
        //Writing end of stress relaxation
        print secs2time(datetime,3)
        printf "sr finished"
        sSegT=ticks
        sStrC= sStrC+ " @Stop At: "+secs2date(datetime,1)+ " "+secs2time(datetime,3)
endif

….End
```

ForceWBuild Function

```
//This function copies the data from the outwave in the appropriate waves. Additionally the axis labels and scaling is done here.
Function ForceWBuild(pStrA, pStrR, pStrC)
String pStrA, pStrR, pStrC
SetDataFolder root:userFlags
NVAR channel0selected, channel1selected, channel2Selected, channel3Selected
SetDataFolder root:SystemParams
NVAR lastCollectedForwardSampleCount, lastCollectedRetractSampleCount
SVAR TxtForceCmt
NVAR startptV, endptV , nmOf0V, nmOf10V, lastChannelCount
SetDataFolder root:userParams
WAVE LastForceScanChannelNumber
NVAR stepsize, delayup, delaydown,stepsized,dwellTime
NewDataFolder /O/S root:forceScans
WAVE FWavein, FWaveRR, FWaveSRWaveIn
NVAR SRBitCollectingDelay, SR2, endTime, sm2Scale,startTime, sm2R, sm2RScale
Variable Period1, Period2, sDisplay, smid, sm1,sm2, lastFWaveIn
String name, NumStr, sStr, sStr1
variable i
DoWindow /K DFWave2
DoWindow /K DFWave1
DoWindow /K DFWave0
DoWindow /K DFWaveC
DoWindow /K DFApproachRetraceCombined
Killwaves /Z FWave0, FWave1, FWave2,FWave0r,FWave1r, FWave2r, FWaveC, FWaveCR, FWaveApproach, FWaveRetract,FWave0RT

….
//STRESS RELAXATION
//Check to see if need a window for stress relaxation (Force vs time)
if(dwellTime!=0)
        DoWindow/K DFWaveSRAB //adding stress relaxation window for Force
        DoWindow/K DFWaveSRAD7 //adding stress relaxation window for Displacement
        DoWindow/k DFWaveAD7Combined
        DoWindow/k DFWaveSRABCombined
        // kills any previous waves
        Killwaves /Z FWaveSRAD7, FWaveSRAB, FWave1AD7Combined, FWaveAD7Combined,
        FWaveApproachABCombined,FWaveSRABCombined,FWaveSRABCombined, FWaveRetractABCombined

        Make/O /N=(numpnts(FWaveSRWaveIn)/2) FWaveSRAB, FWaveSRAD7
        //Separating data in FWaveSRWaveIn between FWaveSRAD7 and FWaveSRAB
        //Separating FWaveSRAB and converting it to voltage
```

```
for (i=0; i<((numpnts(FWaveSRWaveIn)/2)); i+=1)
	FWaveSRAB[i]=FWaveSRWaveIn[2*i]/32767*10.24
endfor
//Setting Scale of FWaveSRAB
//THE INTERVAL OF THE TIME IS 100milliseconds since channel is retrieved every 100ms
SetScale/P x 0, 2*1.25e-06*SRBitCollectingDelay,"s", FWaveSRAB
SetScale d 0,0,"V", FWaveSRAB
note /K FWaveSRAB  //Killing any pre-existing notes of this wave
sStr="\r\nThe sampling Interval for each channel is: "+ num2str(2*1.25e-06*SRBitCollectingDelay)+" seconds" //need to add comment, maybe
Note FWaveSRAB
sStr+pStrC+"\r\n@CHANNELNAME="+chNum2name(LastForceScanChannelNumber[0]-1) //Making a new note for this wave

//Separating FWaveSRAD7 and converting it to voltage
for (i=0; i<((numpnts(FWaveSRWaveIn)/2)); i+=1)
	FWaveSRAD7[i]=FWaveSRWaveIn[2*i+1]/32767*10.24
endfor
//Setting Scale of FWaveSRAD7
SetScale/P x 0, 2*1.25e-06*SRBitCollectingDelay,"s", FWaveSRAD7 //THE INTERVAL OF THE TIME IS 50milliseconds since channel is retrieved every 50ms
SetScale d 0,0,"V", FWaveSRAD7
note /K FWaveSRAD7  //Killing any pre-existing notes of this wave
sStr="\r\nThe sampling Interval for each channel is: "+ num2str(2*1.25e-06*SRBitCollectingDelay)+" seconds"
Note FWaveSRAD7
pStrC+"\r\n@CHANNELNAME="+chNum2name(LastForceScanChannelNumber[1]-1) //Making a new note for this wave
//Copying FWave1 to FWaveAD7Combined
Duplicate/O FWave1, FWave1AD7Combined
SetScale/P x 0, 2*1.25e-06*50, "s", FWave1AD7Combined
SetScale d 0,0,"V", FWave1AD7Combined
//Copying FWaveSRAD7 to FWaveAD7Combined
Duplicate/O FWaveSRAD7, FWaveAD7Combined
SetScale/P x sm2, 2*1.25e-06*SRBitCollectingDelay, "s", FWaveAD7Combined
SetScale d 0,0,"V", FWaveAD7Combined
//Copying FWave0 to FWaveApproachABCombined
Duplicate/O FWave0, FWaveApproachABCombined
sm2=(numpnts(FWave0)-1)*1.25*delayup/1000000
sm2Scale=sm2/numpnts(FWave0)
SetScale/I x 0, sm2, "s", FWaveApproachABCombined
SetScale d 0,0,"V", FWaveApproachABCombined
//Copying FWaveSRAB to FWaveSRABCombined
Duplicate/O FWaveSRAB, FWaveSRABCombined
```

```
        SetScale/P x sm2, 2*1.25e-06*SRBitCollectingDelay,"s",
        FWaveSRABCombined
        SetScale d 0,0,"V", FWaveSRABCombined
        //Copying FWave0R to FWaveRetractABCombined
        Duplicate/O FWaveRetract, FWaveRetractABCombined
        SR2=2*1.25e-06*SRBitCollectingDelay
        startTime=sm2+(2*1.25e-
        06*SRBitCollectingDelay*numpnts(FWaveSRABCombined))
        sm2R=(numpnts(FWaveRetractABCombined)-1)*1.25*delaydown/1000000
        sm2RScale=sm2R/numpnts(FWaveRetractABCombined)
        endTIME=startTime+sm2R
        SetScale/P x sm2+(2*1.25e-
        06*SRBitCollectingDelay*numpnts(FWaveSRABCombined)),
        (numpnts(FWaveRetractABCombined)-1)*1.25*delaydown/1000000/
        numpnts(FWaveRetractABCombined),"s", FWaveRetractABCombined
        SetScale d 0,0,"V", FWaveRetractABCombined
endif //END OF STRESS RELAXATION CHECK

….End
```

ForceWSave Function

```
// this function saves all recorded waves (by callingfwSaveWave) and a general note on
the force scan
Function ForceWSave()

SetDataFolder root:userFlags
NVAR channel0selected, channel1selected, channel2Selected, channel3Selected
NVAR calibrated=root:SystemFlags:calibrated
SetDataFolder root:UserParams:
WAVE sampleScanSettings
SVAR experimentName, setName
NVAR dwellTime
SetDataFolder root:SystemParams:
NVAR nmOf0V, nmOf10V
NVAR InvOLS, SpringCst
NewDataFolder /O/S root:forceScans
WAVE FWave0, FWave1, FWave2,FWave0r,FWave1r, FWave2r, FWaveC,
FWaveCR,FWaveSRAD7, FWaveSRAB
NVAR LastForceScan=root:systemParams:LastForceScan
NVAR exportToMunichFormat=root:userFlags:exportToMunichFormat

….

//Saving Waves
sflag=fwSaveWave(FWave0, "_A")
sflag+=fwSaveWave(FWave0R,"_R")
```

```
sflag+=fwSaveWave(FWave1, "_A")
sflag+=fwSaveWave(FWave1R,"_R")
sflag+=fwSaveWave(FWave2, "_A")
sflag+=fwSaveWave(FWave2R,"_R")
if (sflag>0)
        fwSaveWave(FWaveC, "C_A")
        fwSaveWave(FWaveCR,"C_R")
else
        fwSaveWave(FWaveC, "_A")
        fwSaveWave(FWaveCR,"_R")
endif
//Saving Stress Relaxation Waves
if(dwellTime>0)
        fwSaveWave(FWaveSRAD7, "_SR")
        fwSaveWave(FWaveSRAB, "_SR")
endif

….End
```

ForceWDisplay Function

```
// This function displays the prescaled collected data on various channels
Function ForceWDisplay(pNum)
Variable pNum
NVAR lastChannelCount=root:systemParams:lastChannelCount
NVAR windowKilling=root:userParams:windowKilling
SetDataFolder root:userFlags
NVAR channel0selected, channel1Selected, channel2Selected, channel3Selected
SetDataFolder root:userParams
WAVE ForceScanChannelNumber, LastForceScanChannelNumber
NVAR dwellTime
….

//Adding Stress Relaxation Windows
if (dwellTime!=0) //Checking if stress relaxation was performed
if ((WaveExists(FWaveSRAB)==1))
        l=mh_getWinPositionCoord("l", "DFWaveSRAB")
        t=mh_getWinPositionCoord("t", "DFWaveSRAB")
        r=mh_getWinPositionCoord("r", "DFWaveSRAB")
        b=mh_getWinPositionCoord("b", "DFWaveSRAB")
if (l+t+r+b==-4)
        display /K=(windowKilling) /W=(100 ,200, 700,400) FWaveSRAB as "Stress
        Relaxation -- "+chNum2name(LastForceScanChannelNumber[0]-1)
else
        display /K=(windowKilling) /W=(l,t,r,b) FWaveSRAB as "Stress Relaxation --
        "+chNum2name(LastForceScanChannelNumber[0]-1)
endif
        DoWindow /C DFWaveSRAB
```

```
		ShowInfo
		ModifyGraph rgb(FWaveSRAB)=(0,12800,52224)
		sStr=StringFromList(0,note(FWaveSRAB),"!")
		TextBox/C/N=text0/Z=1/G=(65280,0,0)/A=LB/X=0.00/Y=-22.00 sStr
endif
if ((WaveExists(FWaveSRAD7)==1))
		l=mh_getWinPositionCoord("l", "DFWaveSRAD7")
		t=mh_getWinPositionCoord("t", "DFWaveSRAD7")
		r=mh_getWinPositionCoord("r", "DFWaveSRAD7")
		b=mh_getWinPositionCoord("b","DFWaveSRAD7")
		if (l+t+r+b==-4)
		display /K=(windowKilling) /W=(90 ,205, 580,445) FWaveSRAD7 as "Stress
		Relaxation -- "+chNum2name(LastForceScanChannelNumber[1]-1)
		else
		display /K=(windowKilling) /W=(l,t,r,b) FWaveSRAD7 as "Stress Relaxation --
		"+chNum2name(LastForceScanChannelNumber[1]-1)
		endif
		DoWindow /C DFWaveSRAD7
		ShowInfo
		ModifyGraph rgb(FWaveSRAD7)=(0,12800,52224)
		sStr=StringFromList(0,note(FWaveSRAD7),"!")
		TextBox/C/N=text0/Z=1/G=(65280,0,0)/A=LB/X=0.00/Y=-22.00 sStr
//Displaying combined AD7
		l=mh_getWinPositionCoord("l", "DFWaveAD7Combined")
		t=mh_getWinPositionCoord("t", "DFWaveAD7Combined")
		r=mh_getWinPositionCoord("r", "DFWaveAD7Combined")
		b=mh_getWinPositionCoord("b","DFWaveAD7Combined")
		if (l+t+r+b==-4)
		display /K=(windowKilling) /W=(90 ,205, 580,445) FWave1AD7Combined,
		FWaveAD7Combined as "Stress Relaxation Combined--
		"+chNum2name(LastForceScanChannelNumber[1]-1)
		else
		display /K=(windowKilling) /W=(l,t,r,b) FWave1AD7Combined,
		FWaveAD7Combined as "Stress Relaxation Combined--
		"+chNum2name(LastForceScanChannelNumber[1]-1)
		endif
		DoWindow /C DFWaveAD7Combined
		ShowInfo
		ModifyGraph rgb(FWaveAD7Combined)=(0,12800,52224)
//Displaying combined AB
		l=mh_getWinPositionCoord("l", "DFWaveSRABCombined")
		t=mh_getWinPositionCoord("t", "DFWaveSRABCombined")
		r=mh_getWinPositionCoord("r", "DFWaveSRABCombined")
		b=mh_getWinPositionCoord("b","DFWaveSRABCombined")
		if (l+t+r+b==-4)
```

```
        display /K=(windowKilling) /W=(90 ,205, 800,445)
        FWaveApproachABCombined, FWaveSRABCombined,
        FWaveRetractABCombined as Approach, Stress Relaxation, and Retrace
        Combined-- "+chNum2name(LastForceScanChannelNumber[1]-1)
        else
        display /K=(windowKilling) /W=(l,t,r,b) FWaveApproachABCombined,
        FWaveSRABCombined, FWaveRetractABCombined as "Approach, Stress
        Relaxation, and Retrace Combined--
        "+chNum2name(LastForceScanChannelNumber[1]-1)
        endif
        DoWindow /C DFWaveSRABCombined
        ShowInfo
        ModifyGraph rgb(FWaveRetractABCombined)=(0,12800,52224)
endif
endif //END OF STRESS RELAXATION SECTION

….End
```

APPENDIX 2

VISCOELASTICITY (DARLING MODEL)

```
clear
close all;

%This starts the stress relaxation analysis

%Opens dialog box to select experiment path in OBC AFM directory
directory_name=uigetdir('C:\Experiments\OBC AFM','Select the experiment directory.')

%Gets text files in the force scan directory
contentsforce = dir(fullfile(directory_name, '*A-B_os_A.txt'));
contentsforceSR = dir(fullfile(directory_name, '*A-B_os_SR.txt'));

%Gets text files in the piezo displacement directory
contentspiezo = dir(fullfile(directory_name, '*AD7_A.txt'));
contentspiezoSR= dir(fullfile(directory_name, '*AD7_SR.txt'));

%Sets output to Excel file
ind = strfind(directory_name,'\');
dir_name = directory_name(1,1:ind(4));
%dir_name = directory_name(1,1:ind(7));
a=input('Please enter the desired name of the file: ');
out_file = strcat(dir_name, a);

%Tab name
b=input('Please enter tab name: ');

vals2 = {'Name', 'Dwell Time (s)', 'Indentation (m)', 'Radius of Indenter (m)', 'Poisson
Ratio', 'A', 'B', 'C', 'R^2', 'Relaxed Modulus (Pa)', 'te(deformation)(s)','to(load)(s)',
'Apparent Viscosity (Pa s)'};
cell_name ={'A1' };
xlswrite(out_file, vals2, b, cell2mat(cell_name));

%Gets user inputted spring constant and slope
'This is for a spherical indenter'
spring_constant = input('Please enter the spring constant in N/m: ');
slope = input('Please enter the slope in m/V: ');
radius= input('Please enter radius of microbead in m: ');
pratio= input('Please enter the Poisson ratio: ');

%Data channel acq. sampling interval for SR channels (50 milliseconds)
SRsampinter=.050;
```

```
%Reads text files
 for (ll = 1:length(contentsforceSR))
%Reads the Stress Relaxation text files
   varSR = textread(fullfile(directory_name, contentsforceSR(ll).name), '%s');
   numsSR = zeros(length(varSR)-1, 1);
   calibrated_forceSR = zeros(length(varSR)-1, 1);
   for (ii = 2:length(varSR))
      numsSR(ii-1) = str2num(cell2mat(varSR(ii)));
   end
%Converts the stress relaxation raw cantilever deflection into applied force in Newtons
   for (ii = 1:length(numsSR))
      calibrated_forceSR(ii) = -(spring_constant.*slope.*numsSR(ii));
   end
%Reads the Elasticity text files
   var = textread(fullfile(directory_name, contentsforce(ll).name), '%s');
   nums = zeros(length(var)-1, 1);
   calibrated_force = zeros(length(var)-1, 1);
   for (ii = 2:length(var))
      nums(ii-1) = str2num(cell2mat(var(ii)));
   end
%Converts raw cantilever deflection into applied force in Newtons
   for (ii = 1:length(nums))
      calibrated_force(ii) = -(spring_constant.*slope.*nums(ii));
   end

%Determines true displacement scale for elasticity and viscoelasticity
%%%ELASTICITY: FOR FINDING FINAL INDENTATION VALUE
   varpiezo = textread(fullfile(directory_name, contentspiezo(ll).name),...
      '%s');
   xdispl = zeros(length(varpiezo)-1, 1);
   displacement = zeros(length(varpiezo)-1, 1);

   for (ii = 2:length(varpiezo))
      xdispl(ii-1) = str2num(cell2mat(varpiezo(ii)))+10;
      displacement(ii-1) = ((60.014E-6)/10.24).*xdispl(ii-1);
   end
%Plots raw voltage versus cantilever deflection data
   figure;
   subplot(3,1,1)
   plot(displacement, nums);
   xlabel('Displacement (m)');
   ylabel('Cantilever Deflection (V)');

%Converts x displacement into actual indentation
```

```
    scaling_factor = zeros(length(var)-1, 1);
    indentation = zeros(length(var)-1, 1);
    displacement2=displacement;
    nums2=nums;

%Calculating Scaling Factor
    for(jj=1:length(nums))
        if nums2(jj)<0
            scaling_factor(jj) = -slope.*nums2(jj);
        else
            scaling_factor(jj) = slope.*nums2(jj);
        end
        indentation(jj) = displacement2(jj)-scaling_factor(jj);
    end

%Indentation index to be used in stress relaxation curve fitting
    lengthIndent=length(indentation);

%%%VISCOELASTICITY
%Reading raw data of piezo during Stress Relaxation
    varpiezoSR = textread(fullfile(directory_name, contentspiezoSR(ll).name),...
        '%s');
    xdisplSR = zeros(length(varpiezoSR)-1, 1);
    displacementSR = zeros(length(varpiezoSR)-1, 1);
%Converting data into displacement
    for (ii = 2:length(varpiezoSR))
        xdisplSR(ii-1) = str2num(cell2mat(varpiezoSR(ii)))+10;
        displacementSR(ii-1) = ((60.014E-6)/10.24).*xdisplSR(ii-1);
    end
%Converts x displacement into actual indentation
    scaling_factor = zeros(length(varpiezoSR)-1, 1);
    indentationSR = zeros(length(varpiezoSR)-1, 1);
    displacement2SR=displacementSR;
    xdisplSR2=xdisplSR;

%Calculating Scaling Factor
    for(jj=1:length(numsSR))
        if xdisplSR2(jj)<0 %Determines whether the force is
            scaling_factor(jj) = -slope.*numsSR(jj);
        else
            scaling_factor(jj) = slope.*numsSR(jj);
        end
        indentationSR(jj) = displacement2SR(jj)-scaling_factor(jj);
    end

 %Time Interval of Elasticity portion
```

```
%1.2500e-004 sampling period for elasticity
Esampinter=50*1.25e-06*2;
Etotaltime=Esampinter*length(displacement);
ETimeArray=0:Esampinter:(Etotaltime-Esampinter);

%Time Interval of Stress Relaxation portion
 %Data channel acq. sampling interval for SR channels (1 milliseconds)
SRsampinter=.001;
SRtotaltime=0.001*length(displacementSR);
%Creates an time array from 0 sec to dwellTime in interval of 50ms
SRTimeInt=0:SRsampinter:(SRtotaltime-SRsampinter);

%MAKING DISPLACEMENT VS TIME GRAPH
PZDisplace=cat(1, displacement, displacementSR);
%Rescales PZDisplace so that the first index is 0
PZDisplace_zeroed=PZDisplace-PZDisplace(1);
CombTime=cat(2, ETimeArray, (Etotaltime+SRTimeInt));
subplot(3,1,2)
plot(CombTime, PZDisplace_zeroed)
xlabel('Time (seconds)')
ylabel('Piezo Displacement (m)')
title('Cantilever base Displacement')

%Converts x displacement into actual indentation
  scaling_factor = zeros(length(PZDisplace)-1, 1);
  indentationTOTAL = zeros(length(PZDisplace)-1, 1);
  displacement2SR=displacementSR;
  PZDisplace2=PZDisplace;
  for(jj=1:length(PZDisplace))
     if PZDisplace2(jj)<0 %Determines whether the force is
        scaling_factor(jj) = -slope.*PZDisplace2(jj);
     else
        scaling_factor(jj) = slope.*PZDisplace2(jj);
     end
     indentationTOTAL(jj) = PZDisplace2(jj)-scaling_factor(jj);
  end

  %Rescaling Indentation to start at 0
  RSindentationTOTAL=indentationTOTAL-indentationTOTAL(1);
  %Indentation Value for Stress Relaxation
  finalIndent=RSindentationTOTAL(end);
  %Calculating RiseTime
  riseTime=CombTime(find(RSindentationTOTAL==finalIndent,1));

%MAKING FORCE VS TIME GRAPH
ForceCombined=cat(1,calibrated_force, calibrated_forceSR);
```

```
smoothedForceCombined=smooth(ForceCombined, 500);
subplot(3,1,3)
plot(CombTime,smoothedForceCombined)
xlabel('Time (seconds)')
ylabel('Force (Newtons)')
title('Force measured by cantilever deflection')

%CALLING SRFIT FUNCTION TO FIT THE SR FORCE VS TIME
% FIT MODEL IS:  A*exp(-B*x)+C
% PLOTS THE SRFORCE VS TIME AS WELL AS THE FIT
% RETURNS THE COEFFICIENTS AND CONFIDENCE INTERVALS FOR THE
COEFFICIENTS

%Smoothing force
smoothedCalibratedForceSR=smooth(calibrated_forceSR,10000);

%Performing fit with Darling Model
[results_coeff, results_confid, SRff,
goodfit]=SRFIT_Darling(SRTimeInt,smoothedCalibratedForceSR);

%Result Coefficients for Darling Model
A=results_coeff(1);
B=results_coeff(2);
C=results_coeff(3);

%Confidence IntervalS
ConfidIntA=results_confid(:,1);
ConfidIntB=results_confid(:,2);
ConfidIntC=results_confid(:,3);

%Goodness of fit parameters
SSE=goodfit.sse;
RSquare=goodfit.rsquare;
DFE=goodfit.dfe;
ARSq=goodfit.adjrsquare;
RMSE=goodfit.rmse;

%Calculating parameters of stress relaxation model from Darling 2006
RelaxedE=(3*C*(1-pratio))/(4*radius^0.5*finalIndent^1.5);
time_cdef=1/B;
time_cload=time_cdef+(time_cdef*A/C);
ApparentVis=RelaxedE*(time_cload-time_cdef);

%Writes results to Excel
vals={contentsforceSR(ll).name, SRtotaltime, finalIndent, radius, pratio, A, B, C,
RSquare, RelaxedE, time_cdef, time_cload, ApparentVis};
```

```
 cell_name ={'A' num2str(ll+1)};
 xlswrite(out_file, vals, b, cell2mat(cell_name));

end %end of main for loop
```

Darling Model Fit Function

```
function [results_coeff, results_conf, cf_, gof]=
SRFIT_Darling(SRTimeInt,calibrated_forceSR)
%SRFIT    Create plot of datasets and fits

figure;
legh_ = []; legt_ = {};   % handles and text for legend
xlim_ = [Inf -Inf];       % limits of x axis
ax_ = axes;
set(ax_,'Units','normalized','OuterPosition',[0 0 1 1]);
set(ax_,'Box','on');
axes(ax_); hold on;


% --- Plot data originally in dataset "calibrated_forceSR vs. SRTimeInt"
SRTimeInt = SRTimeInt(:);
calibrated_forceSR = calibrated_forceSR(:);
h_ = line(SRTimeInt,calibrated_forceSR,'Parent',ax_,'Color',[0.333333 0 0.666667],...
    'LineStyle','none', 'LineWidth',1,...
    'Marker','.', 'MarkerSize',12);
xlim_(1) = min(xlim_(1),min(SRTimeInt));
xlim_(2) = max(xlim_(2),max(SRTimeInt));
legh_(end+1) = h_;
legt_{end+1} = 'calibrated_forceSR vs. SRTimeInt';

% Nudge axis limits beyond data limits
if all(isfinite(xlim_))
  xlim_ = xlim_ + [-1 1] * 0.01 * diff(xlim_);
  set(ax_,'XLim',xlim_)
end

%Calculating starting points for fit
startA=calibrated_forceSR(1);
startC=calibrated_forceSR(length(calibrated_forceSR));
%Create fit
fo_ = fitoptions('method','NonlinearLeastSquares','Robust','On','Algorithm','Levenberg-
Marquardt','MaxFunEvals',10000,'MaxIter',10000);
ok_ = ~(isnan(SRTimeInt) | isnan(calibrated_forceSR));
st_ = [startA 0.8 startC ];
set(fo_,'Startpoint',st_);
```

```
ft_ = fittype('a*exp(-b*x)+c',...
    'dependent',{'y'},'independent',{'x'},...
    'coefficients',{'a', 'b', 'c'});

% Fit this model using new data
[cf_ gof] = fit(SRTimeInt(ok_),calibrated_forceSR(ok_),ft_,fo_);

% Or use coefficients from the original fit:
if 0
  cv_ = {1.965254389031e-007, 0.2468091779351, 4.391328108047e-007};
  cf_ = cfit(ft_,cv_{:});
end

% Retrieving coefficient values and their confidence intervals
results_coeff=coeffvalues(cf_);
results_conf=confint(cf_);

% Plot this fit
h_ = plot(cf_,'fit',0.95);
legend off;  % turn off legend from plot method call
set(h_(1),'Color',[1 0 0],...
    'LineStyle','-', 'LineWidth',2,...
    'Marker','none', 'MarkerSize',6);
legh_(end+1) = h_(1);
legt_{end+1} = 'fit 2';

% Done plotting data and fits.  Now finish up loose ends.
hold off;
h_ = legend(ax_,legh_,legt_,'Location','NorthEast');
set(h_,'Interpreter','none');
xlabel('Time (Seconds)');               % x label
ylabel('Calibrated SR Force (Newtons)'); % y label
```

APPENDIX 3

POROELASTICITY (KALCIOGLU-HU MODEL)

```
clear all; clear global; clc;
close all;

%This starts the stress relaxation analysis
%Opens dialog box to select experiment path in OBC AFM directory
 directory_name=uigetdir('C:\Experiments\OBC AFM','Select the experiment directory.')

%Gets text files in the force scan directory
contentsforce = dir(fullfile(directory_name, '*A-B_os_A.txt'));
contentsforceSR = dir(fullfile(directory_name, '*A-B_os_SR.txt'));

%Gets text files in the piezo displacement directory
contentspiezo = dir(fullfile(directory_name, '*AD7_A.txt'));
contentspiezoSR= dir(fullfile(directory_name, '*AD7_SR.txt'));

%Sets output to Excel file
 ind = strfind(directory_name,'\');
 dir_name = directory_name(1,1:ind(4));
 a=input('Please enter the desired name of the file: ');
 out_file = strcat(dir_name, a);

%Tab name
b=input('Please enter tab name: ');
vals2 = {'Name', 'Dwell Time (s)', 'SR Indentation (m)', 'Radius of Indenter (m)', 'Poisson
Ratio','R^2', 'Rise Time(s)','Ramp slope (m/s)', 'Initial Force (N)','Force at Infinity
(N)','Contact radius (m)','Shear modulus(Pa)', 'Poisson ratio of solid matrix',
'Diffusivity(m^2/s)', 'Intrinsic Permeability(m^2)'};
cell_name ={'A1' };
xlswrite(out_file, vals2, b, cell2mat(cell_name));

%Gets user inputted spring constant and slope
% 'This is for a spherical indenter'
 spring_constant = input('Please enter the spring constant in N/m: ');
 slope = input('Please enter the slope in m/V: ');
 radius= input('Please enter radius of microbead in m: ');
 pratio= input('Please enter the Poisson ratio: ');

 %Data channel acq. sampling interval for SR channels (50 milliseconds)
SRsampinter=.050;

%Reads text files
 for (ll = 1:length(contentsforceSR))
```

```
%Reads the Stress Relaxation text files
   varSR = textread(fullfile(directory_name, contentsforceSR(ll).name), '%s');
   numsSR = zeros(length(varSR)-1, 1);
   calibrated_forceSR = zeros(length(varSR)-1, 1);
   for (ii = 2:length(varSR))
      numsSR(ii-1) = str2num(cell2mat(varSR(ii)));
   end
%Converts the stress relaxation raw cantilever deflection into applied force in Newtons
   for (ii = 1:length(numsSR))
      calibrated_forceSR(ii) = -(spring_constant.*slope.*numsSR(ii));
   end
%Reads the Elasticity text files
   var = textread(fullfile(directory_name, contentsforce(ll).name), '%s');
   nums = zeros(length(var)-1, 1);
   calibrated_force = zeros(length(var)-1, 1);
   for (ii = 2:length(var))
      nums(ii-1) = str2num(cell2mat(var(ii)));
   end
%Converts raw cantilever deflection into applied force in Newtons
   for (ii = 1:length(nums))
      calibrated_force(ii) = -(spring_constant.*slope.*nums(ii));
   end

%Determines true displacement scale for elasticity and viscoelasticity
%%%ELASTICITY: FOR FINDING FINAL INDENTAION VALUE
   varpiezo = textread(fullfile(directory_name, contentspiezo(ll).name), '%s');
   xdispl = zeros(length(varpiezo)-1, 1);
   displacement = zeros(length(varpiezo)-1, 1);

   for (ii = 2:length(varpiezo))
      xdispl(ii-1) = str2num(cell2mat(varpiezo(ii)))+10;
      displacement(ii-1) = ((60.014E-6)/10.24).*xdispl(ii-1);
   end
%Plots raw voltage versus cantilever deflection data
   figure;
   subplot(3,1,1)
   plot(displacement, nums);
   xlabel('Displacement (m)');
   ylabel('Cantilever Deflection (V)');

%Converts x displacement into actual indentation
   scaling_factor = zeros(length(var)-1, 1);
   indentation = zeros(length(var)-1, 1);
   displacement2=displacement;
   nums2=nums;
```

```
    for(jj=1:length(nums))
        if nums2(jj)<0 %Determines whether the force is
            scaling_factor(jj) = -slope.*nums2(jj);
        else
            scaling_factor(jj) = slope.*nums2(jj);
        end
        indentation(jj) = displacement2(jj)-scaling_factor(jj);
    end

%Indentation index to be used in stress relaxation curve fitting
    lengthIndent=length(indentation);

    %%%VISCOELASTICITY
    varpiezoSR = textread(fullfile(directory_name, contentspiezoSR(ll).name), '%s');
    xdisplSR = zeros(length(varpiezoSR)-1, 1);
    displacementSR = zeros(length(varpiezoSR)-1, 1);

    for (ii = 2:length(varpiezoSR))
        xdisplSR(ii-1) = str2num(cell2mat(varpiezoSR(ii)))+10;
        displacementSR(ii-1) = ((60.014E-6)/10.24).*xdisplSR(ii-1);
    end
%Converts x displacement into actual indentation
    scaling_factor = zeros(length(varpiezoSR)-1, 1);
    indentationSR = zeros(length(varpiezoSR)-1, 1);
    displacement2SR=displacementSR;
    xdisplSR2=xdisplSR;
%Calculating Scaling Factor
    for(jj=1:length(numsSR))
        if xdisplSR2(jj)<0
            scaling_factor(jj) = -slope.*numsSR(jj);
        else
            scaling_factor(jj) = slope.*numsSR(jj);
        end
        indentationSR(jj) = displacement2SR(jj)-scaling_factor(jj);
    end

 %Time Interval of Elasticity portion
 %1.2500e-004 sampling period for elasticity
Esampinter=50*1.25e-06*2;
Etotaltime=Esampinter*length(displacement);
ETimeArray=0:Esampinter:(Etotaltime-Esampinter);

 %Time Interval of Stress Relaxation portion
 %Data channel acq. sampling interval for SR channels (1 milliseconds)
SRsampinter=.001;
SRtotaltime=0.001*length(displacementSR);
```

```
%Creates an time array from 0 sec to dwellTime in interval of 50ms
SRTimeInt=0:SRsampinter:(SRtotaltime-SRsampinter);

%MAKING DISPLACEMENT VS TIME GRAPH
PZDisplace=cat(1, displacement, displacementSR);
%Rescales PZDisplace so that the first index is 0
PZDisplace_zeroed=PZDisplace-PZDisplace(1);
CombTime=cat(2, ETimeArray, (Etotaltime+SRTimeInt));
subplot(3,1,2)
plot(CombTime, PZDisplace_zeroed)
xlabel('Time (seconds)')
ylabel('Piezo Displacement (m)')
title('Cantilever base Displacement')

%Converts x displacement into actual indentation
  scaling_factor = zeros(length(PZDisplace)-1, 1);
  indentationTOTAL = zeros(length(PZDisplace)-1, 1);
  displacement2SR=displacementSR;
  PZDisplace2=PZDisplace;
%Calculating Scaling Factor
  for(jj=1:length(PZDisplace))
     if PZDisplace2(jj)<0
        scaling_factor(jj) = -slope.*PZDisplace2(jj);
     else
        scaling_factor(jj) = slope.*PZDisplace2(jj);
     end
     indentationTOTAL(jj) = PZDisplace2(jj)-scaling_factor(jj);
  end

%Rescale
  RSindentationTOTAL=indentationTOTAL-indentationTOTAL(1);

%MAKING FORCE VS TIME GRAPH
ForceCombined=cat(1,calibrated_force, calibrated_forceSR);
smoothedForceCombined=smooth(ForceCombined, 500);
subplot(3,1,3)
plot(CombTime,smoothedForceCombined)
xlabel('Time (seconds)')
ylabel('Force (Newtons)')
title('Force measured by cantilever deflection')

%CALLING SRFIT FUNCTION TO FIT THE SR FORCE VS TIME
% FIT MODEL IS:  KALCIOGLU
% PLOTS THE SRFORCE VS TIME AS WELL AS THE FIT
% RETURNS THE COEFFICIENTS AND CONFIDENCE INTERVALS FOR THE
COEFFICIENTS
```

```
 %smoothing force
 smoothedCalibratedForceSR=smooth(calibrated_forceSR,10000);

%**********Stress Relaxation Experimental Parameters**********
%Indentation depth Value during Stress Relaxation
   finalIndent=RSindentationTOTAL(end);
 %Calculating RiseTime
   riseTime=CombTime(find(RSindentationTOTAL==finalIndent,1));
 %Calculating ramp slope
   k=finalIndent/riseTime;
 %************************************************************

%Establishing x and y data points before performing Fit
xdataIn=SRTimeInt; %X DATA
ydataIn=smoothedCalibratedForceSR; %YDATA

%Making sure dimensions are the same
if size(xdataIn)== size(ydataIn)
   ydataIn=ydataIn; %KEEP YDATA AS IN
else
   ydataIn=ydataIn'; %RESTRUCTURING Y DATA TO MATCH DIMESIONS OF
XDATA
end

%For Kalcioglu model fit
%Initial force at time 0 of stress relaxation
F0=ydataIn(1);
%Force at infinity-Last Force Value of Stress Relaxation
F_inf=ydataIn(end);
%Calculating a^2:the square of the contact radius
a2=radius*finalIndent;

%Calculating Poroelastic Parameters of Shear Modulus and Poisson's ratio
%of solid matrix

%Calculating Shear Modulus
G=(3/16)*(F0/(finalIndent*a2^0.5));
%Calculating Poisson's ratio of solid matrix
v_s=1-(0.5*(F0/F_inf));

%Setting up model to derive diffusivity, D
%Boundaries for Fit
lowerBound = [-Inf,   -Inf,  -Inf]; %lower bound for unknowns
upperBound = [Inf,  Inf,  Inf]; %upper bound for unknowns
%Initializing number of model fit iterations to perform
```

```
NITER = 1e3; NFUN = 1e6;
opts = optimoptions('lsqcurvefit','Algorithm', 'levenberg-marquardt',...
    'TolFun',1e-24,'TolX',1e-23,'MaxIter',NITER,'MaxFunEvals',NFUN,...
    'Display','iter-detailed','ScaleProblem','Jacobian');

%Initializing diffusivity parameter D
paramIn = 1e-10;
%Creating function of Kalcioglu model fit
myfun = @(param_,xdata_) Kalcioglu_fit(param_, xdata_, a2, F0,F_inf);

%Fit the data model using parameters
[paramOut,resnorm,residual,exitflag,output,lambda,jacobian]=...
    lsqcurvefit(myfun, paramIn, xdataIn, ydataIn, lowerBound, upperBound, opts);

%Derived diffusivity parameter
D=paramOut;

%Solvent viscosity, which is that of PBS since, PBS is the solvent of the
%15% Dextran solution
n=0.90e-03;

%Calculating intrinsic permeability k
kPerm=(D*(1-(2*v_s))*n)/(2*(1-v_s)*G);

% A PLOT OF ORIGINAL DATA WITH MODEL FIT
%Evaluate new range of data based on fit
xFit  = min(xdataIn):mean(diff(xdataIn)):max(xdataIn);
yFit = feval(myfun, paramOut, xFit);
%try matlabpool close; end;

%Determining RSquare
SStot = sum((ydataIn-mean(ydataIn)).^2) ;
SSerr = sum((ydataIn-yFit).^2) ;
RSquare = 1 - SSerr/SStot;

%Plotting fit and data
figure; plot(xdataIn, ydataIn,'rx'); hold on;
plot(xFit, yFit,'x'); hold off;
legend('data','fitted');
title('Kalcioglu model');
xlabel('Time (seconds)');
axis square;

%RESULTS TO BE WRITTEN IN THE EXCEL FILE.
%  %Writes results to Excel
```

```
  vals={contentsforceSR(ll).name, SRtotaltime, finalIndent, radius, pratio, RSquare,
riseTime,k,F0,F_inf,(a2^0.5),G,v_s,D,kPerm};
  cell_name ={'A' num2str(ll+1)};
  xlswrite(out_file, vals, b, cell2mat(cell_name));

end %end of main for loop
```

Kalcioglu-Hu Model Fit Function

```
function F = Kalcioglu_fit(param, xdata, a2, F0,F_inf)

% Retrieve the parameters values to check convergence
fprintf('- D=%0.6g\n',param(1))

%This function has two inputs:
%param: the  unknown that needs to be calculated, D
%xdata: data points that need to be fitted --> t

% [Kalcioglu] Eq. 3
F =  ((0.491*exp(-0.908*sqrt(param/a2.*xdata))+ 0.509*...
    exp(-1.679*param/a2.*xdata))*(F0-F_inf))+ F_inf;

end
```